

University of Mississippi

eGrove

Electronic Theses and Dissertations

Graduate School

1-1-2019

Investigation of narrow bipolar events in Mississippi thunderstorms

Sampath Asiri Bandara

Follow this and additional works at: <https://egrove.olemiss.edu/etd>



Part of the [Physics Commons](#)

Recommended Citation

Bandara, Sampath Asiri, "Investigation of narrow bipolar events in Mississippi thunderstorms" (2019).
Electronic Theses and Dissertations. 1955.
<https://egrove.olemiss.edu/etd/1955>

This Dissertation is brought to you for free and open access by the Graduate School at eGrove. It has been accepted for inclusion in Electronic Theses and Dissertations by an authorized administrator of eGrove. For more information, please contact egrove@olemiss.edu.

INVESTIGATION OF NARROW BIPOLAR EVENTS IN MISSISSIPPI
THUNDERSTORMS

A Dissertation
presented in partial fulfillment of requirements
for the degree of Doctor of Philosophy
in the Department of Physics and Astronomy
University of Mississippi

by

SAMPATH BANDARA

August 2019

ABSTRACT

This dissertation investigates Narrow Bipolar Events (NBEs), which are a type of short-duration (10- 30 μ s) lightning discharge. The study primarily used data from NBEs collected in 2016 at seven sensor sites within 50 km of Oxford, Mississippi, USA. Each sensor site had three electromagnetic antennas called Fast Antenna (FA), dE/dt, and Log-RF with bandwidths of 0-2.5 MHz, 0-1.0 MHz, and 186-192 MHz, respectively. NBEs are often isolated from other lightning events in thunderclouds, but they sometimes initiate negative cloud-to-ground (-CG) and intracloud (IC) lightning flashes, or they can occur during these flashes.

In the first part of the study, FA and Log-RF data were used to examine low-altitude (<8.0 km) negative NBEs (NNBEs) to see how many -CG flashes were initiated by NNBEs. Out of 686 -CG flashes, only 33 (5%) flashes were initiated by an NNBE. These NNBEs occurred at an average altitude of 6.2 km, had average amplitude (range-normalized amplitude to 100 km) of 0.4 V/m, and had average VHF (Log-RF) power of 130 W. Since the low-altitude NNBEs were substantially weaker than positive NBEs that initiate intracloud (IC) flashes, it is hypothesized that -CG flashes are easier to initiate than IC flashes.

The second part of the study investigated the properties of 201 positive NBEs (+NBEs). The +NBEs were classified in two ways: into Types A-D [Karunarathne et al., 2015] and into three different groups: Isolated, Not-isolated, and IC flash-initiator or INBE [Wu et al., 2014]. The average VHF (Log-RF) power of NBEs within the A-D categories were 1.9, 4.0, 9.8, and 13.2 kW, respectively, while the powers for the Isolated, Not-isolated, and INBE categories were 10.1, 4.0, and 10.1 kW, respectively.

The third study considered 34 NBEs that occurred close in space and time to each other: 13 pairs of NBEs, one group of three +NBEs, and one group of five +NBEs. The NBEs were overlaid on radar data of the parent thunderstorms. The data indicate that the individual NBEs in each group initiated in separate intense electric field regions of small extent rather than in a single large-scale electric field region.

ACKNOWLEDGMENTS

I am profoundly thankful to my adviser Dr. Thomas Marshall for introducing me to the field of lightning Physics. He has given me the freedom to pursue different problems in lightning Physics while providing me with every bit of guidance, assistance, and expertise that I needed during this time. Without his enormous guidance and persistent help, the work presented in this dissertation could not have been accomplished. I am also deeply grateful to Dr. Maribeth Stolzenburg for her advice and comments during this work, and her ideas and encouragement always carried forward my research work.

I also want to thank my Ph.D. committee members, Dr. Likun Zhang and Dr. Richard K. Gordon for their assistance and valuable comments during my dissertation work. I am always grateful for the guidance and support received from Dr. Sumedha Karunaratne. His excellent advice has always benefited by both my research as well as a career in every possible way during this time. My thanks also go out to the support I received from the University of Mississippi to obtain my Ph.D.

My deep appreciation goes out to the Dr. Buddhika Dassanayake. Without his dedication, support, and advice, this Ph.D. journey would never have been started in the first place. My sincere thanks should go to my parents for their love and encouragement during this journey. I extend my thanks to colleagues from Atmospheric Physics group at Ole Miss for their assistance and friendship.

TABLE OF CONTENTS

ABSTRACT.....	ii
ACKNOWLEDGMENTS	iv
LIST OF TABLES	ix
LIST OF FIGURES	x
CHAPTER 1 INTRODUCTION	1
CHAPTER 2 INSTRUMENTATION	6
2.1 Electric field change meter	6
2.2 dE/dt antenna	7
2.3 Log-RF antenna	10
2.4 Log-RF antenna group delay estimation.....	12
2.5 Array configuration and operation.....	14
CHAPTER 3 DETERMINING THE LOCATION OF LIGHTNING EVENTS	17
3.1 Summary and Conclusions	22
CHAPTER 4 CHARACTERIZING THREE TYPES OF NEGATIVE NARROW BIPOLAR EVENTS IN THUNDERSTORMS	24
4.1 Introduction.....	24
4.2 Data and analysis methods.....	27
4.2.1 Determining NNBE Locations.....	27

4.2.2 Calculating NNBE range-normalized amplitudes and NNBE VHF source powers	27
4.2.3 Identification of typical NNBEs	29
4.2.4 Identification of NNBEs preceding -CG flashes	31
4.3 Statistical results	42
4.3.1 Low percentage of -CG flashes preceded by an NNBE	42
4.3.2 Altitudes of NNBEs	43
4.3.3 Durations of NNBEs	45
4.3.4 Range-normalized amplitudes of NNBEs	47
4.3.5 VHF power of NNBEs	49
4.3.6 Distance and time separations between NNBEs and the first classic IB pulse	51
4.3.7 Successive time separations between FA pulses	53
4.3.8 Altitude separations between NNBE-IBP	54
4.4 Discussion	57
4.5 Summary and Conclusions	58
 CHAPTER 5 CHARACTERISTIC OF VHF PEAK POWER ASSOCIATED WITH POSITIVE NARROW BIPOLAR LIGHTNING PULSES	 62
5.1 Introduction	62
5.2 Identification of NBEs	65
5.3 Categorization of NBEs into Types A, B, C, and D.	67

5.4 Categorization of NBE according to their spatiotemporal relationship with other lightning activities.....	69
5.5 Statistical investigations.....	74
5.5.1 FA waveforms of NBEs.....	74
5.5.2 Log-RF waveforms of NBEs	75
5.5.3 VHF source Power of NBEs in Method 1.	78
5.5.4 VHF source Power of NBEs in Method 2.	79
5.5.5 Characteristic of Rise time of Log-RF waveform.....	80
5.6 Summary and Conclusions.	84
CHAPTER 6 THE OCCURRENCE OF MULTIPLE NBES WITHIN THUNDERSTORMS	86
6.1 Introduction.....	86
6.2 Data and Methodology.....	88
6.3 Space and Time development of NBE Groups.....	89
6.3.1 Altitudes, range-normalized amplitudes, and VHF powers of NBEs in groups.	89
6.3.2 Time and Horizontal separation of NBEs in groups.	92
6.3.3 Spatiotemporal relation with other lightning activities.....	92
6.4 Summary and Conclusions.	100
CHAPTER 7 SUMMARY.....	102
BIBLIOGRAPHY	107

APPENDIX A CIRCUIT DIAGRAM OF ELECTRIC FIELD DERIVATIVE AND LOG-RF SENSOR.	113
APPENDIX B NNBES THAT INITIATE -CG FLASHES: ADDITIONAL EXAMPLES....	115
VITA.....	142

LIST OF TABLES

Table 5.1. Number of types A–D NBEs.	69
Table 5.2. Number of INBEs, isolated, and Not-isolated NBEs.....	73
Table 5.3. Number of NBE found in method 1 classification within method 2.	73
Table 5.4. Comparison of FA waveform properties of NBEs.	75
Table 6.1. Number of NBEs groups.....	88

LIST OF FIGURES

Figure 2.1. Band widths of dE/dt antenna	9
Figure 2.2. Electronic component design of the Log-RF antenna system	10
Figure 2.3. Phase response of 4 different bandpass filter	13
Figure 2.4. Sensor arrangement of EE and SS sites.	15
Figure 3.1. Comparison of PBFA and $\int dE/dt$ methods for pulse altitudes (z) in CG flash. 19	
Figure 3.2. Comparison of PBFA and $\int dE/dt$ methods for Horizontal pulse positions (X-Y) in CG flash.	20
Figure 3.3. Similar to Figure 3.1, which shows another comparison example of the PBFA and $\int dE/dt$ methods for pulse altitudes in IC flash.	21
Figure 3.4. Similar to Figure 3.2, shows an example of X-Y location comparison in 2 methods for IB pulses during the first 1ms of the IC flash.....	22
Figure 4.1. Plan view of seven sensor sites along with locations of NNBEs.	29
Figure 4.2. E-change (FA) and Log-RF waveforms of a typical negative narrow bipolar pulse.	31
Figure 4.3. Example of an NNBE(L) that apparently initiated a -CG flash.	35
Figure 4.4. Similar to Figure 4.3, showing another example of an NNBE(L) that apparently initiated a -CG flash.....	38
Figure 4.5. Similar to Figure 4.3, showing an example of an NNBE(H) that apparently initiated a -CG flash.....	39
Figure 4.6. Similar to Figure 4.5, showing another example of an NNBE(H) that apparently initiated a -CG flash.....	41

Figure 4.7. (a) Altitude histogram of the three types of NNBEs. (b) Horizontal distance error and altitude error for NNBE(L)s and NNBE(H)s. (c) Similar to (b), but for NNBE(T).	44
Figure 4.8. Durations for the three NNBE types.	46
Figure 4.9. Histogram of NNBE zero-to-peak FA magnitudes range-normalized to 100 km (E_{100km}) for the three NNBE groups.	48
Figure 4.10. Histograms of VHF powers of the three NNBE types.	50
Figure 4.11. Distance and time separations between NNBEs and the first classic IB pulse ..	51
Figure 4.12. Histogram of time separations between successive pulses.	53
Figure 4.13. Altitude difference (z_1-z_2) between the initiating NNBE and the first IB pulse in the flash.	55
Figure 5.1. Plan view of seven sensor sites (marked with stars) along with locations of 201 NBEs.	66
Figure 5.2. Examples of Types A–D NBEs.	68
Figure 5.3. Example of an NBE that occurred as a Not-isolated event in a lightning flash. . .	70
Figure 5.4. Example of positive NBE that occurred as the initial event of an IC flash.	72
Figure 5.5. Shows the definition of the rise time and zero crossing time parameters of the type A-D waveform that were recorded by FA and the Log-RF antenna.	76
Figure 5.6. Comparison of zero cross and rise time of Type A-D waveforms using Log-RF and FA data.	77
Figure 5.7. Distribution of peak radiated power for the Types A-D of NBEs.	78
Figure 5.8. Histograms of VHF powers of the three NBEs groups; INBE, Isolated, and Not-isolated.	79

Figure 5.9. Scatter plots of the peak radiated power versus the rise time of the Log-RF waveform for: (a) – (c) Type B-D of NBEs. (d)-(f) all NBEs found in INBE, not-isolated, and isolated and groups.	81
Figure 5.10. In the same format as Figure 5.9, (a) – (c) Type B-D of NBEs found in INBE group. (d)-(f) Type B-D of NBEs found in Not-isolated group. (g)-(i) Type B-D of NBEs found in Isolated group.	82
Figure 5.11. Examples of Type C NBE waveform found in INBE group.	83
Figure 6.1. Bar chart of: (a) altitude, (b) range-normalized (100 km) FA amplitude, (c) VHF powers for NBEs in groups.	90
Figure 6.2. Example of a multiple positive NBE discharge event (Group 12).	94
Figure 6.3. Radar reflectivity along with the five positive NBEs of Group 12.	95
Figure 6.4. Figure format similar to that of Figure 6.2, shows an additional example of multiple positive NBEs discharge events.	96
Figure 6.5. Radar reflectivity scan and the vertical cross sections of the volumetric radar data for three sequences of NBE discharge events in Figure 6.4.	97
Figure 6.6. Examples of mixed polarity pairs of NBEs.	98
Figure 6.7. Similar to Figure 6.3, showing radar reflectivity data for two pairs of NBE discharge events with opposite polarity within the pair, as shown in Figure 6.6.	99
Figure A.1. The circuit diagram of amplifier used in the dE/dt	113
Figure A.2. The schematic of Non-inverter level change circuit.	114
Figure B.3. Example of NNBE(L) occurred as the initial event of a negative CG flash.	117
Figure B.4. Example of NNBE(L) occurred as the initial event of a negative CG flash.	118
Figure B.5. Example of NNBE(L) occurred as the initial event of a negative CG flash.	119

Figure B.6. Example of NNBE(L) occurred as the initial event of a negative CG flash.....	120
Figure B.7. Example of NNBE(L) occurred as the initial event of a negative CG flash.....	121
Figure B.8. Example of NNBE(L) occurred as the initial event of a negative CG flash.....	122
Figure B.9. Example of NNBE(L) occurred as the initial event of a negative CG flash.....	123
Figure B.10. Example of NNBE(L) occurred as the initial event of a negative CG flash.....	123
Figure B.11. Example of NNBE(L) occurred as the initial event of a negative CG flash.....	124
Figure B.12. Example of NNBE(L) occurred as the initial event of a negative CG flash.....	125
Figure B.13. Example of NNBE(L) occurred as the initial event of a negative CG flash.....	126
Figure B.14. Example of NNBE(L) occurred as the initial event of a negative CG flash.....	127
Figure B.15. Example of NNBE(L) occurred as the initial event of a negative CG flash.....	128
Figure B.16. Example of NNBE(L) occurred as the initial event of a negative CG flash.....	129
Figure B.17. Example of NNBE(H) occurred as the very first event of a negative CG flash.	130
Figure B.18. Example of NNBE(H) occurred as the very first event of a negative CG flash.	131
Figure B.19. Example of NNBE(H) occurred as the very first event of a negative CG flash.	132
Figure B.20. Example of NNBE(H) occurred as the very first event of a negative CG flash.	133
Figure B.21. Example of NNBE(H) occurred as the very first event of a negative CG flash.	134
Figure B.22. Example of NNBE(H) occurred as the very first event of a negative CG flash.	135

Figure B.23. Example of NNBE(H) occurred as the very first event of a negative CG flash.	
.....	136
Figure B.24. Example of NNBE(H) occurred as the very first event of a negative CG flash.	
.....	137
Figure B.25. Example of NNBE(H) occurred as the very first event of a negative CG flash.	
.....	138
Figure B.26. Example of NNBE(H) occurred as the very first event of a negative CG flash.	
.....	139
Figure B.27. Example of NNBE(H) occurred as the very first event of a negative CG flash.	
.....	140
Figure B.28. Example of NNBE(H) occurred as the very first event of a negative CG flash.	
.....	141
Figure B.29. Example of NNBE(H) occurred as the very first event of a negative CG flash.	
.....	141

CHAPTER 1

INTRODUCTION

One of the most unresolved questions concerning the physics of lightning is how lightning initiates. Particularly, the electric field necessary for conventional breakdown within thunderclouds is primarily not reached. In the air, at atmospheric pressure, the electric field required for conventional breakdown is approximately 2000 kVm^{-1} . However, the maximum electric field measurements found within a thundercloud are substantially smaller than the conventional breakdown electric field. For example, Stolzenburg et al. [2007] studied and analyzed the electric field within storm clouds covering a variety of thunderstorms using approximately 250 series of balloon sounding data, and the largest observed electric field was 626 kVm^{-1} . The initiation of lightning can be loosely described as the formation and propagation of a leader channel within the thunder cloud. The leader formation process is sometimes called an initial breakdown (IB) stage of the lightning flash. This process typically happens during 2-10 ms of cloud-to-ground (CG) flashes and 5-20 ms of intracloud (IC) flashes (Marshall et al. 2014). Among the various hypothesis, **Hydrometeor theory of lightning initiation** and **Runaway breakdown and extensive atmospheric shower combine process of lightning initiation (RB-EAS)** are the two hypotheses that are most possibly responsible for the lightning initiation process.

The Relativistic runaway electron avalanche and its relation to the initiation of lightning were introduced in Gurevich et al. (1992). Gurevich et al. (1999, 2004) hypothesized that highly energetic electrons resulting from cosmic-ray air showers or extensive atmospheric showers (EAS) in the atmosphere that pass through an area of high electric field within the storm cloud extract the energy from the electric field and run away (accelerated by electric field). Additionally, these runaway electrons experience electron-electron scattering with air molecules and produce new fast electrons that eventually lead to an electron avalanche process. Thereby, this process is theorized to produce enough ionization to initiate lightning.

According to the RB-EAS theory, Gurevich et al. (2004) and Gurevich and Zybin (2005) suggest a possible mechanism for producing Narrow bipolar events, that was first reported by Le Vine 1980. Gurevich et al. (2004) suggest that RB-EAS was very-short time single pulse discharge and produce a large number of thermal electrons (low energy electron). In RB-EAS discharge, current is determined by the motion of the thermal electrons and produces a unipolar current pulse with a duration and intensity exponentially increasing according to the discharge height. Therefore, RB-EAS produce a megahertz range ($\sim 0.2\text{--}0.5$ MHz) bipolar radio pulse with an underlying current pulse that lasts approximately $0.5\text{--}8\text{ }\mu\text{s}$ depending on the discharge height. Furthermore, its emission power depends on square of the maximum value of the current pulse and could produce very high-power radio pulse. These descriptions adequately fit with the characteristic of a Narrow bipolar event.

Hydrometeor theory has long been serving as the main hypothesis for the electrification of a thundercloud. Under this mechanism, electrical charges are produced by the interaction between the graupel or hydrometeor and the cloud particle with essential presence of water droplet. With the help of the cloud updraft and gravity, they separated to significantly distant parts of cloud region. This produce the necessary ambient electric field for the lightning breakdown.

However, Hydrometeor theory of lightning initiation by means that initiation of lightning from hydrometeor with the presence of the ambient electric field. Most of the early work on the hydrometeor theory of lightning initiation was based on theoretical work or the high-voltage laboratory experiments.

Phelps et al. [1971] studied positive streamers generated by a pulsed point electrode in a uniform-field gap and found that the propagation distance of the positive streamers increases monotonically with the intensity of the external (ambient) electric field. Also, Phelps et al. (1971) discovered that at a specific value of the Electric field, streamer systems tend to grow more dramatically. In addition, more accurately replicate the thunder cloud environment, they used water droplets that fell freely in the opposite direction of the electric field to produce positive streamers caused by hydrodynamic instability. Phelps et al. [1971] observed similar behavior of the positive streamers generated by the water droplets as described above. Phelps et al. [1974] found that the intensification of the streamer system in a strong electric field causes the accumulation of negative charge towards the origin of the streamer system while increasing the net positive-charge carried by streamer tips. The more rapid the intensification, the more excess charge will be deposited.

Phelps et al. [1974] proposed that a series of such systems passing through the same volume could lead to a significant accumulation of negative charge, thus creating a strong local intensification of the electric field and thereby the initiation of lightning.

The confirmation of the initiation of a lightning process that arises from a hydrometeor has been obtained quite recently by Rison et al. 2016. Rison et al. 2016 analyzed the initiation of Narrow bipolar events that were the initial event of the intracloud lightning flash (e.g., Rison et al. 1999; Wu et al. 2014; Rison et al. 2016;).

Using the three- dimensional Lightning Mapping Array (LMA) and a high-speed broadband VHF interferometer (INTF), Rison et al. 2016 show that NBE discharge is caused by the newly identified breakdown process of "fast positive break down." In the computer simulation of NBE waveforms carried out by Rison et al. [2016] it is found that the NBE discharge is characterized by an extraordinarily large peak current with relatively small charge transfer and an unusual propagating speed ($\sim 10^7 \text{ ms}^{-1}$). Based on those information and observation of NBE discharge gain from LMA and INTF, Rison et al. [2016] concludes that NBE discharge was composed by a lateral distribution of positive streamer with unusual propagation velocity. The large current associated with the NBE discharge is caused by positive streamers which spread their current over a relatively large cross-sectional area. Initiation of streamers under the less-strong electric field has been shown by Phelps et al. [1974] and Griffiths and Phelps (1976).

However, Rison et al. [2016] also concluded that "all in-cloud and cloud to ground lightning discharges are initiated by NBE-type fast positive breakdown." However, relatively few examples exist of NBEs initiating lightning flashes. The primary goals of this dissertation are to provide more examples of NBEs or NBE-type events initiating lightning flashes and to use these data to learn more about the mechanism(s) of lightning initiation. Narrow bipolar events can be uniquely identified among other lightning activities by their strong RF emission. NBEs are also characterized by a large-amplitude and short-duration bipolar electric field change of either polarity [Willett et al., 1989]. This dissertation will investigate NBEs by studying their electromagnetic radiation emission using data collected by the author in 2016 using three different electromagnetic antennae (called E-change, dE/dt , and Log-RF). The dissertation will carry out three separate investigations.

The first part of this dissertation is motivated by the assertion of Rison et al. 2016 that negative NBEs initiate all negative cloud-to-ground lightning flashes. However, to date there is very little data to support this assertion. Previous studies [e.g., Smith et al., 2004; Wu et al., 2011] have concluded that negative NBEs typically occur at heights above ~15 km while most positive NBEs occur at altitudes of 7 - 15 km. most - CG flashes, however usually initiate at altitudes < 7 km. Therefore, negative NBEs that initiate negative cloud to ground flashes should also initiate at low altitude. The Autor has investigated the characteristics of low altitude negative NBEs and their role in initiating negative cloud-to-ground (-CG) flashes.

The second investigation has determined the source power of positive NBEs that clearly initiate intracloud (IC) flashes. Wu et al. [2014] observations showed that initiator-type positive NBEs (i.e., NBEs occurring as the initiating events of lightning flashes) can be identified among positive NBEs from their discharge heights. The author has extended the Wu et al. [2014] study by including the VHF source powers of the initiator-type positive NBEs and the types of NBEs as defined by Karunarathne et al. [2015].

The third and the final part of this dissertation considers occurrences of NBEs that do not initiate a lightning flash; these NBEs are either isolated in time and space from lightning flashes or occur during a flash rather than at the beginning. Understanding NBEs that do not initiate lightning may help explain the mechanism of NBEs in general.

CHAPTER 2

INSTRUMENTATION

In this chapter, the descriptions of the detection instruments in different frequency bands and their data used for this study will be explained. Four instruments were used and were called: Fast Antenna, Slow Antenna, dE/dt antenna and Log-RF antenna. Especially, the dE/dt and Log-RF antennas will be explained in detail, since they were specially developed, customized and built for this experiment. In addition, the data processing will be discussed. For the lightning data collection seven sets of the four antennas were distributed at 7 sites in and around Oxford, Mississippi.

2.1 Electric field change meter

Fast Antenna (FA) and Slow Antenna (SA) used in this study was essentially calibrated flat plate antenna. In order to measure the electric field change, it is necessary to integrate the signal from the antenna using an integrated circuit with a capacitor (C) on it. In addition, the electronic decay time constant of the active integrator is given by the product of its feedback resistance and the integration capacitor. The physical appearance and its operation were identical to the fast and slow antenna described in Karunarathne et al. (2013) and were also described extensively in Karunarathne et al. (2013). In brief, the operation can be explained using the following equation (e.g., Krehbiel, 1979; Karunarathne, 2013; Jerauld, 2007):

$$\Delta V = \frac{\epsilon_0 A_{eff}}{C} \Delta E \quad (2.1)$$

Here, the voltage output (ΔV) of the FA or SA is proportional to the E-change (ΔE), with the coefficient of proportionality $\frac{\epsilon_0 A_{eff}}{C}$, where ϵ_0 is the permittivity of the vacuum, C is the feedback capacitance, and A_{eff} is the effective area of the antenna.

The frequency bandwidth of the fast antenna was 16 Hz - 2.6 MHz, while the bandwidth of the slow antenna was 0.16 Hz – 2.6 MHz; therefore, the "characteristic length" (speed of light / frequency) of the electromagnetic waves detected by the antenna was greater than 120 m for both antennas. The electronic decay time of FA was 10 *ms*, which is relatively long compared to most of the sensors with this name (e.g., Kitagawa and Brook, 1960), while the slow antenna had a relatively long electronic decay time of 1.0 s. Because it has a long decay time constant compared to the fast antenna, the slow antenna has a high sensitivity for electrostatic changes. The E field sensors described above measure only the vertical component of the field, regardless of whether there is a horizontal component. The capture of Lightning data for each antenna was digitized by a digitizer of 10 MS / s, 12 bits and recorded on the computer.

2.2 dE/dt antenna

Time derivative of electric field signatures of the lightning activities were measured using Electric field derivative antenna (dE/dt), as shown in Figure 2.4(d). The antenna consists of two circular aluminum flat plates 15 cm apart from each other.

The top plate was essentially isolated from the lower plate using a Teflon cylindrical separator with a 5 cm diameter, while the bottom plate serves as the ground plane for the antenna.

The bottom plate was supported by a 30 cm long hollow Aluminum cylinder with Teflon on it. Threaded metal rod that passes through the hollow Aluminum cylinder was connected to the top plate. The threaded rod provided the necessary electric connection, as well as the support to the top plate while it was isolate from the remain system. In additionally, the other end of the threaded rod was connected to the SO-239 female connector. Antenna was connected through a 50 cm long $50\ \Omega$ BNC cable to an amplifier circuit on the side of the plastic box. The amplifier circuit input was terminated by a $50\ \Omega$ resister. Thus, its characteristic impedance is $Z_0(50\ \Omega)$. The diagram of the amplifier circuit can be found in Appendix A.

When there is an external electric field, the output voltage (ΔV) of the antenna system is proportional to the vertical component of dE/dt . The vertical component of E is more dominant in the dE/dt measurement at ground level. Because the flat ground is perfectly conductive with boundary conditions, it must be considered that the horizontal component of the E zero. however, that the finite conductivity of the Earth could lead to a non-zero horizontal component of E .

However, the horizontal component is present, the vertical component remains dominant and interest here. Weidman and Krider (1980) show that relationship between ΔV and dE/dt is as follows.

$$dE/dt = \Delta V / (\epsilon_0 A_{eff} Z_0) \quad (2.2)$$

where ϵ_0 is permittivity of free space, A_{eff} is the area of the sensor plate (top plate). As with the fast antenna or slow antenna, overall gain of the ideal flat plate dE/dt antenna is not affected by the capacitance of the antenna (e.g., Jerauld et al. 2007).

However, the effective area of the detection plate depends on the location of the configuration and the surrounding environment. therefore, the sensor near ground level is less sensitive than the sensor on the roof (e.g., Krehbiel et al., 1979; Shao et al., 2006). Choosing an appropriate gain for amplifier circuit is very important for the experiment. However, increased sensitivity can cause the antenna to become saturated for nearby Lightning activities. While, less sensitive antenna system cannot see the activities of Lightning that are far from the antenna.

The experimental frequency response plots for dE/dt antenna is shown in Figure 2.1. The experimental gain of the dE/dt antenna was 43 (32.7 dB). The lower 3db frequency could not be determined exactly from the experiment, since it is quite close to zero. The upper 3dB frequency was 2.5 MHz. The dE/dt antenna output voltages were digitized with a digitizer (PCI-DAS4020/12) of 10 MS/s, 12-bit and recorded at sample rates 10 MS/s in the computer.

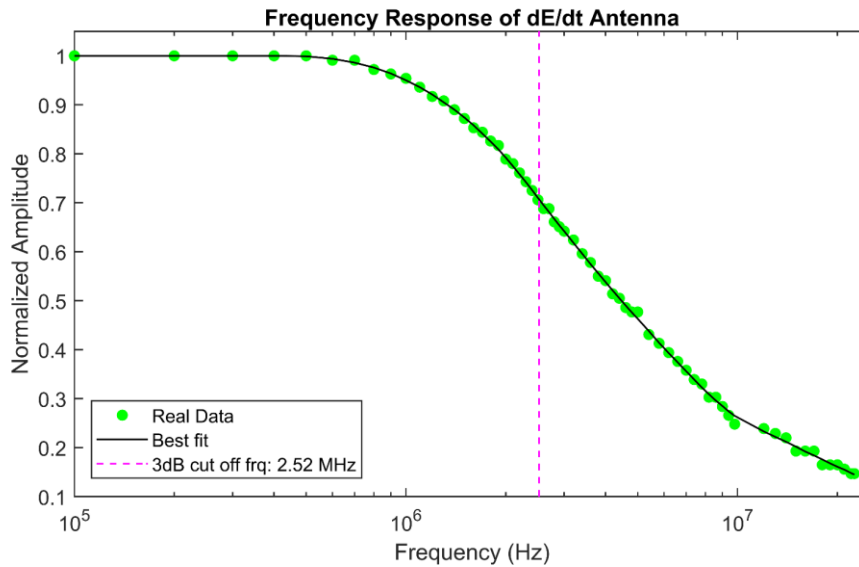


Figure 2.1. Band widths of dE/dt antenna

2.3 Log-RF antenna

The Log-RF antenna was completely designed using a commercially available component (e.g., VHF antenna, band pass filters, wideband amplifier, power detector). Figure 2.2 shows the layout of the electronic components of the Log-RF antenna. The components were interconnected by a short-length coaxial cable (LMR-195, 50Ω). To minimize background noise and provide good insulation, the sensitive part of the system protects with two separate aluminum enclosure.

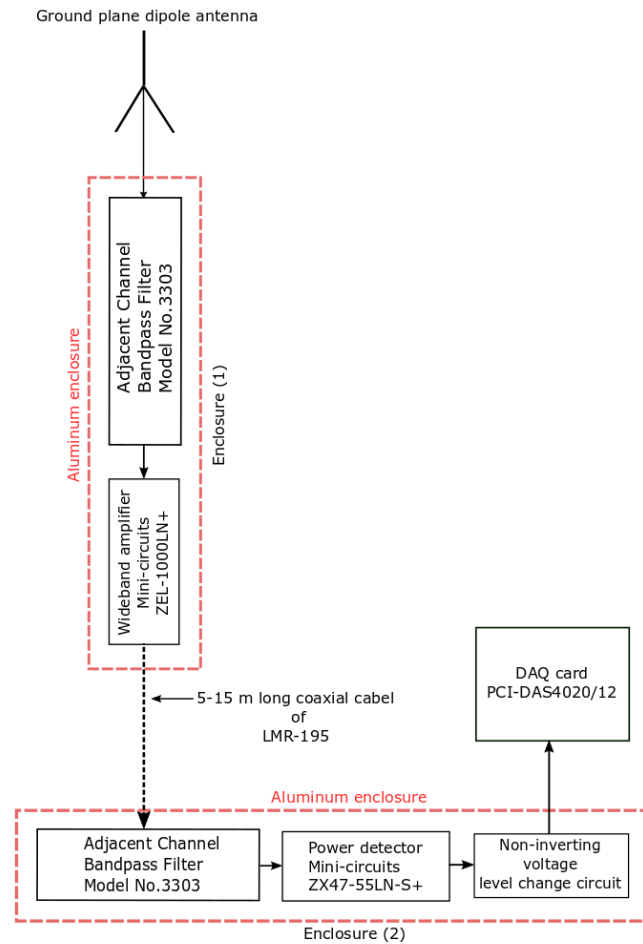


Figure 2.2. Electronic component design of the Log-RF antenna system

As shown in Figure 2.2, the bandpass filter and broadband amplifier located inside the Enclosure (1), which are close to the receiving antenna. While the second band pass filter, Log power detector, and the non-inverter level change circuit were assembled within the Enclosure (2). The Enclosure (2) was located near the digitizer and output from the Enclosure (1) connect through 5-15 m long coaxial cable (LMR-195, 50 Ω) to input of Enclosure (1). VHF receive antenna which is $\lambda/4$ ground plane, omnidirectional, and dipole antenna. The antenna was vertically mounted on near the ground or roof. The antenna has peak receive performance at 137-470 MHz and 820 -870 MHz. The Log-RF antenna system is capable of detecting the VHF radiation power emitted by Lightning in different breakdown process, between the frequency band of 184-190 MHz.

At operation, the VHF signal captured by the receiving antenna passes through a 100 cm long coaxial cable to the bandpass filter of channel -9 to block the frequency other than the desired frequency band. The signal is then amplified to +23 dB by the low noise broadband amplifier. After the amplification, the signal propagates through a coaxial cable (5-15 m) to the Enclosure (2). After entering the signal to the Enclosure (2), the signal passes through the additional bandpass filter for an additional filtering process. Then the signal is converted logarithmically using the Log power detector. The system is quite smiler to LMA system describe in Hamlin et al. (2004). The DC output voltage of the Log-power detector varies approximately from 0.50 to 2.10 V and the anlog input of the DAQ card (PCI-DAS4020/12) can operate in two programmable ranges ± 5 and ± 1 V. Choosing a dynamic range of ± 1 V instead of ± 5 V on the DAQ card can improve the resolution of the A / D conversion. Therefore, the output voltage recording of power detector was scaled again between -1 and +1 V using a non-inverting level change circuit befor it send it to DAQ card.

Circuit diagram and the operation of non-inverting level change circuit are explained in Appendix A. Finally, data were digitized and recorded at 10 MS/s with a bit depth of 12. The Log-RF sensors were calibrated according to the method used by Hamlin (2004), so that the known external reference powers were placed on the VHF antenna terminal and the resulting voltage was measured from the DAQ card.

2.4 Log-RF antenna group delay estimation

Knowing the group delay of the Log-RF antenna system is crucial to compare the signal waveform of the FA, SA and dE/dt antennas with the signal of the Log-RF antenna. However, delay introduced from the environmental factors are complex and is beyond the scope of this study. Group delay or electrical delay is typically introduced by the bandpass characteristic of filters, amplifiers, power detector, and coaxial cables in Log-RF antenna. In most cases, the band-pass characteristics of the Log-RF antenna can have a large influence on the group delay of the system. It is worth to note that time resolution of Log-RF data is $0.1 \mu s$. Therefore, any delay that is introduced from the component of the Log-RF system has less than $0.1 \mu s$ is negligible. In addition, within each detection station, each type of antenna had used coaxial cables of equal length to transmit the signal from the antenna to the DAQ card. Thus, the delay presented by the coaxial cables was neglected for the current study.

The group delay of a bandpass filter was calculated using a Microwave Network analyzer (N5242A PNA-X) by obtaining the S21 data in a frequency range of 187-192 MHz. S21 is the ratio of the voltage out of the Device Under Test (DUT) to the voltage in. S21 data from the network analyzer include the “unwrapped” phase as well as magnitude. Group delay (τ) is defined as the negative derivative of the phase (ϕ) (in degrees) with respect to frequency f :

$$\tau = -\frac{1}{360^\circ} \left(\frac{\Delta\phi}{\Delta f} \right) \quad (2.3)$$

According to the Equation 2.3, the input signal has a different frequency that passes through the filter will change the phase of the output signal. Because the signal with the lowest frequency component has a longer wavelength than the signal with the higher frequency component, it will go through fewer cycles that pass through the filter. Using Equation 2.3, it is easy to show that the relationship between frequency and phase is a straight line.

$$\Delta\phi = (360^\circ \cdot \tau) \cdot \Delta f \quad (2.4)$$

According to eq.2.4, group delay of the filter can be obtained by using the slop of the phase vs frequency graph.

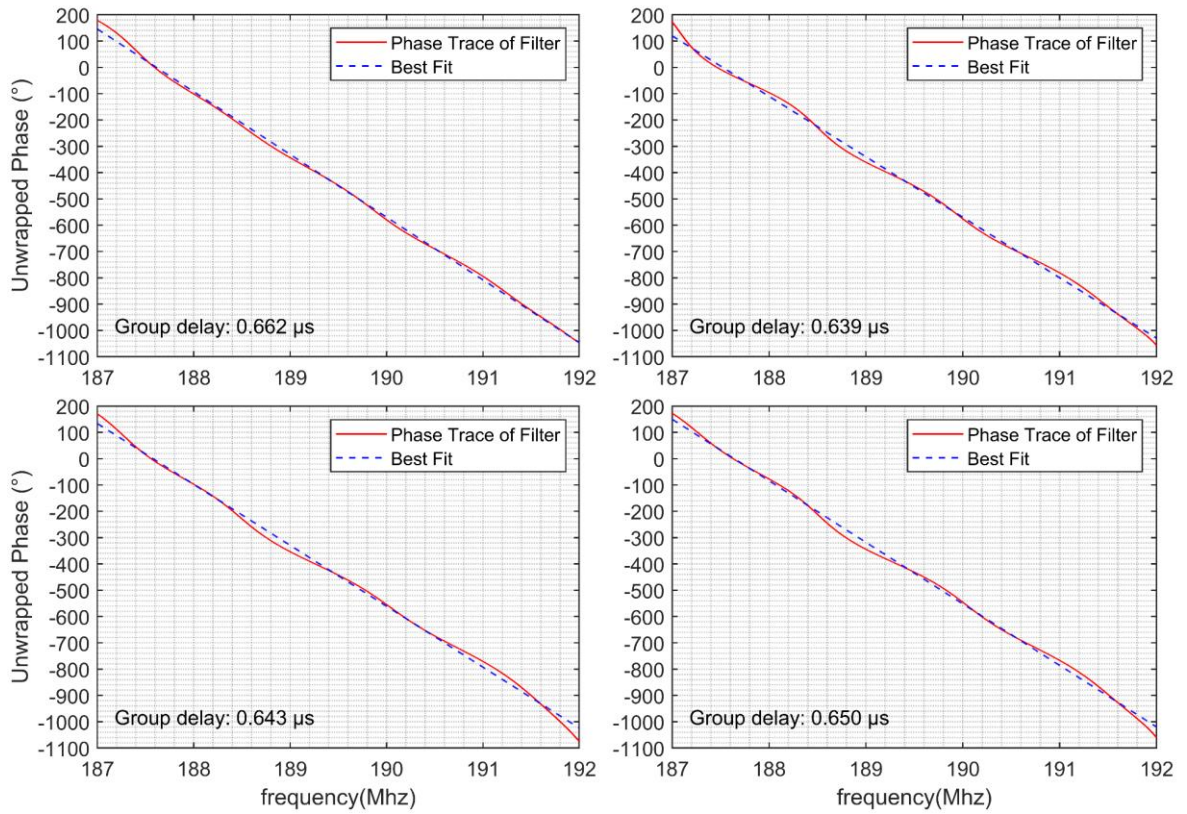


Figure 2.3. Phase response of 4 different bandpass filter (Model No.3303 channel S50-9). Each plot includes the result of the measurement for the individual S21 phase scan of the bandpass filter and its best linear fit

The results of the phase tracking for 4 different bandpass filters in the frequency range of 187-192 MHz are shown in Figure 2.3. The group delay calculated from the slope of the graphs were 0.662, 0.639, 0.643 and 0.650 μs , respectively. All 4 bandpass filters had a very similar delay, since the slope of all the graphs is very similar. Slightly different between those numbers could be due to manufacturing process of filter. The group delay for the single bandpass filter was determined by averaging the previous values. The Log-RF system was composed of 2 band filters so that the overall signal delay for the Log-RF system in this study was conceded as 1.3 μs .

2.5 Array configuration and operation

Multiple Lightning observation stations were deployed in and around Oxford, Mississippi, USA in the summer of 2016. The array system comprised seven lightning detection stations and each station's name is given by a two or three-character identification code (EE, FS, IH, JM, SS, TM, and NDS). And They were located within 17 km of the EE site (which serves as the origin of our coordinate system), plus a seventh site (identified as NDS) located 43 km WSW of the EE site. Each station is equipped with four sensors: two E-change sensors (FA and SA), a dE/dt , and a Log-RF. The array capable of detecting lightning radiation from normal lightning discharges within 50-60 km effectively, therefore, only the strongest lightning event at ~ 200 km distance can be detected. Three of the sensor sites in the array (JM, TM, and SS) were operated by two 12 V batteries and sensor were mounted 1-3m above ground on two sides of a heavy-duty metal box.

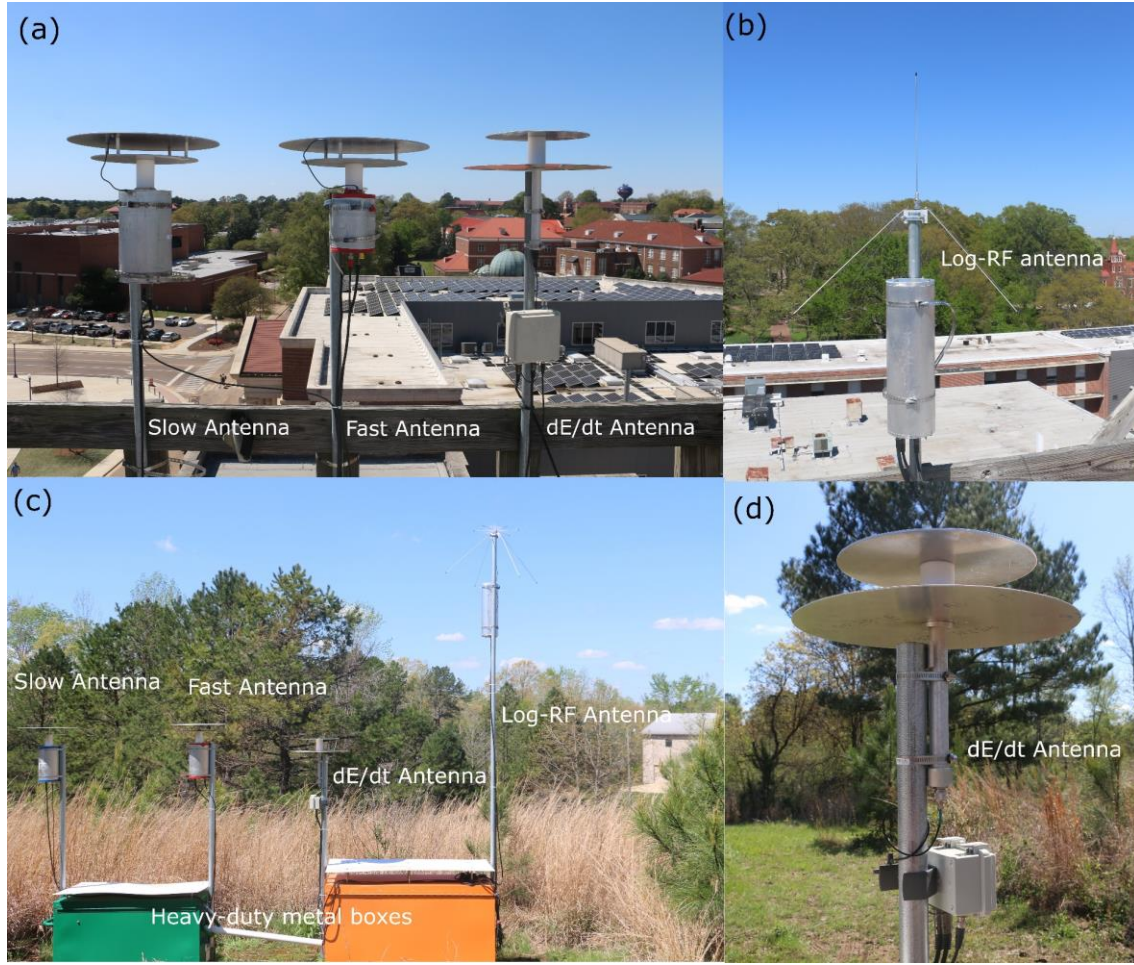


Figure 2.4. Sensor arrangement of EE and SS sites. The EE sensors were mounted on top of three-story building (Anderson Hall) and were operated by AC power: (a) left to right: slow antenna, fast antenna, dE/dt antenna and (b) Log-RF antenna. (c) Similar sensor arrangement at SS site: slow antenna, fast antenna, dE/dt antenna and Log-RF antenna were mounted on both sides of a metal box and were operated by two 12 V automobile batteries. (d) Close-up view of dE/dt antenna.

The rest of them were mounted on roof tops and operated on AC power. The example of the sensor arrangement is shown in Figure 2.4. At each site, the data from the four sensors were digitized simultaneously with 10 MS / s, 12 bits using two separate DAQ cards. The fast antenna and the Log-RF were connected separately to one of the DAQ card and the dE / dt and slow antenna were connected to the second DAQ card. The two DAQ card were triggered by the FA whenever a floating threshold was exceeded by an E-change pulse. As described in Karunaratne et al. (2013) the data were digitized in two modes, continuous and triggered.

In the continuous mode, 10 MHz, 12-bit data from all sensors were separately down-sample to 10 *KHz* and continuously recorded on the computer. In trigger mode, the triggered data of FA, SA, dE/dt and Log RF antenna were recorded on the computer at sampling rate 5, 5, 10, and 10 MS / s, respectively. Further, each trigger a 400 *ms* data record with 250 *ms* of pre-trigger and 150 *ms* of post-trigger was stored in computer. Any new FA trigger during the post-trigger period would extend the post-trigger period by 150 μ s from the time of the new trigger. These data were time stamped using Global Positioning System (GPS) pulse-per-second output (with a 1 sigma average less than 2 ns).

CHAPTER 3

DETERMINING THE LOCATION OF LIGHTNING EVENTS

In this chapter, the most widely used method for locating lightning pulses detected with the E-change and electric field derivative antenna array will be briefly explained. where a 3D source location is calculated from the difference in arrival time (TOA) of a signal in five or more measurement stations. Furthermore, two types of data used to locate natural Lightning events in the TOA technique will be provided in this study.

By measuring the arrival time of the lightning pulses using an array of electric (E) or magnetic (B) field change sensors, it can be used to obtain the position of the Lightning source in spacetime. Therefore, Time of Arrival (TOA) is a widely used technique for locating Lightning sources. The time of arrival of the signal (t_i) to a given sensor i associated with the unknown time of source (t) whose location coordinate is (x, y, z) can be written as follows:

$$t_i = t + \frac{1}{c} \sqrt{(x_i - x)^2 + (y_i - y)^2 + (z_i - z)^2} \quad (3.1)$$

Where c is the propagation speed of signal, (x_i, y_i, z_i) are receiver coordinates. A similar non-linear Equation can be obtained for j^{th} station by replacing i with j . Arrival time difference for set of two receiving antennas (i, j) :

$$c(t_i - t_j) = \sqrt{(x_i - x)^2 + (y_i - y)^2 + (z_i - z)^2} - \sqrt{(x_j - x)^2 + (y_j - y)^2 + (z_j - z)^2} \quad (3.2)$$

The result is a basically an equation for a hyperbola with three unknowns (x, y, z) . Having at least four different antennas will produce three such hyperbolas. Therefore, one way to obtain the location of source using the TOA technique is to find the intersection location of those branches of hyperbolas (e.g., Proctor, 1971). Another way to obtain the location of the sources using the TOA technique is by taking the square form of Equation 3.1 and taking the difference of arrival time for pairs of stations, as mentioned above. It will produce a linearized equation with 4 unknowns (x, y, z, t) . Having equations for 5 stations gives 4 equations that are linear in the 4 unknowns, x, y, z, t . Therefore, they can be used to obtain analytical solutions of four unknowns (e.g., Koshak and Solakiewicz.,1996; Hamlin et al.2004; Bitzer et al. 2013; Karunarathne et al. 2013;).

Karunarathne et al. [2013] used TOA with electric field change (E-change) data from 10 sites to find pulse locations; they called this technique PBFA (for “position by fast antenna”). In addition to that, Monte Carlo technique has been used to estimate (x, y, z, t) errors. Karunarathne et al. [2013] focused on two types of lightning pulses: initial breakdown pulses and return strokes.

The arrival times that are identified from the dE/dt pulses can also be used to find the source location of the pulses in the 3-D TOA technique. Jerauld et al. (2007) used 2-D TOA technique with an array of 4 dE/dt sensors to determine time and space locations of lightning return strokes. However, it was found that the numerically integrated dE/dt can give a similar waveform with a better resolution compared to the directly measured E waveforms. Therefore, the peaks of numerically integrated dE/dt waveform instead of E-change were also used to calculating the time differences that are need for the 3-D TOA technique, which was describe Karunarathne et al. (2013).

Trapezoidal approximation method was used to perform the numerical integration of the dE/dt record. In addition, the integration precision was increased by linearly interpolating the dE/dt data to 60 MS / s prior to integration. Numerical integration of the dE/dt waveforms were severely affected by the vertical displacement (DC component) in the dE/dt waveforms. Therefore, any linear trend associated with the dE/dt waveforms was carefully eliminated before integration. In this study, All the pulse location of Lightning data presented herein are determined either PBFA or $\int dE/dt$.

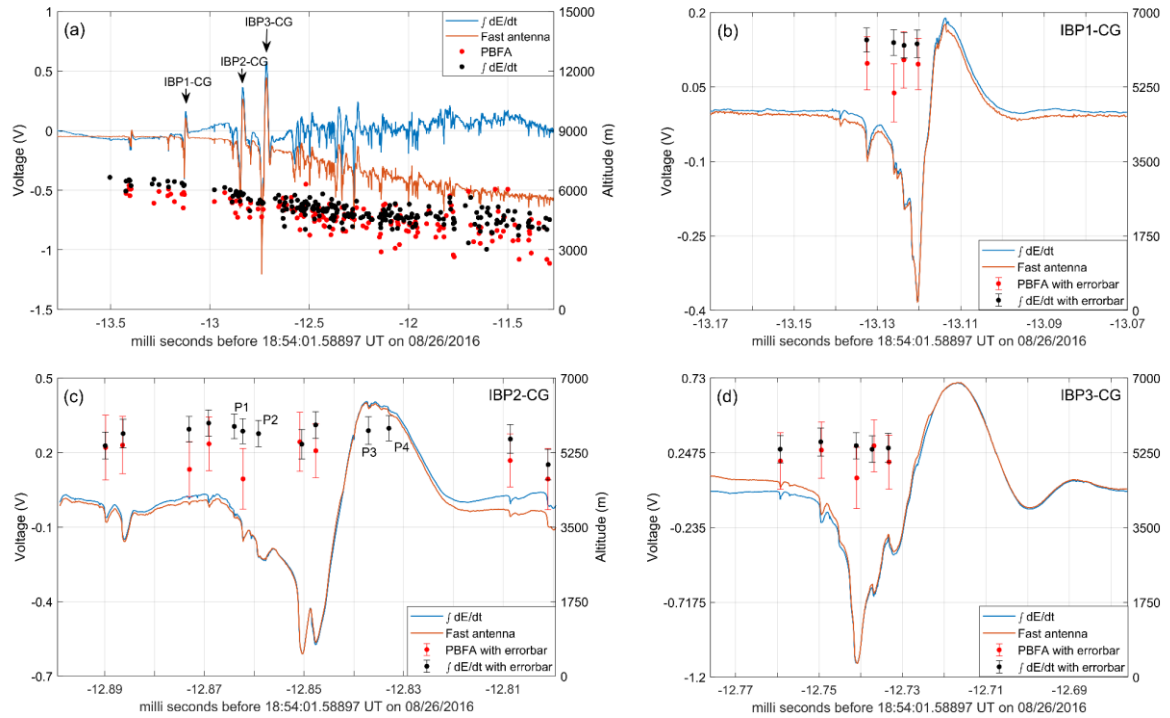


Figure 3.1. Comparison of PBFA and $\int dE/dt$ methods for pulse altitudes (z) in CG flash. (a) First 2.5 ms of initial breakdown pulses of CG flash with data from FA (Light brown) and integrated dE/dt (blue) sensors. Altitudes of the pulses (right axis) were determined from TOA of FA data (PBFA, red) and TOA of integrated dE/dt data ($\int dE/dt$, black). (b)-(d) Detailed expansion of the IB pulses (IBP1-CG, IBP2-CG, and IBP3-CG) in (a). PBFA and $\int dE/dt$ altitude errors are represented by error bars. P1, P2, P3 and P4 indicate that the altitude positions in (c) could not be determined using PBFA.

Figure 3.1a shows an example of integrated dE/dt data compared to corresponding E-change data. The lightning data in the figure shows first 2.5ms of initial breakdown pulses of single-stroke CG flash occurred on 08 August 2016. The altitudes of the pulses (determined from the full array of sensors) are shown time versus altitude (right axis) and were identified from TOA of E-change data (PBFA, red) and TOA of integrated dE/dt data ($\int dE/dt$, black). Figure 3.1.(b)-(d) shows the detailed expansion of IBP1-CG, IBP2-CG, and IBP3-CG (different location) illustrating comparison of E-change data and integrated dE/dt waveforms. Each integrated dE/dt waveform was scaled to match the corresponding E-change data. This result indicates that the waveforms of the integrated dE/dt are in accordance with the waveforms of change E. in addition to that for most pulses, the altitude error bars PBFA and $\int dE/dt$ overlap shows good agreement with the pulse altitude. However, the $\int dE/dt$ error bars are smaller than the PBFA bars because the time resolution of $\int dE/dt$ is $0.1 \mu s$ versus $0.2 \mu s$ for PBFA. It is interesting to note locations P1, P2, P3, P4 in figure 3.1.a could not be determined using PBFA but were determined using $\int dE/dt$. Thus, $\int dE/dt$ best suited for locating small pulses.

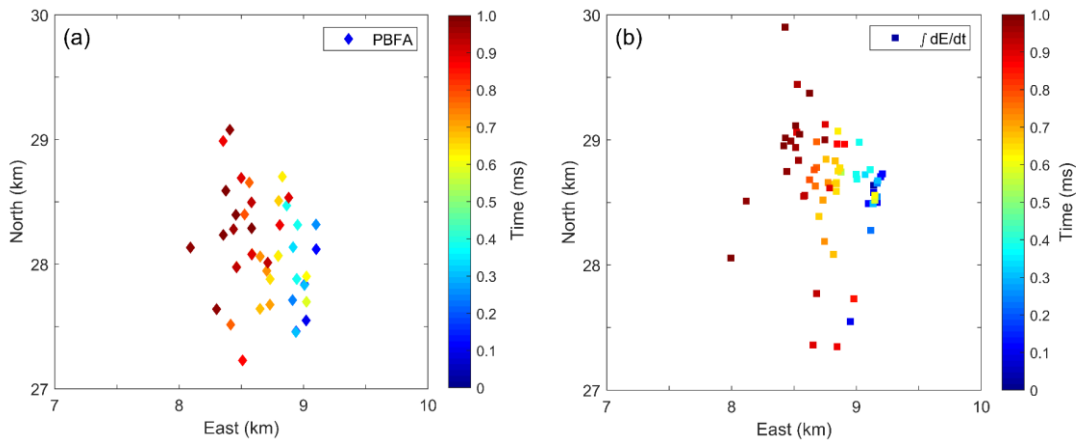


Figure 3.2. Comparison of PBFA and $\int dE/dt$ methods for Horizontal pulse positions (X-Y) in CG flash. (a) X-Y locations of IB pulses during the first 1ms of the flash, determined by PBFA. (b). same pulses determined using $\int dE/dt$

Figure 3.2 shows the (X-Y) or Horizontal locations of CG pulses during the first 1ms of the above flash, determined using PBFA (a) and $\int dE/dt$ (b). Note that both techniques give a similar time and space development of the pulse events, but the $\int dE/dt$ locations are more tightly clustered, which may be due to their time resolution.

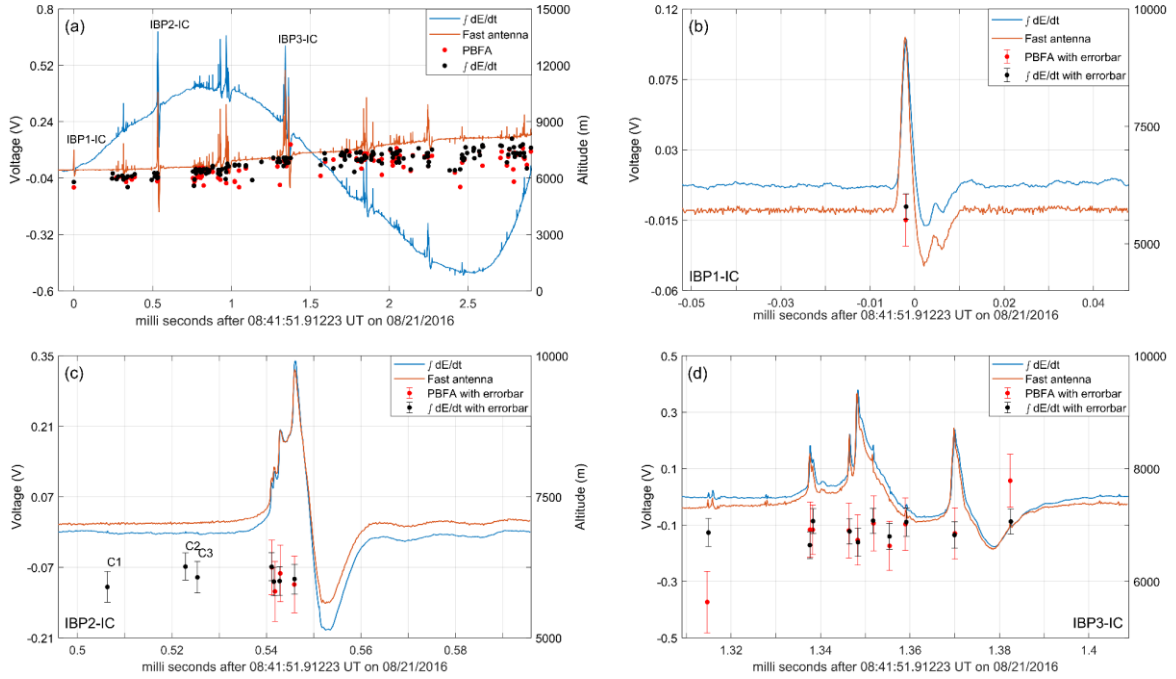


Figure 3.3. Similar to Figure 3.1, which shows another comparison example of the PBFA and $\int dE/dt$ methods for pulse altitudes in IC flash. Similarly, C1, C2, and C3 show that the altitude positions in (c) could not be determined using PBFA.

Another example comparison of the PBFA and $\int dE/dt$ methods is shown in figure 3.3, which shows the E- change and the corresponding data of dE/dt during the first 3 ms of a flash IC on 21 August 2016. Slow oscillation behavior of integrated dE/dt in figure 3.3.a is a clear artifact, but the agreement between integrated dE/dt and E-change for individual pulses (e.g., IBP1-IC, IBP2-IC, and IBP3-IC) is quite good. Note that the locations C1, C2, and C3 in (c) could not be determined using PBFA but were determined using $\int dE/dt$.

In addition, the overlay error bar for the individual altitude location given by two methods indicates a reasonable agreement between the altitude locations of the pulses determined from the integrated dE/dt and E-change data.

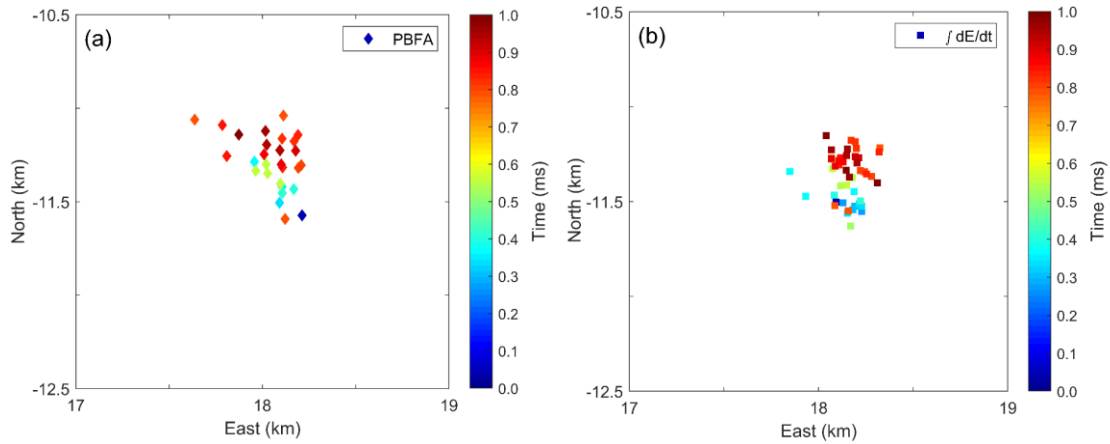


Figure 3.4. Similar to Figure 3.2, shows an example of X-Y location comparison in 2 methods for IB pulses during the first 1ms of the IC flash

Figure 3.4 shows the space and time development of the individual IB pulses of 1ms at the beginning of the IC flash. both techniques give a similar time and space development of the pulse events. However, PBFA are more dispersed in space in contrast to $\int dE/dt$. So $\int dE/dt$ give can give denser or higher resolution Lightning location images than PBFA.

3.1 Summary and Conclusions

The wave shapes of integrated dE/dt pulses were in good agreement with E-change pulse wave shapes, although static changes in the pulses are not seen in the integrated dE/dt data due to elimination of DC-offset in the dE/dt waveforms prior to integration. Also, integration artifacts sometimes occur on millisecond time scales, but these artifacts are easily ignored and do not seem to interfere with correct determination of pulses location.

There was good agreement between pulse locations determined using E-change data (PBFA) and dE/dt data ($\int dE/dt$). In general, the PBFA locations are slightly more scattered than the $\int dE/dt$ locations. The $\int dE/dt$ locations are probably better and more tightly clustered because the time resolution of the integrated dE/dt is $0.1\mu\text{s}$ while the time resolution of the E-change data is $0.2\mu\text{s}$. in addition to that, with our sensors, smaller pulses are more easily seen using the integrated dE/dt data than the E-change data and this is one of the advantages over PBFA.

CHAPTER 4

CHARACTERIZING THREE TYPES OF NEGATIVE NARROW BIPOLAR EVENTS IN THUNDERSTORMS

In this chapter, data from fast antennas (FAs) with bandwidth $16\text{ Hz} - 2.6\text{ MHz}$ and VHF power sensors (Log-RF) with bandwidth of $186\text{--}192\text{ MHz}$ will be used to examine negative narrow bipolar events, or NNBEs. The main focus in this chapter is on low-altitude ($<8.0\text{ km}$) NNBEs that initiate negative cloud-to-ground (-CG) flashes; very few low-altitude NNBEs have been studied previously.

4.1 Introduction

Narrow bipolar events (NBEs) are a type of electrical discharge associated with thunderclouds (e.g., Karunarathna et al., 2015). (NBEs are also known as narrow bipolar pulses, or NBPs, and as compact intracloud discharges, or CIDs.) LeVine (1980) first identified NBEs and stated, based on measurements using the HF and VHF radio bands, that NBEs were “the sources of the strongest RF radiation during lightning.” With an electric field change sensor (called an “E-change” sensor or “fast antenna” herein) with a bandwidth of $500\text{ Hz} - 2\text{ MHz}$, LeVine (1980) found that an NBE produced a bipolar pulse with a short duration ($10 - 20\text{ }\mu\text{s}$). LeVine (1980) described the bipolar NBE as having “an initial negative half cycle followed by a positive overshoot”; we will use “initial half cycle” and “overshoot” to describe the two opposite polarity parts of the NBE bipolar pulse. NBEs were originally

thought to be temporally isolated from other lightning discharges (e.g., Willett et al., 1989; Smith et al., 1999), but Rison et al. (1999) showed that some NBEs initiate intracloud (IC) flashes, and Karunarathne et al. (2015) found that among 226 NBEs, only 37% occurred with no other lightning event within 10 km and 660 ms. Using the physics definition of electric field polarity, Willett et al. (1989) noted that NBEs can be either positive or negative based on the polarity of the initial deflection of the bipolar electric field change pulse. Ahmad et al. (2010) compared the characteristics of positive and negative NBEs detected in Malaysia. Herein we focus on negative NBEs (NNBEs).

Smith et al. [2004] located more than 100,000 positive and negative NBEs in the USA and found that the majority of positive NBEs occurred at altitudes of 7-15 km and the majority of NNBEs occurred at altitudes of 15-20 km, but small numbers of both types of NBEs were located down to an altitude of 4 km. Wu et al. (2012) studied the altitudes of more than 8000 NBEs in China and found that most NNBEs occurred between 16 and 19 km altitude while most positive NBEs occurred between 8 and 16 km, though the minimum altitudes of NNBEs and positive NBEs were 7.0 and 6.4 km, respectively. Wu et al. (2011) determined that their NNBEs (all 174 of which were located at altitudes of 15 – 20 km) had on average larger range-normalized E-change amplitudes than 555 positive NBEs, with the ratio of their respective geometric mean values being 1.4. We refer to these high altitude NNBEs as typical NNBEs or NNBE(T).

Using an HF/VHF digital interferometer, a VHF Lightning Mapping Array (LMA), and a fast antenna, Rison et al. [2016] reported that positive NBEs initiate most or all IC flashes and that NNBEs initiate most or all negative cloud-to-ground (-CG) flashes. Since -CG flash initiations typically occur below 7 km altitude, the initiating NNBEs represent a previously unknown group of low altitude NNBEs.

For NBEs detected with the interferometer, Rison et al. (2016) found that the positive NBEs initiating IC flashes had VHF powers in the range 0 – 53.5 dBW while the NNBEs initiating -CG flashes were much weaker, 2 to 28 dBW. In addition, the waveforms of the NNBEs initiating -CG flashes had a “more monopolar” electric field change rather than the usual bipolar waveform; i.e., the NBE overshoot was missing or was very small. We refer to this type of NNBE as “hump-like” or NNBE(H).

Marshall et al. (2014) and Chapman et al. (2017) showed that most or all -CG flashes and intracloud (IC) flashes begin with an impulsive initiating event, followed by an initial E-change (or IEC) that may include one or more short-duration low-amplitude initial breakdown (IB) pulses, followed by the first classic IB pulse (or “1stCIBP”). (A “classic” IB pulse is defined herein as having a bipolar waveform, a duration $\geq 10 \mu\text{s}$, and a relatively large amplitude; classic IB pulses often have one or more “subpulses” on the initial half cycle of the bipolar waveform (Weidman and Krider, 1979). We note that this definition of classic IB pulse is not based on a particular physical mechanism, so the $10 \mu\text{s}$ minimum duration is somewhat arbitrary.) As shown by Rison et al. (2016), the impulsive initiating event may sometimes be an NBE.

However, Marshall et al. (2019) found that one -CG and two IC flashes began without a fast antenna pulse. Since a bipolar fast antenna pulse is the hallmark of an NBE, one conclusion of Marshall et al. (2019) was that some -CG and IC flashes are initiated without an NBE. Marshall et al. (2019) also found that there was a short-duration ($\sim 1 \mu\text{s}$), low-power ($< 1 \text{ W}$, or $< 0 \text{ dBW}$) VHF event initiating each of these flashes.

Herein we report on NNBEs using an array of fast antennas and VHF power detectors. After determining their waveform shape and altitude, we divided the NNBEs into three groups (including the two types described above): (1) typical, high-altitude NNBE(T)s, (2) low-altitude, hump-like NNBE(H)s, and (3) low-altitude NNBEs with normal bipolar waveforms

that we call NNBE(L)s. The NNBE(L)s are previously unreported. The two main goals of this study are to show data that indicate NNBE(H)s and NNBE(L)s initiate some but not all -CG flashes, and to characterize the properties of NNBE(H)s and NNBE(L)s, including range-normalized E-change amplitude and VHF power. NNBE data for this study were collected during July and August 2016 using a seven-site array of lightning sensors located in and around Oxford, Mississippi, USA. Detailed description of the lightning sensor array can be found in chapter 2.

4.2 Data and analysis methods

4.2.1 Determining NNBE Locations

In this study we sometimes used PBFA for NNBE locations whenever 5 or more sites had FA data with reasonable signal to noise. NNBEs and other Lightning pulses can also be located with $\int dE/dt$ waveforms from at least 5 sensor sites using the PBFA TOA algorithm as described in chapter 3; these locations are labeled as “ $\int dE/dt$.” Herein most of the locations of NNBEs and other lightning pulses were determined using $\int dE/dt$.

4.2.2 Calculating NNBE range-normalized amplitudes and NNBE VHF source powers

Locating the NNBEs is especially important since the locations allow us to compare our measurements with previously published data of NNBEs and of positive NBEs. For instance, a typical way of quantifying NNBE amplitudes in the FA data is to range-normalize them to 100 km using a $1/R$ dependence, where R is the slant range from the NNBE to the FA sensor.

This range dependence assumes that the NNBE E-change amplitude is dominated by “radiation” component with essentially no “induction” or “electrostatic” contributions (see Uman et al. (1975) for the definition of these terms). Herein, the words “range-normalized” will imply that the range chosen was 100 km; we also use “ $E_{100\text{km}}$ ” to indicate the range-normalized amplitude of FA pulses. The $E_{100\text{km}}$ value of NNBEs was determined by averaging the range-normalized data from all FA sensors with range > 20 km.

A typical way to quantify NBE amplitudes in the HF and VHF radio bands is to calculate the NBE source power, P_s , in watts or dBW using the Friis transmission equation (e.g., Balanis., 2005):

$$P_s = \frac{P_r}{G_s G_r \left(\frac{\lambda}{4\pi R} \right)^2 |\hat{n}_s \cdot \hat{n}_r^*|^2} \quad (4.1)$$

where P_r is the power received by the Log-RF antenna, G_s and G_r are the gains of the emitting and receiving antennas (here, the NNBE and the Log-RF antenna, respectively), R is the slant range between the NNBE and the Log-RF antenna, λ is the wavelength of the VHF radiation (~ 1.6 m for the center frequency of 189 MHz), \hat{n}_s is the unit polarization vector of the VHF radiation, and \hat{n}_r is the unit polarization vector of the Log-RF antenna.

Below we calculate the source power, P_s , of NNBEs using Equation 4.1 and express the power in watts (and sometimes in dBW, decibels relative to 1 watt). The antenna gains G_s and G_A are taken to be unity. R is known from PBFA or $\int dE/dt$ locations of the NNBEs. The expression $|\hat{n}_s \cdot \hat{n}_r^*|^2$ is the polarization loss factor (PLF) and can vary from 0 to 1 (Stutzman and Thiele, 2013). The PLF for reception of a linearly polarized wave with a linearly polarized receiving antenna is

$$|\hat{n}_s \cdot \hat{n}_r^*|^2 = |\cos \theta|^2 \quad (4.2)$$

The Log-RF receiving antenna was vertically polarized. We assume that the VHF radiation of an NNBE was isotopically emitted and was due to vertical charge motions, so it was vertically polarized. From the receiving antenna, θ was the angle measured upward from the horizontal to the NNBE; at long range θ was approximately 0 radians, so the PLF has been assumed to be 1.0. Other possible choices for the polarization (or charge motion orientation) of the NNBEs are discussed below.

4.2.3 Identification of typical NNBEs

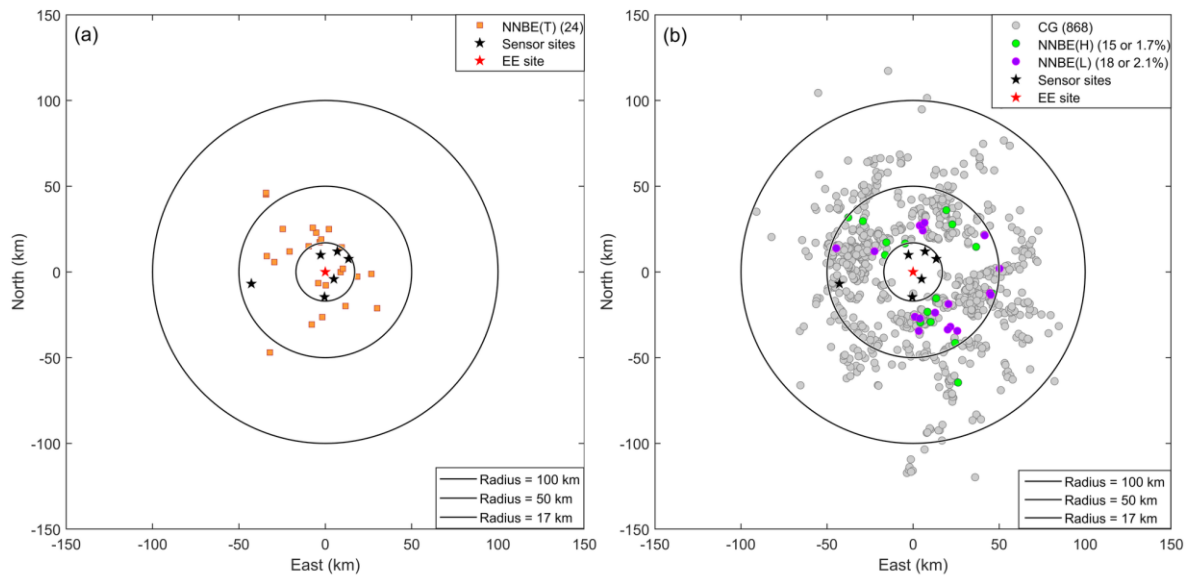


Figure 4.1. (a) Plan view of seven sensor sites (marked with stars) along with locations of 24 NNBE(T)s (orange squares). The central sensor site, EE, is marked with the red star and is the origin of the coordinate system; three range rings are also shown. (b) Plan view of seven sensor sites along with locations of the first return stroke of 868 -CG flashes with locatable IB pulses. Of these 868 -CG flashes, 833 were not preceded by an NNBE (gray circles), 18 were preceded by NNBE(L)s (purple circles), and 15 were preceded by NNBE(H)s (green circles).

Although our main goal was to investigate the NNBEs that initiate -CG flashes, we first identified typical NNBEs or NNBE(T)s in our dataset for comparison. LeVine (1980) showed that NBEs have especially strong VHF powers; we used this fact in a search algorithm to find NNBE(T)s.

We programmatically searched each 400 ms record of triggered data obtained at the EE station for Log-RF pulses having peak amplitude greater than a threshold, which we adjusted to find only the largest Log-RF pulses. To find only negative NBEs, the program required that the initial polarity of the coincident fast antenna waveform was negative. In addition, we required that the candidate NNBE(T)s had triggered data at five or more sensor sites so that we could use either PBFA or $\int dE / dt$ to locate NNBE(T)s. Then, for each candidate NNBE(T) found in the Log-RF data, we visually examined the coincident fast antenna data to ensure that each candidate had a typical bipolar NBE waveform with a duration $< 50 \mu\text{s}$. This procedure produced 174 NNBE(T)s. For further analysis, we then focused only on NNBE(T)s with horizontal location errors Δx and $\Delta y < 2 \text{ km}$ and chi squared goodness-of-fit values < 5 , leaving a set of 24 NNBE(T)s.

These 24 NNBE(T)s occurred at altitudes above 8 km (z ranging from 8.0 – 16.3 km). The plan locations of the 24 NNBE(T)s are shown in Figure 4.1a (as orange squares); all were located within 60 km horizontal distance of the EE site.

Figure 4.2 shows one example from among the 24 NNBE(T)s. The NNBE(T) shown was isolated in time and space from other lightning events and occurred at an altitude of 15.7 km. It had a range normalized fast antenna amplitude of -17.1 V/m (the largest of the 24 NNBE(T)s) and a VHF power of 5590 W, the third largest VHF power in the group of 24 NNBE(T)s. The NNBE(T) in Figure 4.2 had a simple bipolar waveform (Type A in the classification scheme of Karunarathne et al., (2015)); the risetime of the coincident Log-RF pulse was approximately $1.3 \mu\text{s}$.

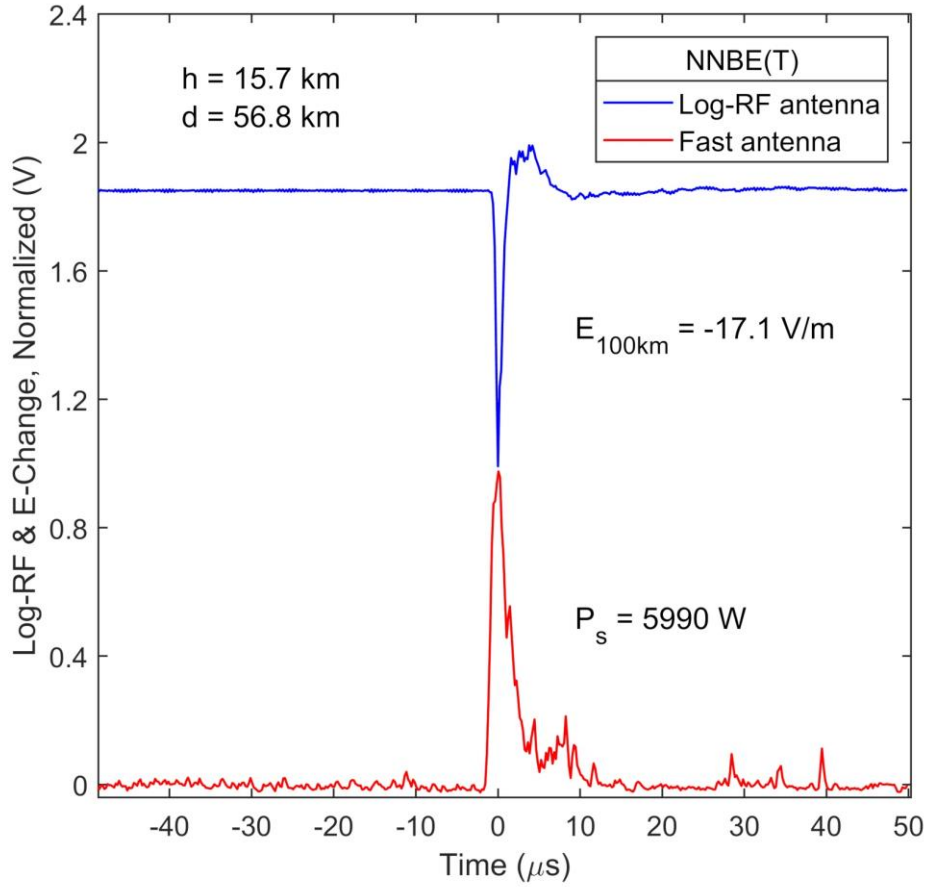


Figure 4.2. E-change (FA) and Log-RF waveforms of a typical negative narrow bipolar pulse, NNBE(T), that occurred at an altitude $h = 15.7$ km and a horizontal range $d = 56.8$ km from the sensor site. FA data (blue, uncalibrated linear scale) and Log-RF data (red, uncalibrated logarithmic scale) plotted as normalized voltage versus time (i.e., for each curve the largest peak-to-peak pulse amplitude is scaled to 1.0 V). $E_{100\text{km}}$ is the FA zero-to-peak amplitude (in V/m) of the NNBE(T) range-normalized to 100 km, while P_s is the VHF power (in watts) of the NNBE(T).

4.2.4 Identification of NNBEs preceding -CG flashes

Finding NNBEs associated with the beginning of -CG flashes was more difficult with an automated routine because NNBEs and -CG return strokes both have a large negative-going pulse in the fast antenna data. However, due to the report by Rison et al. (2016) that NNBEs initiate negative -CG flashes, we were motivated to search for such events in our 2016 dataset. In brief, the multistep procedure used to find NNBEs initiating -CG flashes were as follows.

All triggered fast antenna data from the EE station were pre-processed in the following manner before finding the triggers that included -CG return strokes. (1) down-sample to 1 MHz to smooth the data, (2) Then, the data was passed through a digital high-pass filter with a cut-off frequency of 2 kHz to eliminate the DC component of data. To efficiently identify the RS pulses, an automated procedure was applied to the processed E-change data.

The procedure first found possible RS pulses from processed electric field data looking for peak amplitude of pulses greater than the threshold value (0.4 V). In addition, we make sure that the identified pulses do not have saturated peaks. If the peak of the pulse is saturated, then the particular pulse is discarded. The threshold value used in the previous step was an arbitrary value for our automated procedure and the value was optimized by adjusting it to find the maximum number of RS pulses within the trigger window. However, the procedure was limited to collecting the subsequent RS pulses in the multiple-stroke flashes by applying the condition that successive RS pulses after each possible RS pulse within 70 ms excluded from the data set. Thus, the rest of the RS pulses are considered as possible candidates as the first RS in this study.

We assumed that the time scale of 70 ms was enough to cover at least one subsequent stroke for our data set. (e.g., Rakov et al., 1990; Fisher et al., 1993, Rakov et al., 1994). Note that applying the above condition did not eliminate all subsequent RS pulses, since some -CG flashes consisted of several successive RS pulses with inter stroke intervals greater than 100 ms. Therefore, the following automated procedure was applied to further limit the collection of the subsequent RS, as well as to identify the -CG flashes with detectable IB pulses.

The next step was to identify all the IB pulses associated with each RS pulse. The procedure was similar to that described in Zhu et al. (2016). From -80 ms to -5 ms (75 ms time window) worth of E-change data prior to each RS pulse were used to find IB pulses. The pulse having a peak amplitude greater than 3 times the background noise level and having an initial

polarity similar to that of the RS pulse was recognized as the detectable IB pulse. In addition, the RS pulse that has at least three detectable IB pulse was considered as a -CG flash with detectable IB pulses. At this stage, the procedure yielded a group of -CG flashes with detectable IB pulses. Next, we reduced this group of -CG flashes to those that also had triggered data at five or more sensor sites, so that we could use either PBFA or $\int dE/dt$ to locate NNBEs and IB pulses. Applying this procedure for all the data collected from July and August 2016, gave a total of 1279 -CG flashes with detectable IB pulses and with triggered data from at least five sensor sites. As in the case for the NNBE(T)s, for further analysis we again focused in on only the NNBEs with horizontal location errors Δx and $\Delta y < 2$ km and chi squared goodness-of-fit values < 5 . These criteria reduced the sample to a set of 868 -CG flashes. Visual inspection of the 868 -CG flashes yielded 18 cases in which the first IB pulse was preceded by an initiation event in the fast antenna data that was easily identified as an NNBE(L). The NNBE(L)s were defined as follows: each was the initial event in the fast antenna data, each had the characteristic fast antenna bipolar waveform of an NBE, each had a duration in the range of 12-38 μs , and each had a coincident peak in the Log-RF data that was the strongest peak or one of the strongest peaks in the Log-RF data. Example NNBE(L)s are presented in Figures 4.3 and 4.4 and are discussed below. Visual inspection of the 868 -CG flashes also yielded another 15 -CG flashes whose IB pulses were preceded by hump-like NNBE(H)s in the fast antenna data. The NNBE(H)s were defined as follows: each was the initial event in the fast antenna data, each had the “more monopolar” waveform described by Rison et al. (2016) rather than the typical bipolar NBE waveform, each had a duration in the range of 8-21 μs , and each had a coincident with Log-RF peak that was relatively large, though generally weaker in power than the NNBE(L)s. Two NNBE(H) examples are presented in Figures 4.5 and 4.6 and discussed below.

Thus, we found 18 NNBE(L)s and 15 NNBE(H)s in the group of 868 -CG flashes, so only about 4% of the -CG flashes were preceded by a NNBE. Below we show that these 33 flashes were apparently initiated by the NNBEs.

Unlike the NNBE(T)s, the 15 NNBE(H)s and 18 NNBE(L)s all occurred at altitudes below 8.0 km (4.5 – 7.8 km). Figure 4.1b shows the plan position of the first return stroke of the 868 -CG flashes (mostly marked in gray); the 33 -CG flashes preceded by NNBE(H)s or NNBE(L)s are marked in green and purple, respectively. If D is the horizontal distance of a flash location from the EE site, then the 868 -CG flash locations were bounded by $12 \text{ km} < D < 125 \text{ km}$. The effective upper limit of flash distances in this set is due to the requirement that the IB pulses were detected at 5 or more sites, while the effective lower limit is due to the fact that our identification procedure did not work if the first return stroke saturated the EE fast antenna, as happened at shorter ranges.

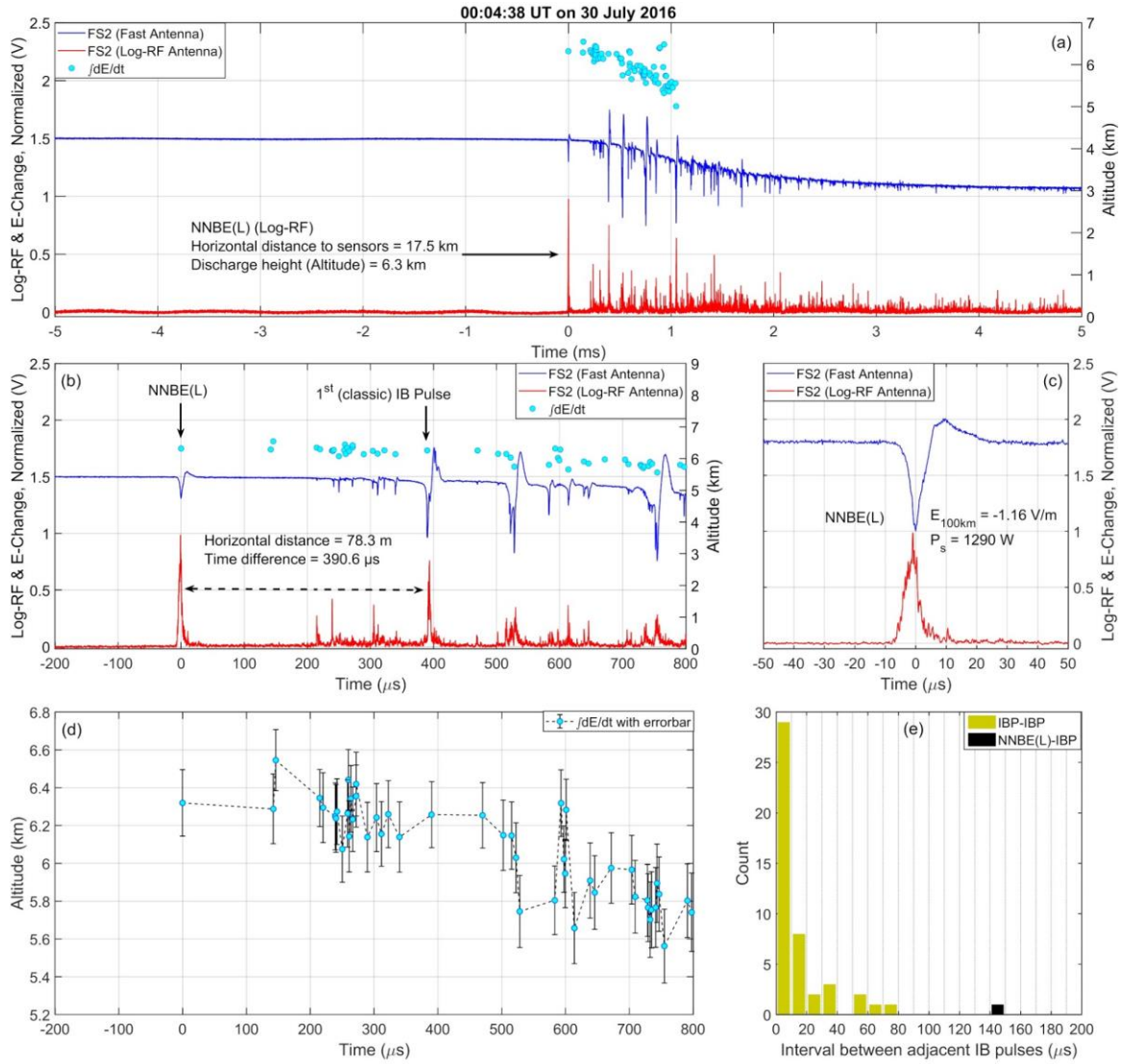


Figure 4.3. Example of an NNBE(L) that apparently initiated a -CG flash. The FA data and Log-RF data are both shown as normalized voltages (as in Figure 2). (a) Overview showing 10 ms of FA data (blue) and Log-RF data (red). Light blue dots represent altitudes (right-hand vertical scale) of FA pulses determined using $\int dE/dt$. Altitude of the NNBE(L) was 6.3 km. (b) Expanded view (1 ms) of first events in (a). (c) Expanded view (100 μ s) of the NNBE(L). (d) FA pulse altitudes with error bars for the same 1 ms shown in (b). (e) Histogram of time intervals between successive FA pulses for the same 1 ms shown in (b) and (d). The time interval between the NNBE(L) and the next pulse location is shown in black in the histogram.

Figure 4.3 shows one of the 18 NNBE(L)s; this NNBE(L) had the largest VHF power in the group of 18. Figure 4.3a shows 10 ms of data, including 5 ms before the initial event of the flash. Based on the $\int dE/dt$ locations (blue dots) of the IB pulses and the NNBE(L), the flash initiated at 6.3 km altitude and developed downward. The identification of the initial event as an NNBE(L) is based in part on its clear bipolar fast antenna pulse and the coincident Log-RF pulse that was larger than any of the Log-RF pulses associated with the IB pulses. Despite having the largest Log-RF pulse, the NNBE(L) did not have the largest magnitude FA pulse since Figure 4.3a shows that there were many classic IB pulses with larger magnitudes; the largest IB pulse magnitudes were about a factor of 5 larger than the NNBE(L). The NNBE(L) altitude of 6.3 km is typical for –CG flash initiation.

Figure 4.3b is an expanded view of the first 1 ms of electrical activity, including the NNBE(L) and first three classic IB pulses. It is easy to see that each classic IB pulse had a coincident, substantial Log-RF pulse and that before the first classic IB pulse there were several narrow IB pulses, including some with substantial Log-RF pulses, as found by Marshall et al. (2019). Note that the first two narrow IB pulses located after the NNBE(L) are not easily visible in the FA data shown in Figure 4.3b, but they were observed and located using $\int dE/dt$. Figure 4.3b also indicates that the NNBE(L) and the first classic IB pulse were close to each other in time ($\sim 390 \mu\text{s}$) and space ($\sim 80 \text{ m}$); we take these facts as additional indications that the NNBE(L) likely initiated this -CG flash.

In Figure 4.3c the NNBE(L) data are plotted on a $100 \mu\text{s}$ scale. The NNBE(L) had a range-normalized FA amplitude $E_{100\text{km}}$ of 1.16 V/m and a VHF power of 1290 W. (These values are a factor of ~ 15 and ~ 5 smaller, respectively, than found for the NNBE(T) in Figure 4.2). Note in Figure 4.3c that the NNBE(L) had a simple bipolar waveform (similar to the NNBE(T) in Figure 4.2), and that the risetime of the coincident Log-RF pulse was about $5 \mu\text{s}$ (slower than for the NNBE(T) in Figure 4.2).

Figure 4.3d shows the altitudes with error bars of the NNBE(L), of the classic IB pulses (including sub-pulses), and of many narrow IB pulses shown above in Figure 4.3b. Overall, Figure 4.3d shows that the trend of the IB pulses was to descend in altitude. However, in the first 500 μs after the NNBE(L), most of the IB pulses had altitudes between 6.2 and 6.4 km with overlapping error bars ($\Delta z \approx \pm 200$ m). On the other hand, the Δz error bars did not overlap for the 5.7 km altitude of the second classic IB pulse peak at 520 μs and the altitudes of the two small events at 6.3 km that occurred only 20 μs later (at 590 μs). Recall that 6.3 km was the approximate altitude of the NNBE(L).

The histogram in Figure 4.3e is for the distribution of times between each pair of successive pulses in Figure 4.3d. It is important to note that the 140 μs between the NNBE(L) and the next pulse (black marker in Figure 4.3e) was substantially longer than all of the other interpulse intervals. As discussed later, we find that this first pulse pair, i.e., the interval from the NNBE to the next pulse, typically has one of the longest time intervals in all the NNBE(L)s and NNBE(H)s cases.

To summarize, the NNBE(L) in Figure 4.3 apparently initiated the following -CG flash, since Figure 4.3a shows that there was no electrical activity for at least 5 ms before the NNBE(L), and Figure 4.3b shows that the first classic IB pulse occurred only 390 μs after the NNBE(L) and only 80 m horizontally from the NNBE(L). Furthermore, the Log-RF duration of this NNBE(L) was about 12 μs (Figure 4.3c), which was typical of the NBEs initiating flashes in Rison et al. (2016). We note that the separation distance of 80 m between NNBE(L) and the first classic IB pulse has an uncertainty of 170 m while their separation in time of 390 μs has an uncertainty < 1 μs .

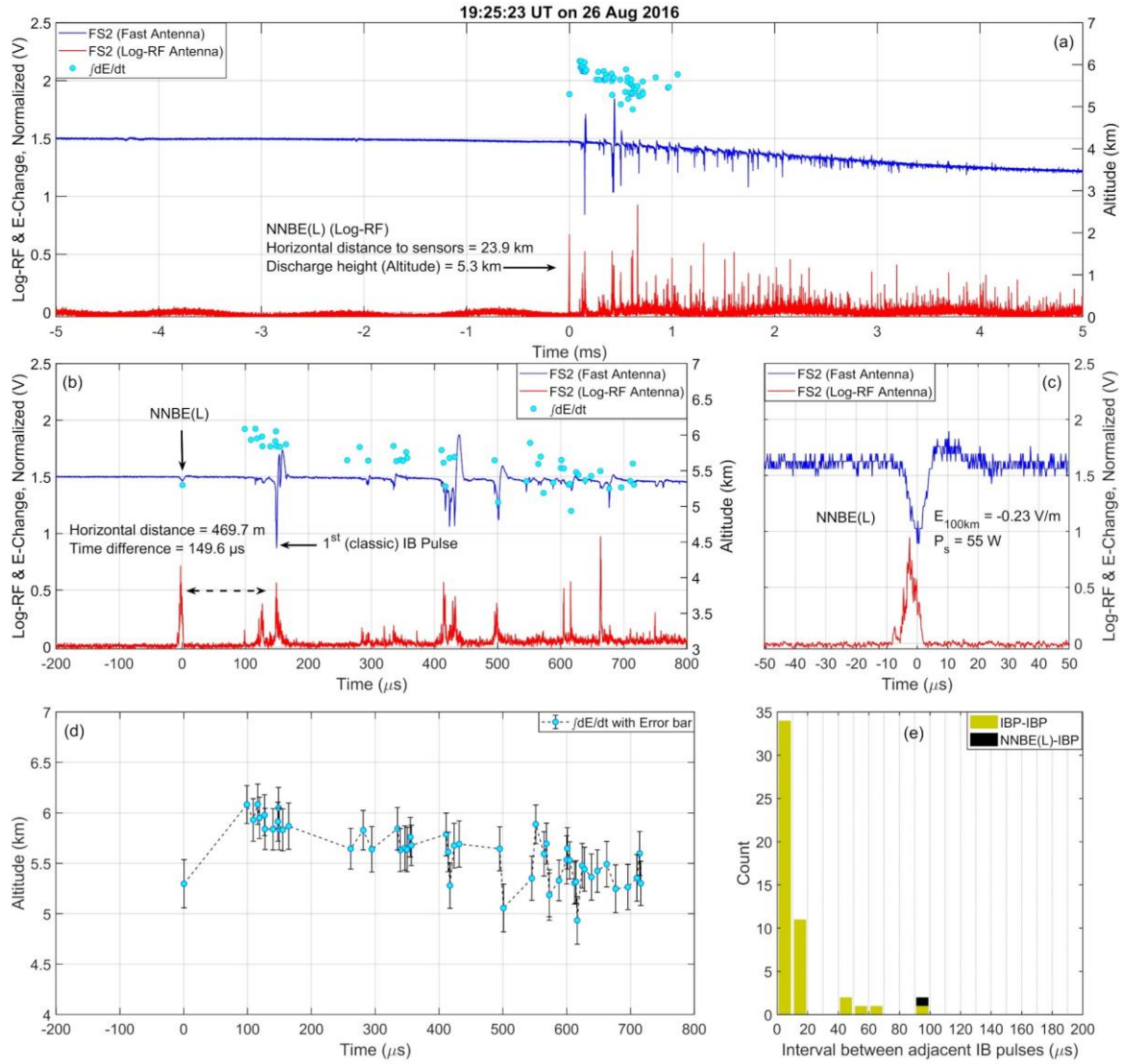


Figure 4.4. Similar to Figure 4.3, showing another example of an NNBE(L) that apparently initiated a -CG flash.

Figure 4.4 is similar to Figure 4.3 for another example of an NNBE(L) that apparently initiated a -CG flash. This NNBE(L) had $E_{100km} = -0.23$ V/m and a VHF power of 55 W. Note that the altitude of this NNBE(L) was lower than the following IB pulses with no overlap of altitude error bars (Figure 4.4d).

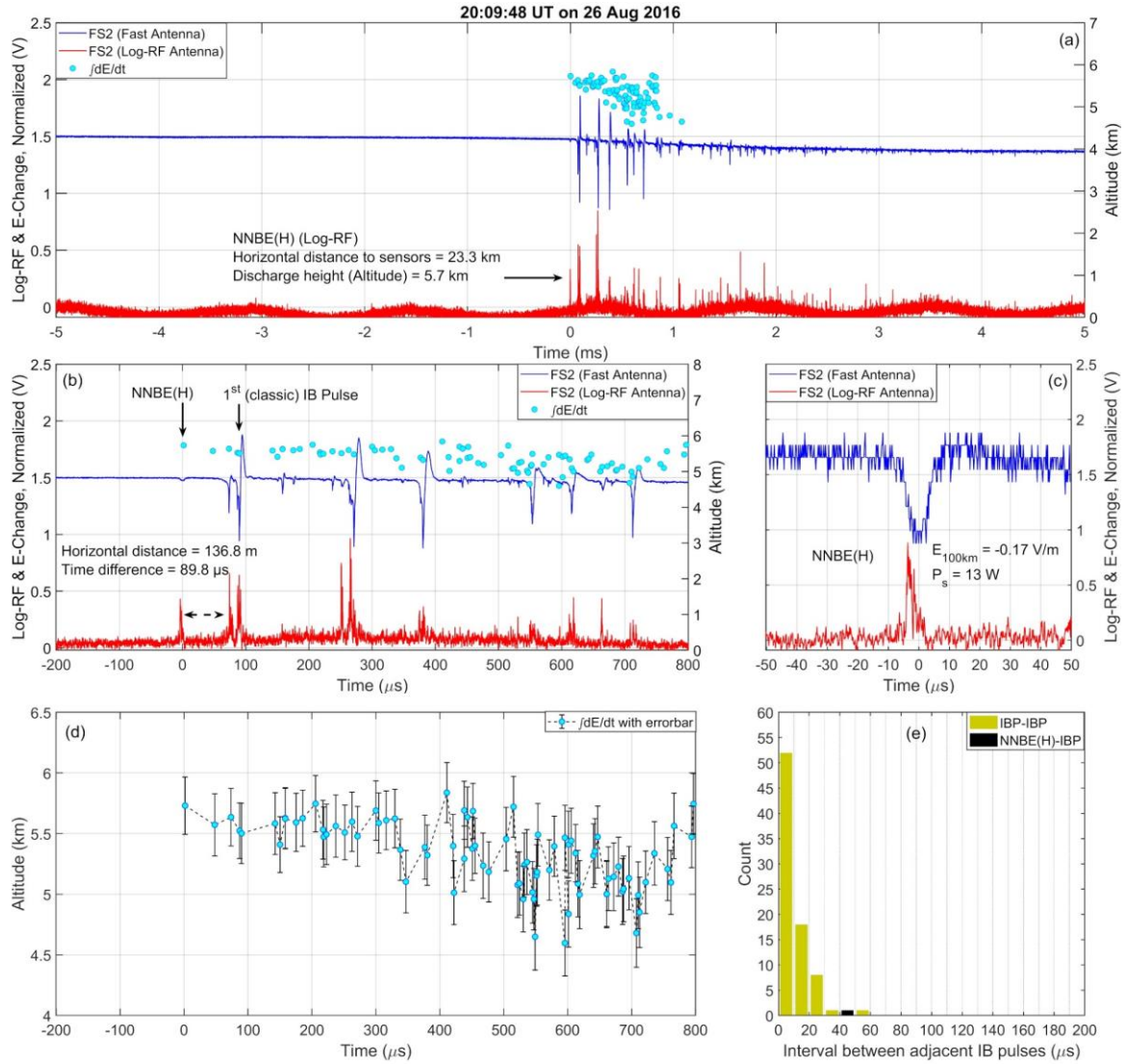


Figure 4.5. Similar to Figure 4.3, showing an example of an NNBE(H) that apparently initiated a -CG flash.

Figure 4.5 is similar to Figure 4.3 but, it shows characteristics for one of the largest of the 15 NNBE(H)s. This event has a hump-like fast antenna pulse (no clear overshoot) with E_{100km} of only -0.17 V/m and a relatively weak, coincident Log-RF pulse with a VHF power of only 12.9 W. Despite this low power, only a few of the IB pulses had larger Log-RF pulses than the NNBE(H) (Figures 4.5a and 4.5b) even though many of them had substantially larger E_{100km} amplitudes.

This NNBE(H) apparently initiated the following -CG flash, since (1) there was no electrical activity before the NNBE(H) (Figure 4.5a) and (2) the first classic IB pulse occurred about 90 μs after the NNBE(H) and only about 136 m horizontally from the NNBE(H) (Figure 4.5b) (with time and distance uncertainties of $< 1 \mu\text{s}$ and 610 m, respectively). Furthermore, the NNBE(H) FA waveform was similar to the two “more monopolar” negative NBEs shown in Rison et al. (2016) that initiated -CG flashes. As in Figure 4.3d, Figure 4.5d shows that the general trend of the IB pulses was to descend in altitude, that most of the IB pulse altitudes had overlapping error bars ($\Delta z \approx \pm 250 \text{ m}$), but that some of the higher and lower IB pulse altitudes were separated by more than 500 m. Figure 4.5e shows that the $\sim 50 \mu\text{s}$ between the NNBE(H) and the next pulse was longer than all but one of the other interpulse intervals.

Figure 4.6 is similar to Figure 4.5 and shows another example of an NNBE(H) that apparently initiated a -CG flash; this NNBE(H) had $E_{100\text{km}}$ of only -0.10 V/m and a VHF power of 4.0 W. Note that the altitude of this NNBE(H) was higher than the first IB pulse with no overlap of altitude error bars.

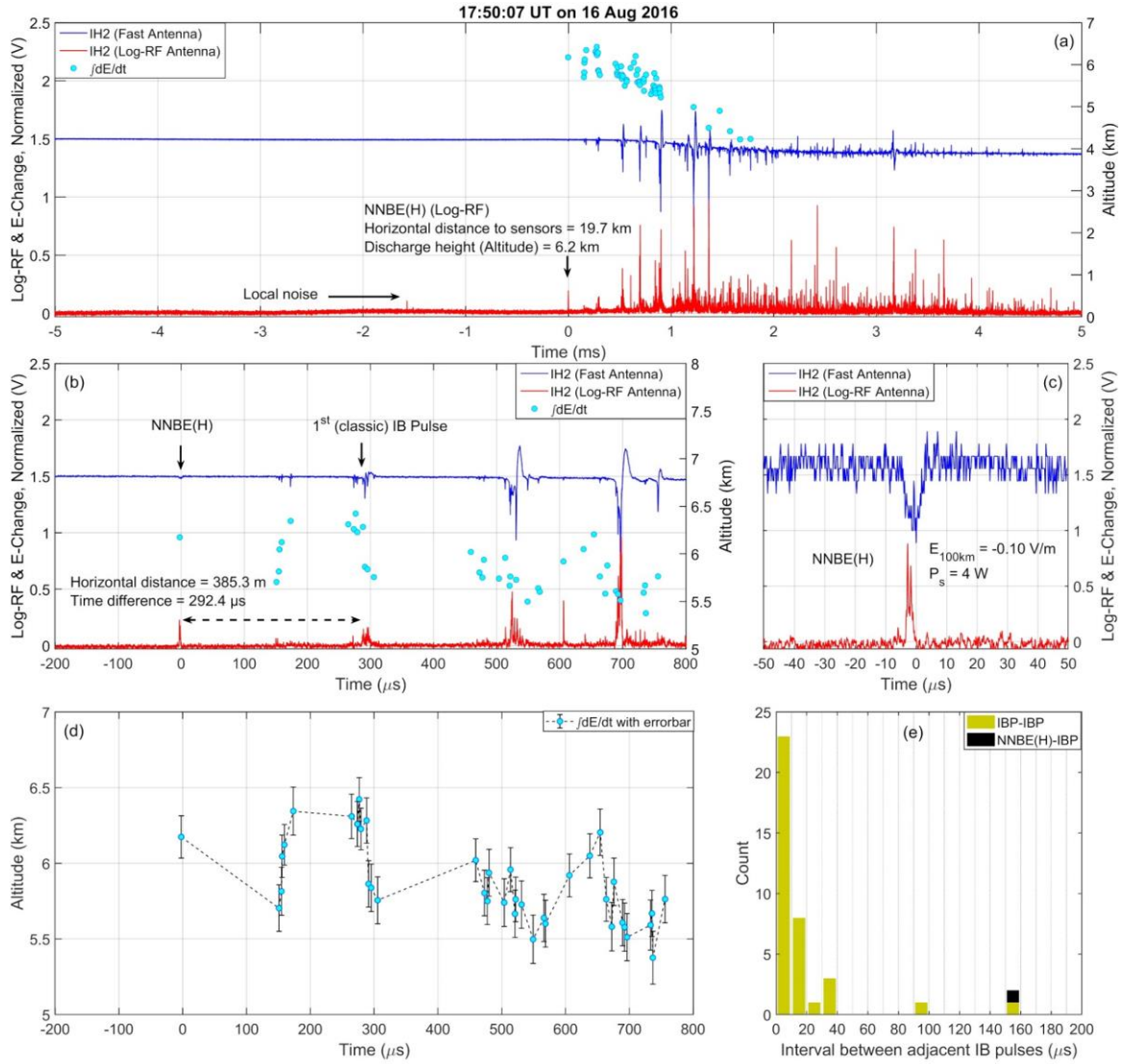


Figure 4.6. Similar to Figure 4.5, showing another example of an NNBE(H) that apparently initiated a -CG flash.

In summary, among the set of 868 -CG flashes, each of the 18 NNBE(L)s and 15 NNBE(H)s were identified as initiating -CG flashes because they satisfied the following criteria, as seen the examples in Figures 4.3, 4.4, 4.5, and 4.6:

- a) The NNBE was the first event of a -CG flash. In other words, the change from no electrical activity to electromagnetic pulses of the -CG flash began with the NNBE.

- b) The NNBE was close in time and space to the first classic IB pulse of the -CG flash. Although the flashes studied herein were too far from the FA sensors to detect an IEC, the NNBE probably started an IEC that led to the first classic IB pulse (e.g., Marshall et al., 2014; Chapman et al., 2017).
- c) The NNBE(L)s had a simple bipolar FA waveform and a Log-RF power that was larger than the power of all or almost all of the IB pulses.
- d) The NNBE(H)s had a small amplitude hump-like FA waveform and a Log-RF power that was quite large relative to the $E_{100\text{km}}$ amplitude of the FA hump.

Obviously, finding only 33 -CG flashes were initiated by NNBEs leaves 835 -CG flashes that must have initiated without an NNBE, similar to the only two -CG flashes investigated in Marshall et al. (2019).

4.3 Statistical results

In this section we report findings based on the dataset of 868 -CG flashes and on statistical analyses of the 24 NNBE(T)s, 18 NNBE(L)s, and 15 NNBE(H)s, described above, with Δx and $\Delta y < 2$ km and chi squared goodness-of-fit values < 5 .

4.3.1 Low percentage of -CG flashes preceded by an NNBE

As discussed in Section 4.2.4, visual inspection of the beginning of each flash in the group of 868 -CG flashes with detectable and locatable IB pulses determined that there were 33 NNBE(L)s and NNBE(H)s. Thus, we found that only 4% of the 868 -CG flashes were preceded by and probably were initiated by an NNBE. Based on this finding, it seems likely that most (i.e., about 96%) of the -CG flashes that occurred during our data collection were not initiated by an NNBE. This finding is similar to the finding of Lyu et al. (2019) that only about 10% on IC flashes were initiated by a positive NBE.

It is important to note that the Lyu et al. (2019) data were collected on flashes within 10 km of their interferometer, so there was no chance of missing the NBE signature. If the percentage of -CG flashes initiated by NNBEs is similar to the percentage of IC flashes initiated by positive NBEs found by Lyu et al. (2019), then it is likely that we detected a significant fraction of the NNBEs initiating -CG flashes in our group of 868 -CG flashes.

4.3.2 Altitudes of NNBEs

Figure 4.7a shows the altitude distribution of 24 NNBEs(T), 18 NNBEs(L), and 15 NNBE(H)s. The altitudes of the 24 NNBE(T)s ranged from 8.0-16.3 km with average of 12.2 km, while the 18 NNBE(L)s ranged from 5.0-7.5 km with average of 6.27 km, and 15 NNBE(H)s ranged from 4.6 – 7.8 km an average of 6.18 km.

In Figure 4.7a we also see that the NNBE(L)s and NNBE(H)s occurred in the same altitude range despite their different fast antenna waveforms. Rison et al. (2016) showed two events like our NNBE(H)s (their Figures 4.4c and 4.4d) that occurred at 6.0 km altitude and initiated -CG flashes. Rison et al. (2016) seemed to suggest that despite their “more monopolar” waveforms, these events were true negative NBEs, since they were caused by fast positive breakdown, just like the more powerful positive NBEs (with bipolar waveforms) that initiated the IC flashes in that study. Therefore, the fact that the NNBE(L)s and NNBE(H)s spanned similar altitudes in Figure 4.7a is consistent with the possibility that NNBE(H)s are merely low power variants of NNBE(L)s. The altitudes of 21 of the 24 NNBE(T)s in this study were below 15 km and thus lower than the majority of those found by Smith et al. [2004] and Wu et al. [2012]. The average altitude of our 24 NNBE(T)s is 5-6 km lower than averages reported in those two earlier studies. The NNBE(L)s and NNBE(H)s occurred at even lower altitudes than the NNBE(T)s in this study, which is not surprising since each of these NNBEs was the initial event of a -CG flash.

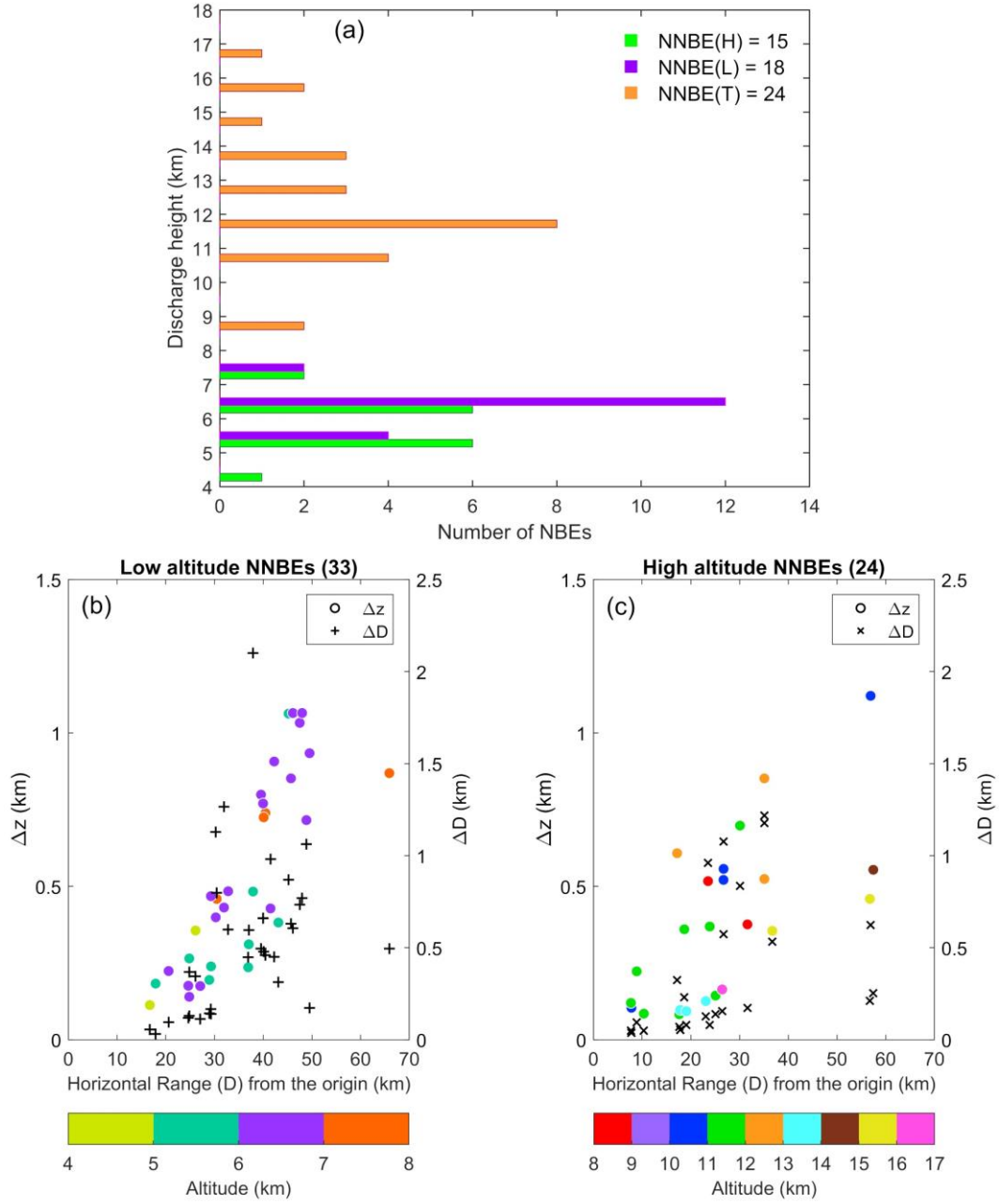


Figure 4.7. (a) Altitude histogram of the three types of NNBEs. (b) Horizontal distance error (ΔD) and altitude error (Δz) for NNBEs initiating CG flashes, namely NNBE(L)s and NNBE(H)s, versus NNBE horizontal range, D . Each NNBE has a colored circle for Δz and a “+” for ΔD . These NNBEs occur at altitudes below 8 km with altitudes indicated by the color bar. (c) Similar to (b), but for NNBE(T)s versus NNBE horizontal range. These NNBEs occur at altitudes above 8 km with altitudes indicated by the color bar.

Overall, Figure 4.7a shows that the NNBE(L)s and NNBE(H)s in this study had no altitude overlap with the vast majority of typical, high altitude NNBE(T)s found in this and in earlier studies.

Figure 4.7b shows the horizontal location errors, ΔD , and the altitude location errors, Δz , for the low altitude NNBEs (i.e., NNBE(L)s and NNBE(H)s); Figure 4.7c shows ΔD and Δz for the high altitude NNBE(T)s. All 57 of the selected NNBEs had $\Delta z < 1.2$ km and (with one exception) had $\Delta D < 1.4$ km. As expected for time-of-arrival locating techniques (e.g., the PBFA algorithm used herein), Figures 4.7b and 4.7c show that altitude errors increase with horizontal range to the flash but are generally smaller for higher altitude events (e.g., Karunarathne et al. 2013).

4.3.3 Durations of NNBEs

Figure 4.8a shows a histogram of the total pulse durations for the three types of NNBEs based on fast antenna data collected at distances > 20 km. For each NNBE type, the arithmetic mean with its standard deviation and geometric mean with its standard deviation are given. The arithmetic mean durations for NNBE(H), NNBE(L), and NNBE(T) were 13, 25, and 20 μs , respectively. The NNBE(L) and NNBE(T) durations are in reasonable agreement with an arithmetic mean of 25 μs reported by Ahmad et al. [2010] for 75 negative narrow bipolar pulses. The approximately 50% shorter pulse durations for NNBE(H) may be due to their lack of an overshoot pulse. Thus, these duration data are consistent with the notion that NNBE(H)s are weak variants of NNBE(L)s in which the overshoot pulse is so weak it is lost in the noise. An alternate explanation is that NNBE(H)s develop via a different mechanism from NNBE(L)s that does not produce any overshoot pulse.

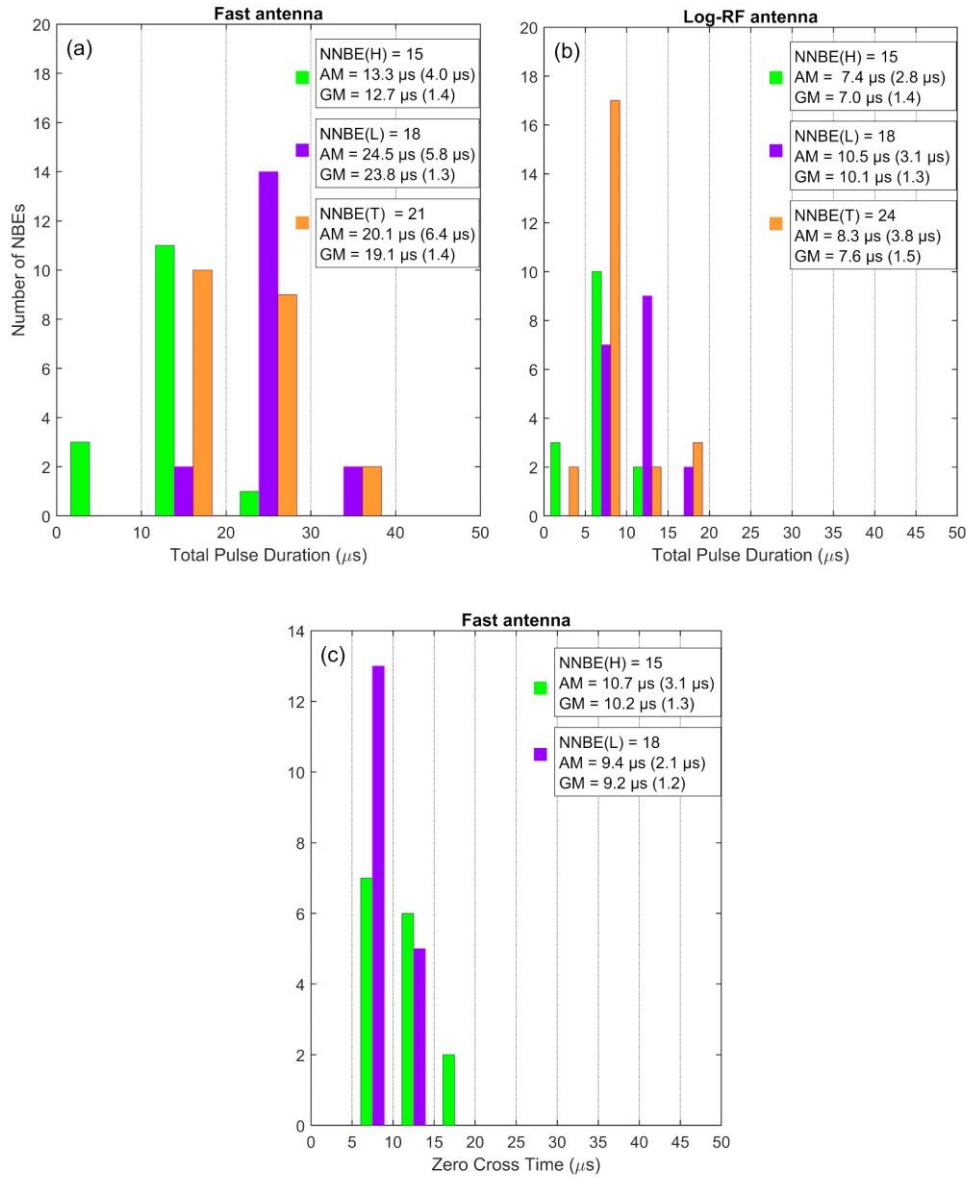


Figure 4.8. (a) Durations for the three NNBE types, based on FA data at distances > 20 km. (b) Durations for the three NNBE types, based on Log-RF data. (c) Zero cross time based on FA data for NNBE(L)s and NNBE(H)s; equivalent to the durations of the leading pulse of the NNBE(L) bipolar pulses and the durations of the hump in NNBE(H) pulses. The legend of each plot includes the arithmetic mean (AM) with the standard deviation in parentheses plus the geometric mean (GM) with its standard deviation in parentheses. The grid lines in each figure show the bin edges.

Figure 4.8b is a histogram of the duration of the main peak of the Log-RF waveform associated with NNBEs. Relevant Log-RF data were obtained by averaging measurements from at least 4 sensor sites. The arithmetic mean durations for NNBE(H), NNBE(L), and NNBE(T) were 7, 11, and 8 μs , respectively.

The NNBE(H) average duration of 7 μs was shorter than the durations of 10 and 14 μs for two NNBE(H)s reported by Rison et al. (2016). Overall, the durations of the Log-RF pulses were about half the durations of the coincident fast antenna NNBE pulses (Figure 4.8a). For most NNBEs, the main Log-RF pulse occurred during the initial half cycle of the bipolar fast antenna pulse or during the fast antenna hump in the NNBE(H)s, which fits with the Log-RF pulse durations being about half of the fast antenna pulse durations.

Figure 4.8c is a histogram for the “zero cross time” of NNBE(L)s and NNBE(H)s, by which we mean the durations of the initial half cycle of the FA bipolar waveform for NNBE(L)s (e.g., Willett et al., 1989) and the durations of the hump for NNBE(H)s. The similar zero cross times for NNBE(L)s and NNBE(H)s seen in Figure 4.8c are consistent with the idea that NNBE(H)s may be weak variants of NNBE(L)s. However, if the NNBE(H)s are produced by a different mechanism from the NNBE(L)s that does not produce an overshoot peak, then the “zero cross times” defined for NNBE(H)s would be meaningless in comparison to a bipolar waveform.

4.3.4 Range-normalized amplitudes of NNBEs

Figure 4.9a presents a histogram of range-normalized electric field changes, $E_{100\text{km}}$, of 15 NNBE(H)s, 18 NNBE(L)s, and 22 NNBE(T)s; the histogram spans $E_{100\text{km}}$ values from 0 to 20 V/m.

Figure 4.9b is an expanded histogram showing only those $E_{100\text{km}}$ values that are less than 4 V/m, which includes all of the NNBE(H)s and NNBE(L)s and 16 NNBE(T)s. In order to avoid electrostatic effects, only NNBEs that occurred at horizontal ranges > 20 km from the EE sensor were included in this analysis. $E_{100\text{km}}$ for 15 NNBE(H)s ranged from 0.06 to 0.54 Vm^{-1} with an arithmetic mean of $(0.19 \pm 0.13) \text{Vm}^{-1}$. $E_{100\text{km}}$ for 18 NNBE(L)s varied from 0.15 to 1.53 Vm^{-1} with an arithmetic mean of $(0.60 \pm 0.39) \text{Vm}^{-1}$.

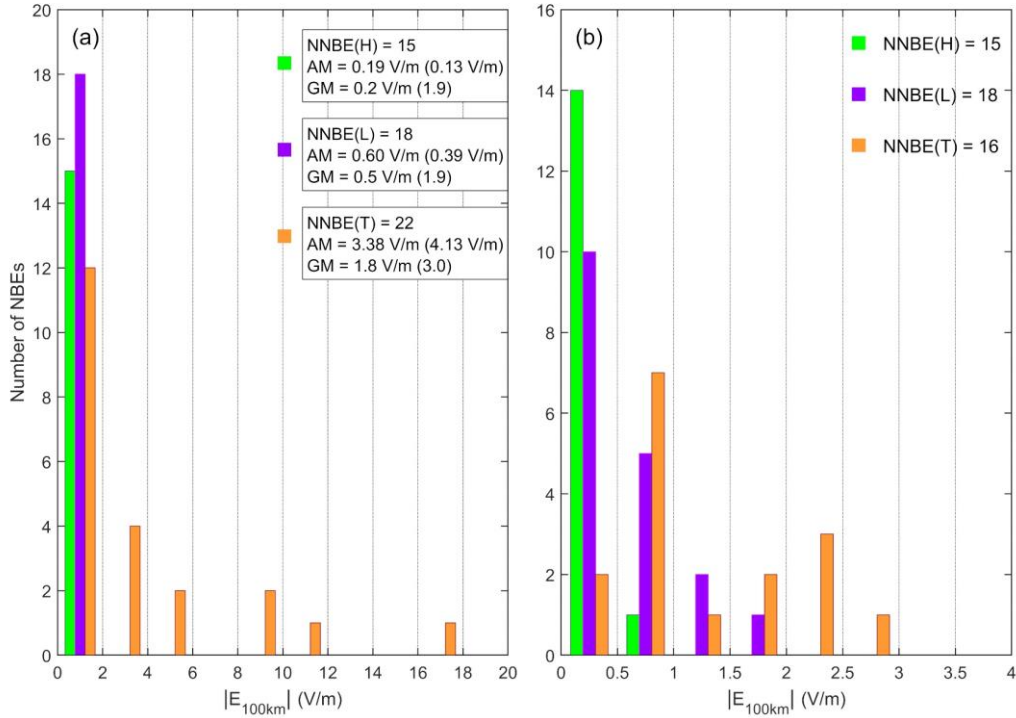


Figure 4.9. (a) Histogram of NNBE zero-to-peak FA magnitudes range-normalized to 100 km (E_{100km}) for the three NNBE groups. The legend includes the arithmetic mean (AM) with the standard deviation in parentheses plus the geometric mean (GM) with its standard deviation in parentheses. The vertical grid lines show the bin edges. (b) Expanded view of data from 0-4 V/m.

E_{100km} for 22 NNBE(T)s varied from 0.41 to 16.21 Vm^{-1} with an arithmetic mean (3.38 ± 4.13) Vm^{-1} . The arithmetic mean of E_{100km} values of NNBE(T)s in this study were much smaller than the corresponding NNBE arithmetic mean of (17.6 ± 7.1) Vm^{-1} reported by Ahmad et al. [2010] for thunderstorms in Malaysia. Overall, the E_{100km} values of NNBEs found herein indicate that the NNBE(L)s were significantly larger than the NNBE(H)s, but both of these low-altitude NNBE types had substantially smaller E_{100km} values than most NNBE(T)s.

The data in Figure 4.9 also are consistent with the idea that NNBE(H)s are weaker, lower power variants of NNBE(L)s despite their different fast antenna waveforms. Since Figure 4.9 shows that NNBE(H) fast antenna waveforms have smaller E_{100km} values than NNBE(L)s, the NNBE(H)s may “lack” the overshoot because it is lost in the fast antenna noise.

One fact supporting this explanation is that the ratio of the NBE bipolar initial half cycle to its overshoot is generally relatively large, varying from about 3 to 9 (e.g., Willett et al., 1989; Ahmad et al., 2010). The combination of this typical ratio with a weak initial half cycle of an NNBE(H) could make any NNBE(H) overshoot difficult to detect, even if the physical mechanism that produces the NNBE(H)s and NNBE(L)s is the same.

4.3.5 VHF power of NNBEs

Figure 4.10 shows distributions of radiated peak source power for NNBE(H)s, NNBE(L)s, and NNBE(T)s, estimated according to Equation 4.1 using Log-RF data collected in the 186-192 MHz band. The Log-RF powers of the 15 NNBE(H)s ranged from 1 – 23 W with an arithmetic mean of 7.6 W (or 8.8 dBW). The Log-RF powers of the 18 NNBE(L)s ranged from 9 – 1290 W with an arithmetic mean of 232 W (or 23.7 dBW). The Log-RF powers of the 24 NNBE(T)s ranged from 260 – 7420 W with an arithmetic mean of 1770 W (or 32.5 dBW). Thus, the NNBE(H)s had the weakest VHF powers, the NNBE(L)s were more powerful, and the NNBE(T)s were substantially more powerful. For comparison Rison et al. (2016) showed two NNBEs that initiated -CG flashes; their VHF powers were 9.0 and 25.8 dBW and were detected in the 60-66 MHz band.

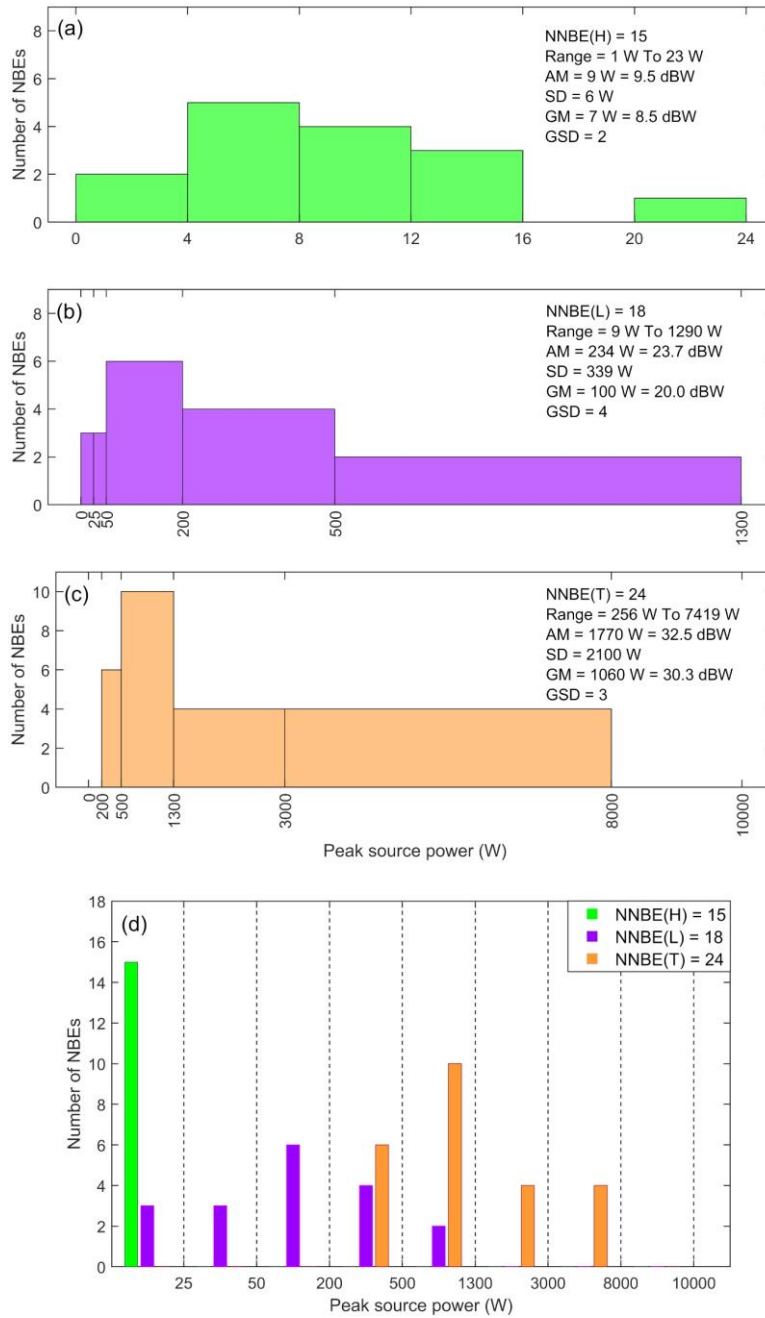


Figure 4.10. Histograms of VHF powers of the three NNBE types. Note the different bin sizes in each histogram. (a) NNBE(H)s. (b) NNBE(L)s. (c) NNBE(T)s. (d) Comparison histogram showing all three types of NNBEs; bin edges are shown by the vertical dashed lines. AM = arithmetic mean, SD = standard deviation of AM, GM = geometric mean, GSD = standard deviation of GM.

4.3.6 Distance and time separations between NNBEs and the first classic IB pulse

We analyzed the 15 NNBE(H)s and 18 NNBE(L)s that initiated -CG flashes to find the time separation and the horizontal distance separation between each of the NNBEs and the first classic IB pulse (or 1stCIBP) of the -CG flash. Note that this time separation is, by definition, the duration of the IEC that occurs at the beginning of most or all flashes (Marshall et al., 2014; Chapman et al., 2017).

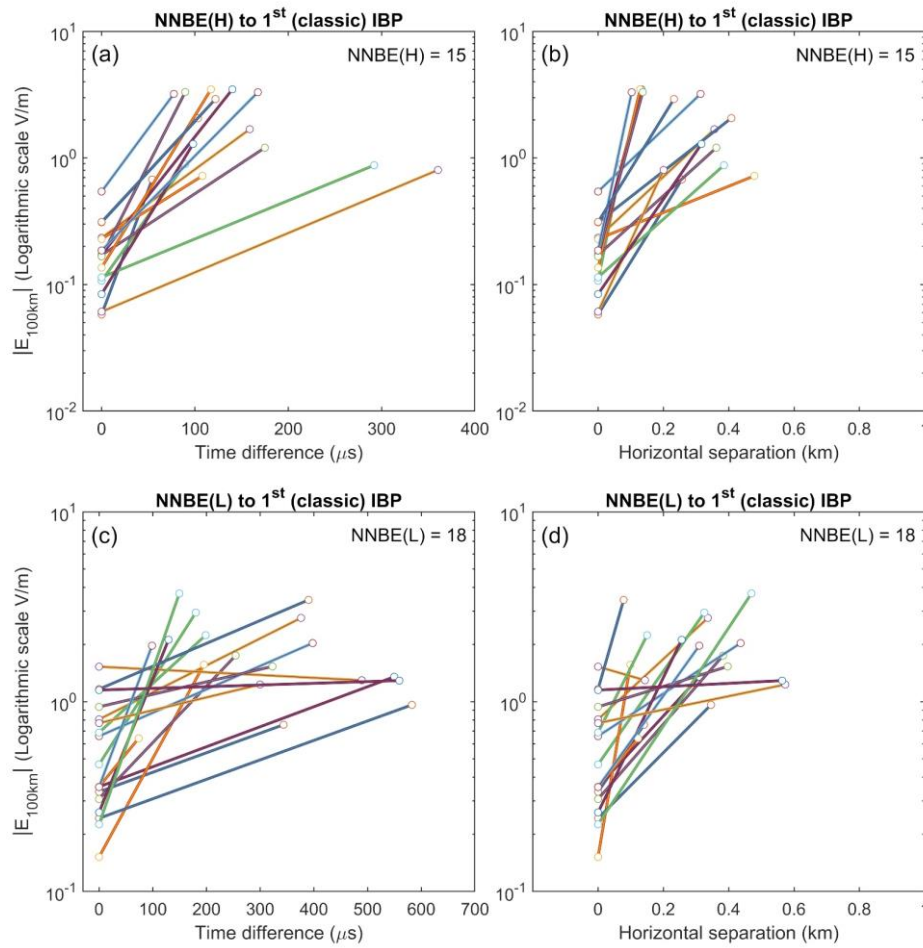


Figure 4.11. Distance and time separations between NNBEs and the first classic IB pulse with (a) and (b) showing values for 15 NNBE(H)s and with (c) and (d) showing values for 18 NNBE(L)s. In each frame the NNBE is plotted at zero on the horizontal axis (time difference or horizontal distance difference) and plotted on the vertical axis with the NNBE's range-normalized peak amplitude ($E_{100\text{km}}$). In each frame the 1st IBP of the CG flash initiated by the NNBE is plotted in the horizontal with the time of occurrence after the NNBE or horizontal distance from the NNBE and plotted on the vertical axis with the 1st IBP's $E_{100\text{km}}$ amplitude.

For 15 NNBE(H)s Figure 4.11a shows the time separation in μs (horizontal axis) for each NNBE(H)/1stCIBP pair plotted as a line connecting the NNBE(H) at 0 μs and the 1stCIBP at the time it occurred after the NNBE(H). The vertical axis in Figure 4.11a shows the range-normalized $E_{100\text{km}}$ amplitudes of the NNBE(H) and the 1stCIBP, so each NNBE(H) or 1stCIBP is plotted as a (time, $E_{100\text{km}}$) point. The time separations of NNBE(H)/1stCIBP pairs varied from 27 to 368 μs , with an average value of 136 μs and an uncertainty $< 1\mu\text{s}$. It can be seen from the Figure 4.11a that most of the 1stCIBPs occurred less than 200 μs after their corresponding NNBE(H)s. These time separations are in good agreement with the durations of IECs at the beginning of -CG flashes in Florida thunderstorms, which had average durations of 180 μs and 230 μs (Marshall et al., 2014; Chapman et al., 2017, respectively). Figure 4.11b is similar to Figure 4.11a, but shows that the horizontal distance separation of NNBE(H)/1stCIBP pairs varied from 70 to 500 m with an average of 300 m. Note however, that the separation uncertainty was usually 100 – 300 m with a maximum of ~ 600 m. The short time separations and close distance separations support the hypothesis that the NNBE(H)s initiated these 15 - CG flashes. Note also in Figures 4.11a and 11b that the $E_{100\text{km}}$ amplitudes of all NNBE(H)s are smaller than the $E_{100\text{km}}$ amplitudes of the 1stCIBPs, which emphasizes how small the NNBE(H) $E_{100\text{km}}$ amplitudes are in these data.

Figures 4.11c and 11d are similar in layout to Figures 4.11a and 11b, but are instead for 18 NNBE(L)/1stCIBP pairs. It is immediately obvious (because of the negative slope of some connecting lines) that some NNBE(L)s had larger $E_{100\text{km}}$ amplitudes than the corresponding 1stCIBP. In Figure 4.11c the separation time of NNBE(L)/1stCIBP pairs was on average longer than for NNBE(H)/1stCIBP pairs with the separation times ranging from 74 to 583 μs with an average of 311 μs , which is somewhat larger than the IEC average duration of 230 μs in Chapman et al. (2017).

The time uncertainty is again $< 1 \mu\text{s}$. Figure 4.11d shows horizontal distance separation of NNBE(L)/1stCIBP pairs varied from 60 to 600 m with an average value of 300 m, which was equal to the average separation distance of NNBE(H)/1stCIBP pairs. Overall, the relatively short time separations and relatively close distance separations support the hypothesis that the NNBE(L)s initiated these 18 -CG flashes.

4.3.7 Successive time separations between FA pulses

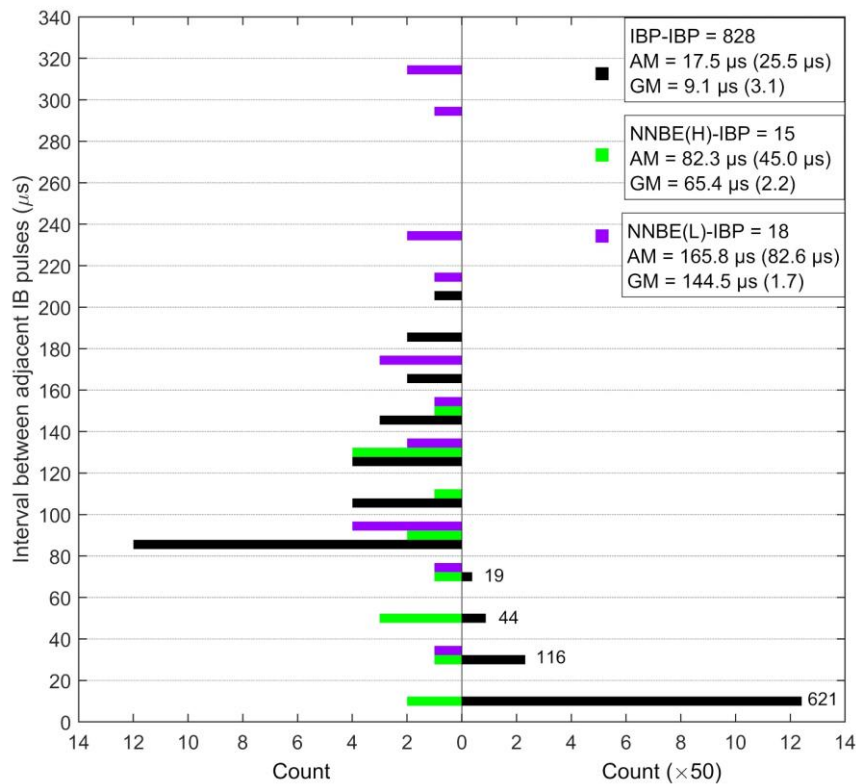


Figure 4.12. Histogram of time separations between successive pulses; examples of these separations are shown in Figures 4.3d, 4.3e and 4.4d, 4.4e. Three groups of time separations are shown: (i) for 15 flashes, the time separation between the initiating NNBE(H) and the following IBP (marked in green), (ii) for 18 flashes, the time separation between the initiating NNBE(L) and the following IBP (marked in purple), and (iii) 828 IBP-IBP time separations that occurred after the NNBE-IBP pair during first millisecond of 10 NNBE(H)s and 10 NNBE(L)s (marked in black). Bin edges are shown by the horizontal lines; the legend for each group includes its arithmetic mean (AM) with the standard deviation in parentheses plus its geometric mean (GM) with standard deviation in parentheses.

In Figures 4.3e, 4.4e, 4.5e, and 4.6e we showed that the time separation between the NNBE and the following narrow IBP (the NNBE-IBP pair) was usually longer than the time separations between the following successive IBP-IBP pairs. In Figure 4.12 we investigate this tendency. Figure 4.12 shows histograms of time separations for three groups: (1) the 15 NNBE(H)-IBP pairs, (2) the 18 NNBE(L)-IBP pairs, and (3) 828 IBP-IBP pairs from 10 of the NNBE(H) flashes and 14 of the NNBE(L) flashes. The third group of pairs is taken from the first 800 μs from each flash, as shown for example in Figures 4.3d and 4.3e, which has 45 IBP-IBP pairs. On average for 24 -CG flashes, there were 37 IBP-IBP pairs in the first 800 μs .

Figure 4.12 shows that 621 of 828 or 75% of the IBP-IBP pairs had time separations less than 20 μs . The arithmetic mean (AM) separation of the 828 IBP-IBP pairs was 17.5 μs with the largest separation being < 220 μs . The time separation of the 15 NNBE(H)-IBP pairs averaged 82.3 μs , while the time separation of the 18 NNBE(L)-IBP pairs averaged 165.8 μs . Both NNBE-IBP average times were significantly longer than the IBP-IBP times. Thus, the interval after the NNBE is different than the interpulse intervals during the IB stage.

4.3.8 Altitude separations between NNBE-IBP

In Rison et al. (2016), the positive NBEs that initiated IC flashes had fast positive breakdown moving downward followed by negative discharges moving upward. We examined our dataset for the opposite directional development in the -CG flashes initiated by NNBEs.

It was found that after the NNBEs the general trend of the IB pulses was to move negative charge downward (see Figures 4.3a, 4.4a, 4.5a, and 4.6a). However, because of the relatively large altitude errors for our NNBEs and IB pulses, what is less certain is the position of the NNBE relative to the following IB pulse. For example, Figure 4.3d shows that the NNBE(L) altitude, including its uncertainty, was about the same as the altitude of the IB pulse that immediately followed the NNBE(L); however, even considering their altitude error bars,

Figure 4.4d showed that the NNBE(L) altitude was below the following IB pulse. Similarly, in Figure 4.5d the NNBE(H) altitude was about the same as the following IB pulse but the NNBE(H) in Figure 4.6d was clearly above than the following IB pulse.

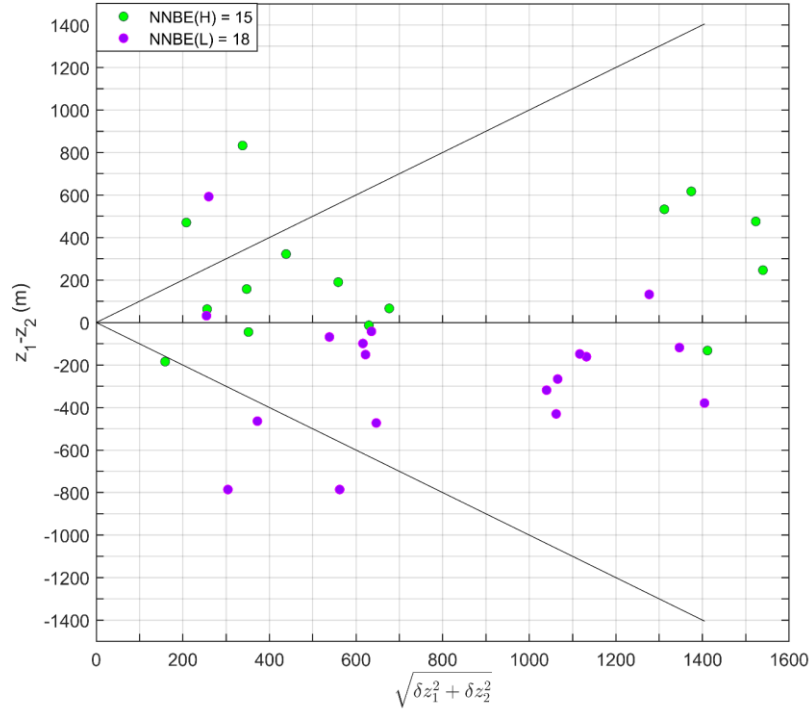


Figure 4.13. Altitude difference ($z_1 - z_2$) between the initiating NNBE and the first IB pulse in the flash, plotted as a function of the estimated error in the altitude difference. Solid diagonals are unity ratios. Points above (below) zero are events for which the NNBE is higher (lower) than the first IB pulse. The three NNBE-first IB pairs above the upper diagonal and the four NNBE-first IB below the lower diagonal had altitude differences ($z_1 - z_2$) greater in magnitude than the estimated combined altitude error.

Figure 4.13 shows, for the 15 NNBE(H)s and 18 NNBE(L)s, the altitude difference ($z_1 - z_2$), where z_1 is the NNBE altitude and z_2 is the first IB pulse altitude, versus the uncertainty in this difference. Positive values of ($z_1 - z_2$) indicate the NNBE was above the first IB pulse, as expected for -CG flash initiations based on Rison et al. (2016). At first glance, there is an intriguing tendency for the NNBE(L)s to be lower than the first IB pulse and the NNBE(H)s to be higher than the first IB pulse.

However, the diagonal lines show where the difference ($z_1 - z_2$) is equal to the uncertainty in the difference. Based on these “unity” lines, 26 of the 33 NNBEs were close enough to the IB pulse altitude such that their relative altitude is uncertain. Of the remaining 7 NNBEs, three were above the first IB pulse and four were below the first IB pulse, with a mixture of NNBE types (L and H) in both groups. In our opinion, no solid conclusion about the relative altitudes of NNBEs and the first IB pulse can be drawn from these data.

We hope to study this question further in the future with -CG flashes that are closer to our sensors for which the uncertainties in altitude are smaller. We are surprised that in Figure 4.13 the NNBE(H)s tend to have higher altitudes than the first IB pulse that follows them, and that the NNBE(L)s have the opposite tendency relative to the first IB pulse that follows them. We have no explanation of this apparent difference in tendency. The planned future work will also provide a test of this preliminary observation.

4.4 Discussion

NBEs are supposed to be very strong VHF radiators (e.g., Le Vine, 1980); Rison et al. (2016) reported positive NBEs with powers as large as 274,000 W and 5 NNBEs with powers in the range of 8-380 W. NBEs are also supposed to have large $E_{100\text{km}}$ values: Willett et al. (1989) reported the arithmetic mean (AM) for 18 positive NBEs was 8.0 V/m; Karunarathne et al. (2015) reported AM=11.0 V/m for 226 positive NBEs; Ahmad et al. (2010) reported AM=22.7 V/m for 107 positive NBEs and AM=17.6 V/m for 75 NNBEs. (Note that the altitudes of the NBEs in Willett et al. and in Ahmad et al. were not determined.) It has also been assumed that the charge motion of NBEs is vertically oriented, and in a study of 10 positive NBEs Karunarathne et al. (2016) showed that 7 were essentially vertical and 3 were oriented at $10^\circ - 20^\circ$ from vertical.

In contrast to expectations, Figure 4.10 shows that our NNBE(H)s and NNBE(L)s had AM powers of 9 W and 230 W, respectively, and Figure 4.9 shows that the $E_{100\text{km}}$ values of our NNBE(H)s and NNBE(L)s had AM values of 0.19 V/m and 0.60 V/m, respectively. We have suggested above that the NNBE(H)s might be weak variants of the NNBE(L)s based on their similar characteristics. We further speculate that NNBE(H)s and NNBE(L)s might propagate with a substantial horizontal component in addition to a vertical component. If this speculation is correct, then the weak VHF powers might be primarily due to θ approaching $\pi/2$ radians in Equation 4.2 (rather than $\theta = 0$ radians, as assumed).

A mainly horizontal orientation could also account for the relatively small $E_{100\text{km}}$ values of NNBE(H)s and NNBE(L)s. Some support for this hypothesis is found in Figure 4d of Rison et al. (2016), which shows mainly horizontal fast positive breakdown for an NNBE(H) with an estimated source power of only 8 W. Determination of the current propagation angle can best be accomplished with close examples of NNBEs, thus we will explore the possibility of non-vertical orientations in future work.

4.5 Summary and Conclusions

This study examines negative narrow bipolar events, or NNBEs, that occurred in July and August of 2016 in Mississippi thunderstorms. Our main focus has been on NNBEs that initiated some -CG flashes, called NNBE(L)s and NNBE(H)s herein. For comparison we also examine typical, high altitude NNBEs, herein called NNBE(T)s, found in the same dataset. Previous studies have recorded thousands of NNBE(T)s (e.g., Smith et al., 2004; Wu et al., 2011; Wu et al., 2012), while only 5 NNBE(H)s (Rison et al., 2016) and zero NNBE(L)s have been previously reported. We identified and located 15 NNBE(H)s, 18 NNBE(L)s, and 24 NNBE(T)s that satisfied all our location criteria, namely, Δx and Δy horizontal location uncertainties were < 2 km, and the chi-squared goodness-of-fit was < 5 . The determination that NNBE(L)s and NNBE(H)s initiated some -CG flashes was based mainly on three facts:

1. In both the fast antenna data and the Log-RF data, the change from no electrical activity to electromagnetic pulses of each -CG flash began when either an NNBE(L) or an NNBE(H) occurred (e.g., Figures 4.3a, 4.4a, 4.5a, and 4.6a). Thus, as the first detectable event, the NNBE(L) or NNBE(H) is apparently the impulsive initiating event of the -CG flash as described by Marshall et al. (2014).

2. After an NNBE(L) or an NNBE(H), the first classic IB pulse (1stCIBP) in the fast antenna data of each -CG flash occurred close in time (averages of 311 and 136 μ s, respectively) to the NNBE(L) or NNBE(H) (e.g., Figures 4.3b, 4.4b, 4.5b, 4.6b, 4.11a, and 11c). This time interval should be the time of the Initial E-Change or IEC defined by Marshall et al. (2014) and is the second stage in the lightning initiation process outlined by Marshall et al. (2014). Note that the measured NNBE(L)/1stCIBP times and NNBE(H)/1stCIBP times were similar to the IEC durations of -CG flashes (Marshall et al., 2014; Chapman et al., 2017), which also is consistent with the identification of NNBE(L)s and NNBE(H)s as initiating events.
3. After an NNBE(L) or an NNBE(H), the first classic IB pulse in the fast antenna data of each -CG flash occurred close in space (300 m on average) to the NNBE(L) or NNBE(H) (e.g., Figures 4.3b, 4.4b, 4.5b, 4.6b, 4.11b, and 4.11d). Since the first classic IB pulse is the third stage in the lightning initiation process as outlined by Marshall et al. (2014), one would also expect the first classic IB pulse to be spatially near the initiating event.

For all three types of NNBEs we have provided example plots showing, apparently for the first time, NNBE fast antenna data and coincident data of NNBE VHF power (Figures 4.2-4.6). For each of the three NNBE groups we have presented the following NNBE properties: altitudes (Figure 4.7), fast antenna pulse durations and VHF power pulse durations (Figure 4.8), range-normalized fast antenna amplitudes (Figure 4.9), VHF source powers (Figure 4.10), and for NNBE(L)s and NNBE(H)s, separation times and distances between each NNBE and the first classic IB pulse following it (Figure 4.11).

We also found that the interval between the NNBE(L)s and NNBE(H)s and the first IB pulse (usually a small amplitude, short duration IBP) was characteristically longer than the interpulse intervals during the early part of the IB stage of flash initiation (Figure 4.12). NNBE(H)s and NNBE(L)s occurred at low altitudes, 4.6 to 7.8 km, in keeping with typical initiation altitudes of –CG flashes in mid-latitude storms (e.g., Karunarathna et al., 2017). The NNBE(H)s are single hump events rather than bipolar events; those in our dataset are like the NNBEs discovered and labeled as “more monopolar” by Rison et al. (2016). The NNBE(L)s are low altitude NNBEs that are weaker in power than most NNBE(T)s but have the usual fast antenna bipolar waveform of typical NBEs. NNBE(H)s may simply be weaker versions of NNBE(L)s in which the overshoot peak of the bipolar event is difficult to see, as discussed above and supported by several aspects of the data herein.

We speculate that the charge motion of NNBE(L)s and NNBE(H)s may have had a more horizontal orientation than the primarily vertical orientation typically found for positive NBEs. This speculation is worthy of examination in future work. Perhaps related but also needing future study is the intriguing indication in Figure 4.13 that most NNBE(H)s may occur above the following IBPs while most NNBE(L)s may occur below them.

Our main conclusions from this study are as follows:

1. As discussed above, the data presented herein indicate that some negative CG flashes are initiated by NNBE(L)s and NNBE(H)s.
2. Visual inspection of the fast antenna and Log-RF data of 868 -CG flashes with locatable IB pulses showed that only 33 flashes (4%) were preceded by an event that can be characterized as an NNBE. Thus, 96% of the -CG flashes investigated probably did not begin with an NNBE. This finding agrees with the report of Lyu et al. (2019) that 88 % of IC flashes were not initiated by fast positive breakdown of a positive NBE. These findings are in contrast to the statement by Rison et al. (2016) “that all in-cloud lightning discharges are initiated by NBE-type fast positive breakdown.”
3. The NNBEs that initiated -CG flashes, namely NNBE(L)s and NNBE(H)s, were substantially weaker than NNBE(T)s (found herein) that did not initiate lightning flashes. They are also much weaker than previously studied positive NBEs that initiated IC flashes. VHF powers ranged from 1 – 23 W for NNBE(H)s and from 9 – 1290 W for NNBE(L)s versus 260 – 7420 W for NNBE(T)s (see Figure 4.10) and 93,000 – 274,000 W for three positive NBEs initiating IC flashes (Rison et al., 2016). Marshall et al. (2019) suggested that -CG flashes are easier to initiate than IC flashes since the IEC charge moments of -CG flashes are much smaller than the charge moments of IC flashes; similarly the much smaller powers of NNBEs initiating -CG flashes versus the positive NBEs initiating IC flashes support the hypothesis that -CG flashes preceded by NNBEs are easier to initiate than IC flashes preceded by positive NBEs.

CHAPTER 5

CHARACTERISTIC OF VHF PEAK POWER ASSOCIATED WITH POSITIVE NARROW BIPOLAR LIGHTNING PULSES

In this chapter, the primary focus is VHF radiation of narrow positive bipolar events (NBEs) and their involvement for initiation of the intracloud lightning flash. The chapter will expand the Wu et al. [2014] study by covering the VHF source powers of the initiating type positive NBE and the types of NBE defined by Karunarathne et al. [2015].

5.1 Introduction

Observation and measurement based on high frequency or HF (3-30 MHz) and very high frequency or VHF (30 – 300 MHz) emissions from lightning discharges have grown extensively, because these frequencies offer a unique perspective on lightning events [e.g., Le Vine and Krider, 1977; Taylor, 1978; Krider et al., 1979; Shao and Krehbiel, 1996]. The strongest VHF emission produced by lightning flashes is a specific class of intracloud lightning discharge first reported by Le Vine [1980], who found that the E-change waveform of the lightning discharge had a short duration (10-20 μ s) and a bipolar shape. Willett et al. [1989] found that the E-change waveform of these unique discharges had two initial polarities (positive and negative) and called them "Narrow Positive Bipolar Pulse (NPBP)" and "Narrow Negative Bipolar Pulse (NPBP)" according to their polarity.

Narrow bipolar pulses (NBPs) are also known as compact cloud discharges (CID) or narrow bipolar events (NBEs) in many investigations.

Based on a three-dimensional lightning mapping array called LMA (that uses VHF receivers in the 60-66 MHz band), Thomas et al. [2001] reported that positive NBEs could have a peak source power more than 300 kW (55 dBW). For comparison, Thomas et al. [2001] showed that non-NBE pulses in typical IC flashes had source powers of 10-100 W, while non-NBE pulses in CG flashes has source powers < 500 W. Zhang et al. (2010) reported that, according to the observation of the 3D VHF mapping array (bandwidth 267 - 273 MHz), the NBEs that initiates the IC flash show a radiated power of an excess of 16 kW. This value is much larger than that their reported emitted power value of 0.1-500 W for ordinary lightning.

Satellite measurements have confirmed the fact that NBEs are the most potent intracloud lightning emitter in the HF and VHF frequency bands (e.g., Jacobson et al, 1999; Jacobson and Light, 2012). Jacobson et al. (1999) studied radio frequency emission from the lightning using the VHF receivers (20-300 Mhz) on the FORTE satellite and observed intense VHF emission associated with NBEs in the form of “transionospheric pulse pairs” or TIPP; TIPP were coincident with NBEs found with LASA (Los Alamos Sferic Array), as described in Smith et al. (2004).

Positive NBEs were originally reported to occur as single isolated events (e.g., Le Vine, 1980; Willett et al., 1989; Smith et al., 1999). However, more recent studies suggest that NBEs often are associated with other lighting processes, especially for initiating some intracloud (IC) lightning flashes (e.g., Rison et al., 1999; Nag et al., 2010; Wu et al., 2011; Wu et al., 2014; Karunarathne et al., 2015, Rison et al. 2016).

Based on LMA observations, Rison et al. [1999] reported that 13 positive NBEs initiated ICs flashes. Nag et al. [2010], based on 157 records of NBEs, reported that 9 of 157 occur in association with CG flashes with 7 of 9 NBEs located using the National Lightning Detection Network. Nag et al. [2010] also found that 5 of the 157 NBEs occurred before IC flashes within 5.3 – 67 ms with horizontal separation < 1 km. Wu et al. (2014) found that 103 out of 638 positive NBEs were followed by IC flashes within 10 ms. Karunaratne et al. (2015) found that 62.8% of 226 positives NBE were associated with one or more lightning events. More recently, Rison et al. (2016) investigated the initiation of lightning using an LMA and a broadband VHF interferometer and found that 10 of 51 IC flashes were initiated by high-power NBEs. Rison et al. (2016) hypothesized that all IC and CG flashes are initiated by NBEs. Rison et al. (2016) study suggested that NBE are caused by “fast positive breakdown.” Moreover, their NBE simulations indicated that NBE breakdown is characterized by large peak currents (50 – 60 kA), relatively small charge transfers (0.5 – 1.0 C), and fast speeds ($4 - 10 \times 10^7 \text{ ms}^{-1}$). Rison et al. [2016] conclude that NBE breakdown composed of a spatially and temporally distributed system of positive streamers. The primary breakdown process associated with positive streamers was described by Phelps et al. [1974].

The present study was based on NBEs data that were recorded during July and August 2016 using a seven-station lightning detection array located in and around Oxford, Mississippi, USA. In this study, NBE and other lightning pulses were located using the $\int dE/dt$ or PBFA methods, depending on the availability of the sensors and their signal-to-noise ratio.

5.2 Identification of NBEs

Identification of positive NBEs through an automated search routine of E-change data has been widely used in previous studies (e.g., Smith et al., 2002; Hamlin et al., 2007; Wu et al., 2011; Wu et al., 2014; Karunarathne et al., 2015). However, in this study, the combination of both E-change and Log-RF data were used to identify positive NBEs. To efficiently capture NBEs from our data set, we have developed an automated procedure that mainly relied on the fact that NBEs tend to be one of the strongest VHF producers in natural lighting (e.g., Le Vine et al., 1980; Willett et al., 1989; Medelius et al., 1989).

The triggered Log-RF data obtained at the EE station was used to find possible candidates for positive NBEs. In each record, we programmatically searched for Log-RF pulses having peak amplitude greater than five times the threshold level. The threshold level used in this procedure was an arbitrary value and was adjusted to find only the largest Log-RF pulses with the corresponding FA pulses to achieve the best description of the positive NBE waveform. In addition to that, the procedure was limited to collecting only positive NBE, so the program required that the initial polarity of the corresponding FA waveform be positive.

Note that this condition is also useful to avoid the collection of additional Log-RF pulses that were not necessary for this study, such as -CG return stroke, negative NBE, some IB pulses in the IC flashes, etc. Furthermore, we required that at least five different sensor locations triggered on each event so that we could locate the pulse using either PBFA or integrated dE/dt .

Finally, we carefully examined the coincident FA waveform associated with each possible RF pulses to make sure that it fit into previously reported positive NBEs waveforms (e.g., Le Vine et al., 1980; Willett et al., 1989; Medelius et al., 1991; Smith et al., 1999; Smith et al., 2004; Ahmad et al., 2010; Nag et al., 2010; Karunarathne et al., 2015).

A large number of Log-RF records were processed using the automated algorithm described above, and the procedure captured a total of 319 positive NBEs. However, for a more detailed analysis, we focus only on positive NBEs with horizontal location errors Δx and $\Delta y < 2$ km and chi-squared goodness-of-fit values < 5 , leaving a set of 201 positive NBEs.

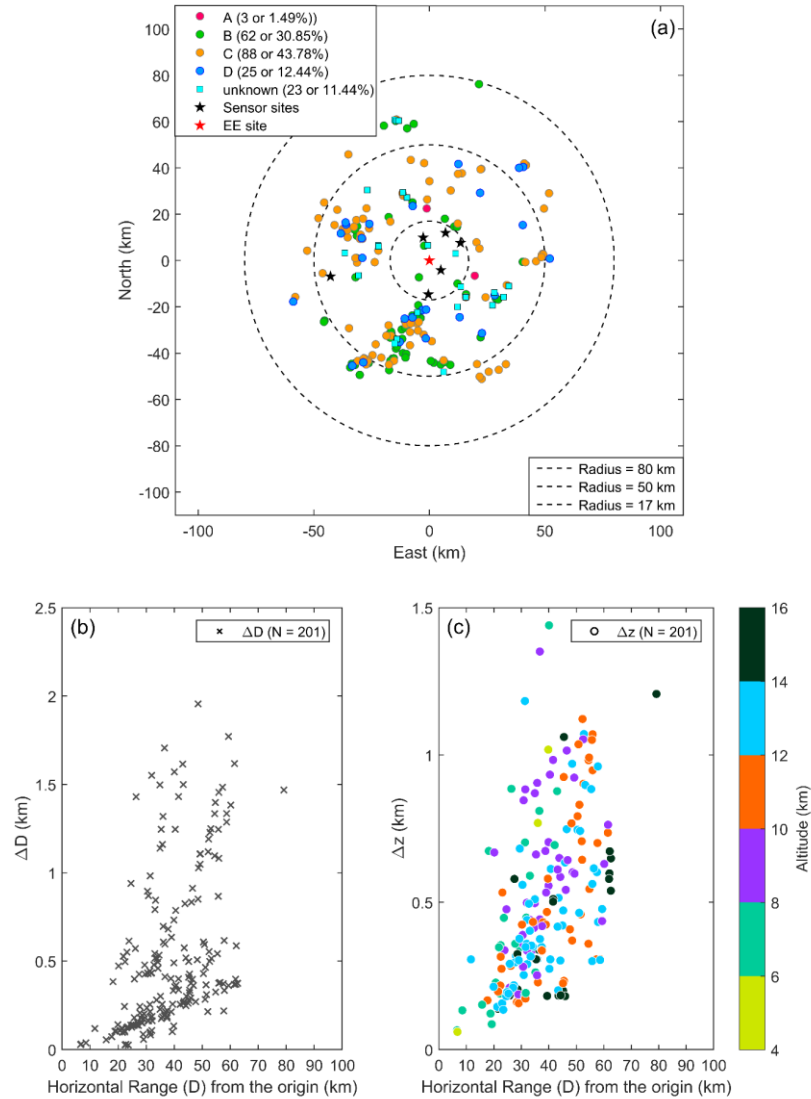


Figure 5.1. (a) Plan view of seven sensor sites (marked with stars) along with locations of 201 NBEs. The central sensor site, EE, is marked with the red star and is the origin of the coordinate system; three range rings are also shown. Type A-D NBEs show in red, green, orange, and light blue color, respectively and rest of the NBE were marked in cyan color. (b) Horizontal distance error (ΔD) marked as "x" for 201 NBEs. (c) Altitude error (Δz) for all NBEs were represented by dots with each NBE colored according to its height.

Figure 5.1a shows the horizontal plan-view of the 201 positive NBEs relative to the EE station. Waveform type A, B, C, and D color-coded into red, green, orange, and light blue, respectively. (The categorization of NBE into type A-D according to their E-change waveform will be discussed in the later section.) Positive NBEs that are not registered as type A-D were marked in cyan color. The horizontal distance (D) of 201 positive NBE ranged between 6 and 80 km. Altitudes of 201 NBEs varied from 5.0 – 15.5 km and the average altitude was 11 km. Figure 5.1b and 5.1c show the errors of horizontal and altitude location for all NBE. The 201 NBEs selected had $\Delta z < 1.5$ km and $\Delta D < 2$ km.

5.3 Categorization of NBEs into Types A, B, C, and D.

The waveform of a positive NBE has long been thought to be a basic bipolar shape with a main positive peak followed by a negative overshoot peak. However, E-change waveforms of positive NBE were reported in some previous studies that indicated that there are some distinguishable features in the waveform rather than a simple bipolar waveform (e.g., LeVine, 1980; Cooray and Lundquist, 1985; Willett et al., 1989; Medelius et al., 1989; Smith et al., 1999; Karunaratne et al. 2015). In particular, Karunaratne et al. [2015] showed that positive NBEs can be divided into four categories (Types A-D) according to their characteristic E-change waveforms.

The positive NBE classification scheme of Karunaratne et al. [2015] was based on the observation of 226 positive NBEs and can be summarized as follows. Type A NBEs have the classic bipolar waveform. Type B NBEs have one or more additional positive peaks just after the negative overshoot, which give noticeable oscillatory shape at the end of the classic bipolar waveform. Type C NBEs have additional pulse or pulses in the main positive peak or between the main peak and the negative overshoot in the bipolar waveform. Type D NBEs have a significant extra peak or peaks just prior to the main positive peak in the bipolar waveform.

Additionally, Karunaratne et al. [2015] noted that there is a possibility for having more than one shape to occur in the same NBE (e.g., Type D also having Type B peaks). It was found that most of the E-change waveforms of NBEs in our set could be categorized using Types A-D (see examples, Figure 5.2). We have categorized 178 of 201 Positive NBEs into Type A-D. The remaining 23 positive NBE could not be easily defined as an A-D waveform due to fuzzy subpulses embedded in the waveform. We call the A-D classification "method 1".

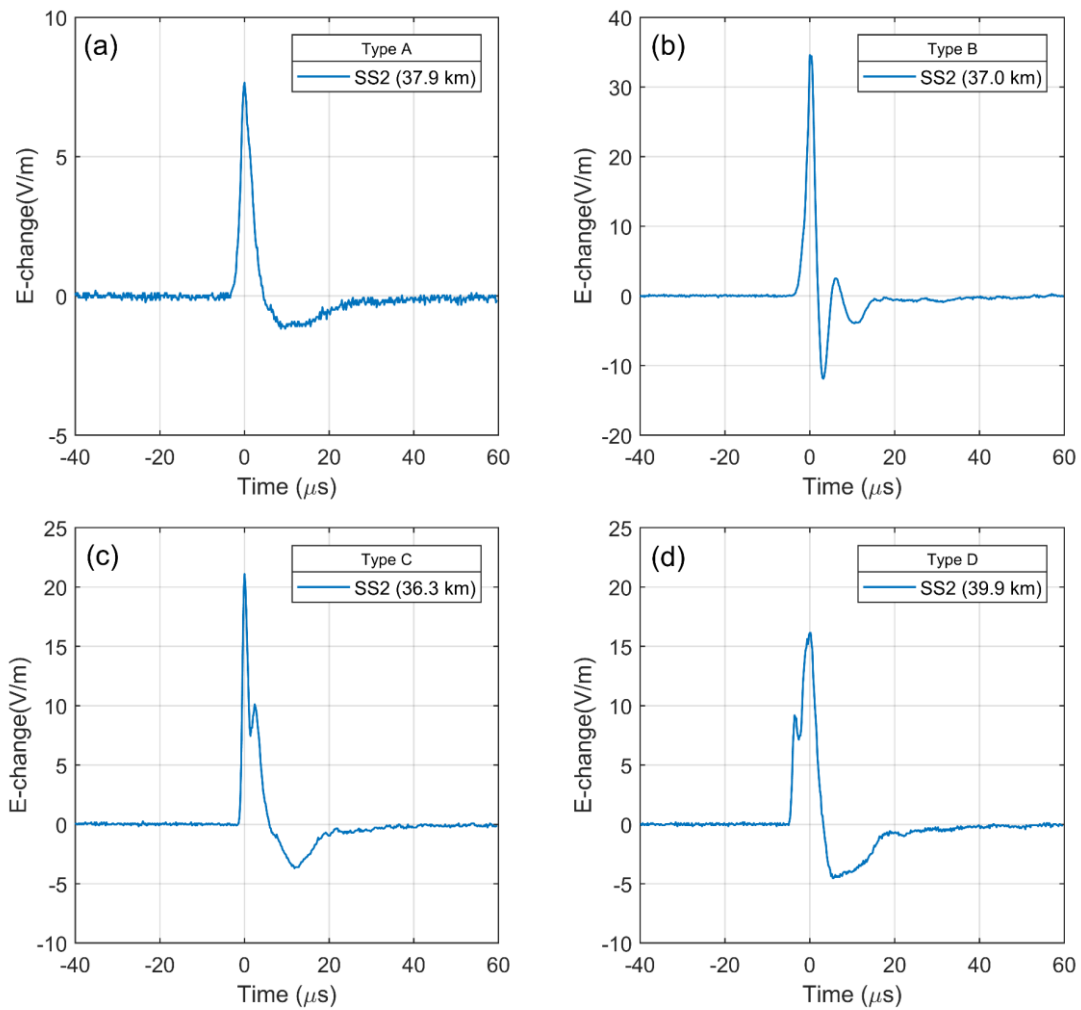


Figure 5.2. Examples of Types A–D NBEs. In each plot, the number inside parenthesis indicate horizontal source distance relative to the SS sensor.

Table 5.1 shows the distribution of 178 of the 201 positive NBEs according to method 1. For comparison, Table 1 also includes the distribution of type A-D NBEs observed in Karunarathne et al. [2015]. Of our 178 NBEs, only 3 NBEs were type A; this value agrees well with the number of type A found in Karunarathne et al. [2015]. These 3 NBEs occurred about 22– 37 *km* horizontally from the EE station. We found 62 positive NBEs had the type B waveform; this was about half the percentage of type B NBEs found by Karunarathne et al [2015]. We found 88 Type C NBEs (44 %) which is much higher than the 13% of type C NBEs in Karunarathna et al.[2015]. The remaining 25 NBEs (12.44%) were type D.

Table 5.1. Number of types A–D NBEs based on current study and Karunarathne et al. [2015].

Method 1	Number of NBEs	
	Current study (178)	Karunarathne et al. 2015 (226)
A	3 (1.49%)	2 (1%)
B	62 (30.85%)	151 (67%)
C	88 (43.78%)	30 (13%)
D	25 (12.44%)	43 (19%)
Unknown	23 (11.44%)	-

5.4 Categorization of NBE according to their spatiotemporal relationship with other lightning activities.

As discussed above, NBEs were originally considered to be isolated in time from other cloud discharges (e.g., Willett et al., 1989, Smith et al., 1999). However, more recent studies show that some of the NBEs had an apparent relationship with other lightning activities (e.g., Rison et al., 1999; Smith et al., 2002; Nag et al., 2010; Wu et al., 2011; Wu et al., 2014; Rison et al., 2016).

Karunarathne et al. [2015] investigated the isolation in space and time of their 226 positive NBEs from other lightning events based on locations given by three lightning locating systems called LDAR2, PBFA, and CGLSS.

They defined “isolated in space” such that no other lightning event occurred within a 10 km radius and defined “isolated in time” such that no other lightning activity occurs within ± 660 ms from the NBE (“pre-pulse” and “post-pulse” time).

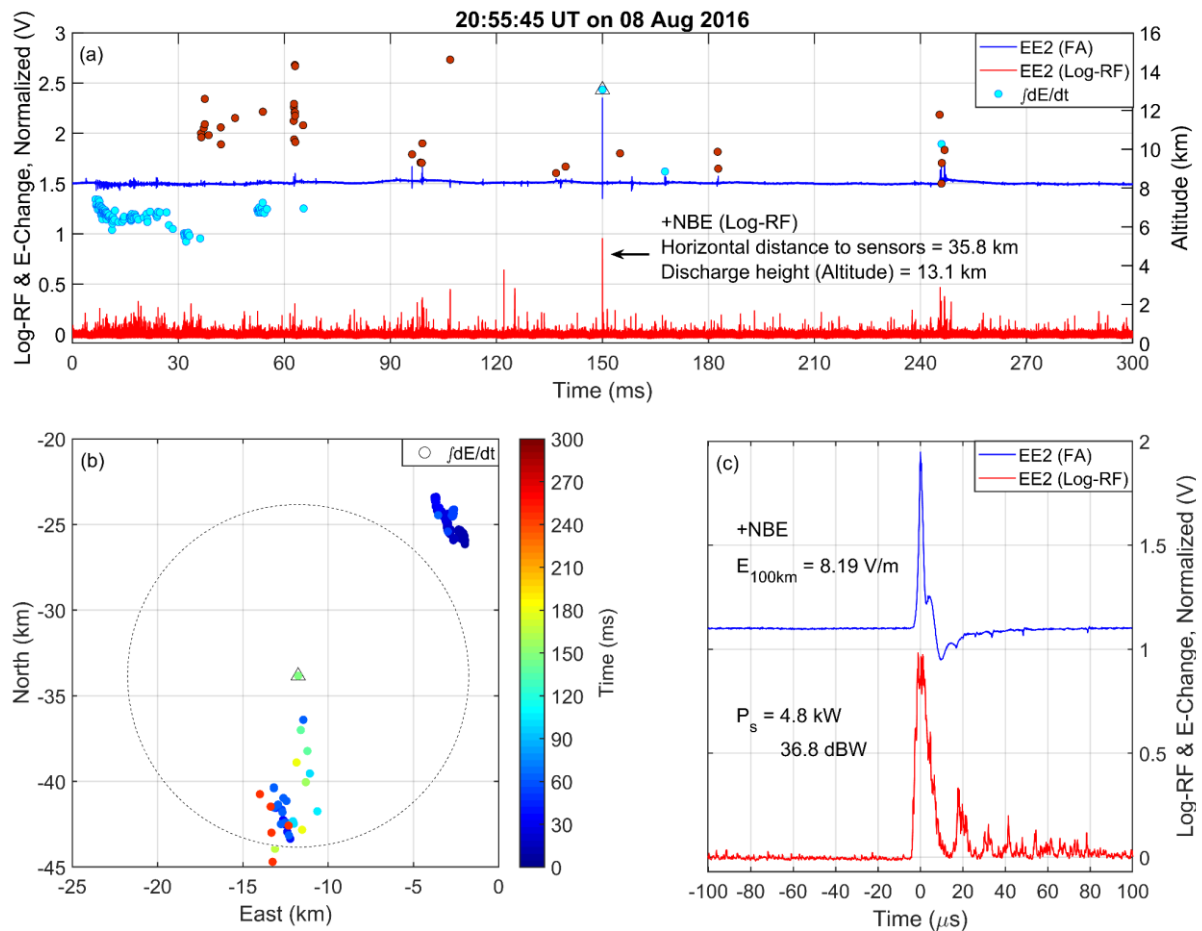


Figure 5.3. Example of an NBE that occurred as a Not-isolated event in a lightning flash. (a) Overview showing 300 ms of FA data (blue) and Log-RF data (red). The light blue and brown points denote the altitudes (right axis) of the FA pulses determined by $\int dE/dt$. Brown dots represent the altitude of each event in a flash within 10 km horizontally from the NBE. (b) Plan position of the lightning discharge in (a). The range of 10 km from NBE (small black triangle) marked by a circle with the dashed line. (c) Expanded view (200 μ s) of the NBE.

Figure 5.3a shows the example of an NBE that occurred within 10 km radius and ± 150 ms time from the other lightning discharge. The NBE happened at 13.1 km altitude and 35.8 km from the EE site. The altitude of lightning events with light blue dots occurred beyond 10 km from the NBE while events with brown dots occurred within 10 km of the NBE.

Figure 5.3b shows the X-Y location of all the events in Figure 5.3a color-coded by time. The NBE's plan position is indicated by the triangle and a dotted circle with a radius of 10 km to show which events occurred within 10 km. Therefore, all lightning events indicated by brown dots in Figure 5.3a were within the circle. In Figure 5.3c shows the waveform of FA and Log-RF data associated with NBE on a 200 μ s scale. The NBE had a range-normalized FA amplitude (E100km) of 8.19 V/m and a VHF power of 4.8 kW (36.8 dBW).

Based on the location given by PBFA and $\int dE/dt$ and with the help of the isolation parameters described in the previous study, we developed “method 2” of categorizing our positive NBEs data set. Method 2 divided the NBEs into three groups called ‘isolated,’ ‘not-isolated,’ and “INBE.” NBEs in the isolated group were defined by their isolation from any other detectable lightning activities within 10 km radius and ± 660 ms time window from the NBEs. The INBE group was made up of “initiator NBEs” [Wu et al., 2014] since they initiated IC flashes. The remaining NBEs were placed in the ‘not isolated’ group.

Wu et al. [2014] found that 16.1% of 638 positive NBEs were INBEs (initiated IC flashes with an upward propagating positive pulse train that usually started within 10 ms after the INBE). Wu et al. [2014] determined that most INBEs occurred below 10 km altitude while the most of the other positive NBEs occurred above 10 km altitude.

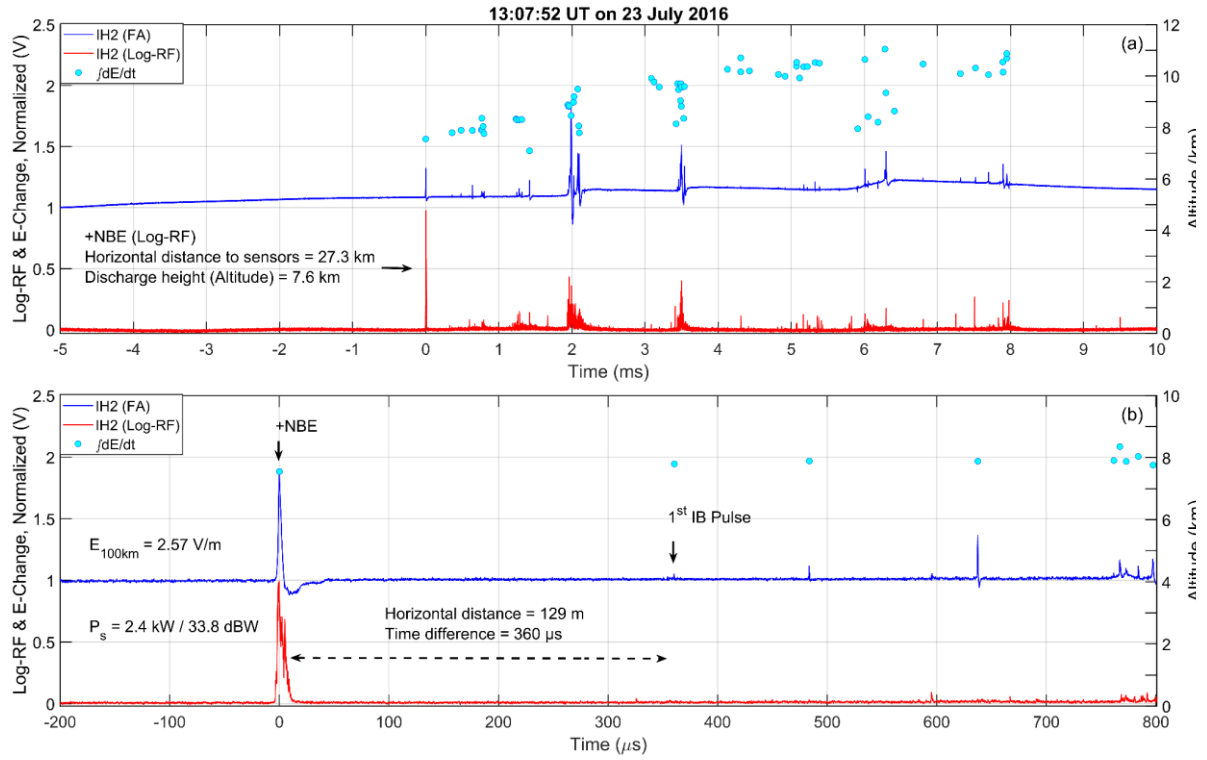


Figure 5.4. Example of positive NBE (+ NBE) that occurred as the initial event (INBE) of an IC flash. The FA data (blue) and the Log-RF data (red) are shown as normalized voltages. (a) First 15 ms of the IC flash that includes 5 ms of pre-INBE data and 10 ms of post-INBE data. The altitudes of the FA pulses (Light blue dots) shows on the right axis and were determined using $\int dE/dt$. (b) Expanded view (1 ms) of INBE and first IB pulses.

Figure 5.4a shows an example first 15 ms of IC flash started by an INBE. Pulse altitudes were determined using $\int dE/dt$. The flash started with an INBE at altitude of 7.6 km and developed upward. In this example, NBE was the initial event of the IC flash based on both the FA data and the Log-RF data, there was no detectable lightning activity before NBE. Also, the first IB pulse in the positive pulse train occurred after <1 ms after NBE.

Figure 5.4b is overview of the first 1 ms of the IC flash, including the NBE and first IB pulse in the flash. The horizontal distance between the NBE and the 1st IB pulse was 129m with an uncertainty of 288 m, while their separation in time of 360 μ s has an uncertainty < 1 μ s. Figure 5.4b also indicates that the NBE had a range-normalized FA amplitude (E_{100km}) of 2.57 V/m and a VHF power of 2.4 kW (33.8 dBW).

In our INBE group, positive NBEs were identified as INBE because they show the following additional criteria to the definition of the not-isolated group as seen in Figure 5.4: (1) The positive INBE was the initial event of IC flash, (2) INBE followed by IB pulse of IC flash start within 10 ms, (3) The INBE was close in time and space to the first IB pulse in the pulse train. In this study horizontal distance from the INBE to the first IB pulse range from 0.1 to 7.9 km with mean 1 km, while the time difference between the INBE and the first IB pulse varied from 0.2 to 6.7 ms with an average of 2.1 ms. Using method 2, 136 of 178 NBEs were categorized into INBEs, isolated NBEs, and not-isolated NBEs.

Table 5.2. Number of INBEs, isolated, and Not-isolated NBEs.

Method 2	Number of NBEs
INBE	72 (40 %)
Not-isolated	46 (26 %)
Isolated	18 (10 %)
Unknown	42 (24%)

Table 5.2 shows the distribution of NBEs according to method 2 classifications. Most of 72 (40%) of positive NBEs were INBEs (compared to 16% INBEs by Wu et al. (2014)). In addition, 46 NBEs (26%) were Not-isolated and only 18 NBEs (10%) were isolated events. This amount is much smaller compared to 37.2 % or 77 of NBEs found in the Karunaratne et al. [2015]. We were unable to locate other FA pulses for 42 NBEs so we could use them with the method 2 categories.

Table 5.3. Number of NBE found in method 1 classification within method 2.

Method 2	Method 1			
	A (3)	B (62)	C (88)	D (25)
INBE	3 (100.00%)	14 (22.58%)	47 (53.40%)	8 (32.00%)
Not-isolated	0 (0.00%)	26 (41.94%)	15 (17.05%)	5 (20.00%)
Isolated	0 (0.00 %)	7 (11.29%)	9 (10.23%)	2 (8.00%)
Unknown	0 (0.00%)	15 (24.19%)	17 (19.32%)	10 (40.00%)

Table 5.3 shows the number of NBEs categorized according to method 1 (Type A-D) found within the categorization of method 2 (INBE, Not- isolated, and Isolated). Types A, C, and D were the most dominant waveforms found in the INBE group while the majority NBEs found non-isolated group had type B waveform.

5.5 Statistical investigations.

In the following section, we report the statistical result of NBE based on the 201 samples. 178 of 201 were categorized into Type A-D and Among 136 was group into INBE, Not-isolated, and Isolated of three groups.

5.5.1 FA waveforms of NBEs.

The E-change waveform properties of NBEs have been discussed and reported extensively in many previous studies. For example, Karunarathna et al. (2015) studied NBE waveform with E-change data from 10 sites at Kennedy Space Center (KSC), Florida. They measured some common waveform properties of NBEs using essentially radiation component of E-change data. Table 4 shows the comparison of waveform parameters observed in the current study and those found in Karunarathne et al. (2015). FA amplitudes of NBEs were range-normalized amplitude to 100 km using $1/R$ normalization where R is the slant range from the NBE to the FA sensor. The all the waveform properties value of NBEs was determined from FA sensors with range > 20 km.

Table 5.4. Comparison of FA waveform properties of NBEs.

References	Type	Peak amplitude (V/m)	Rise time (μ s)	FWHM (μ s)	Zero cross (μ s)	Pulse duration (μ s)
current study	A	2.0 ± 0.6	2.0 ± 0.2	3.2 ± 0.1	8.7 ± 2.0	30.1 ± 5.4
Mississippi (USA)	B	8.7 ± 5.1	2.3 ± 0.9	2.4 ± 0.7	8.5 ± 3.8	32.8 ± 10.4
(N = 178)	C	7.8 ± 3.1	1.9 ± 0.8	3.5 ± 1.8	9.4 ± 3	32.3 ± 10.2
	D	7.4 ± 2.6	3.9 ± 1.5	4.6 ± 2.0	9.3 ± 2.6	33.5 ± 10.6
N = 201	TP	8.0 ± 4.0	2.4 ± 1.5	3.3 ± 2.0	9.7 ± 5.5	33.4 ± 11.9
Karunaratne et al. (2015)	A	12.2 ± 1.1	2.0 ± 0.0	3.1 ± 1.3	7.3 ± 1.0	-
Florida (USA)	B	12.4 ± 6.8	2.4 ± 1.3	2.0 ± 0.7	9.0 ± 4.2	-
(N = 226)	C	8.4 ± 3.9	1.5 ± 1.1	4.6 ± 2.6	12.7 ± 5.6	-
	D	8.4 ± 4.1	4.3 ± 3.1	4.0 ± 1.6	11.1 ± 5.2	-
N = 226	TP	11.0 ± 6.2	2.6 ± 2.0	2.8 ± 1.8	9.9 ± 4.8	-

* TP- typical values for individual properties

From Table 5.4 we can see that all the time parameters were in good agreement with those found in Karunaratne et al. (2015). The range normalized peak amplitude measured in this study for NBEs is smaller than the $(11.0 \pm 6.2) Vm^{-1}$ reported by Karunaratna et al. (2015), but they stated that their sample expected to have a larger amplitude NBEs. However, our peak amplitude value was in good agreement with $(8.0 \pm 5.3) Vm^{-1}$ reported by Willett et al. (1989). In summary, waveform properties values found in this study for positive NBEs agree with previous studies.

5.5.2 Log-RF waveforms of NBEs

Although the FA waveform properties of positive NBEs are well known, the corresponding Log-RF waveforms have not been extensively studied. In this study Log-RF waveforms properties were characterized by zero cross time and rise time.

Each Log-RF measurement for NBE obtained by averaging measurements from at least 4 sensor sites. Additionally, data were smoothed by resampling data into 1 MHz. The Log-RF “zero-cross” time of 201 NBEs in this study varied from 3.7 to 28.1 μs , with the averaged value of 12.1 μs with standard deviation of 3.6 μs . In this study, the “zero-cross” time of a Log-RF waveform was defined as the width of the initial positive peak at 10% of its maximum amplitude. The mean rise time (10–90% of the peak value) of Log-RF waveforms found in this study was $(3.1 \pm 1.5) \mu\text{s}$, while values varied from 1.1 to 8.9 μs . Figure 5.5 shows the zero-cross and rise time parameters of FA and Log-RF waveforms.

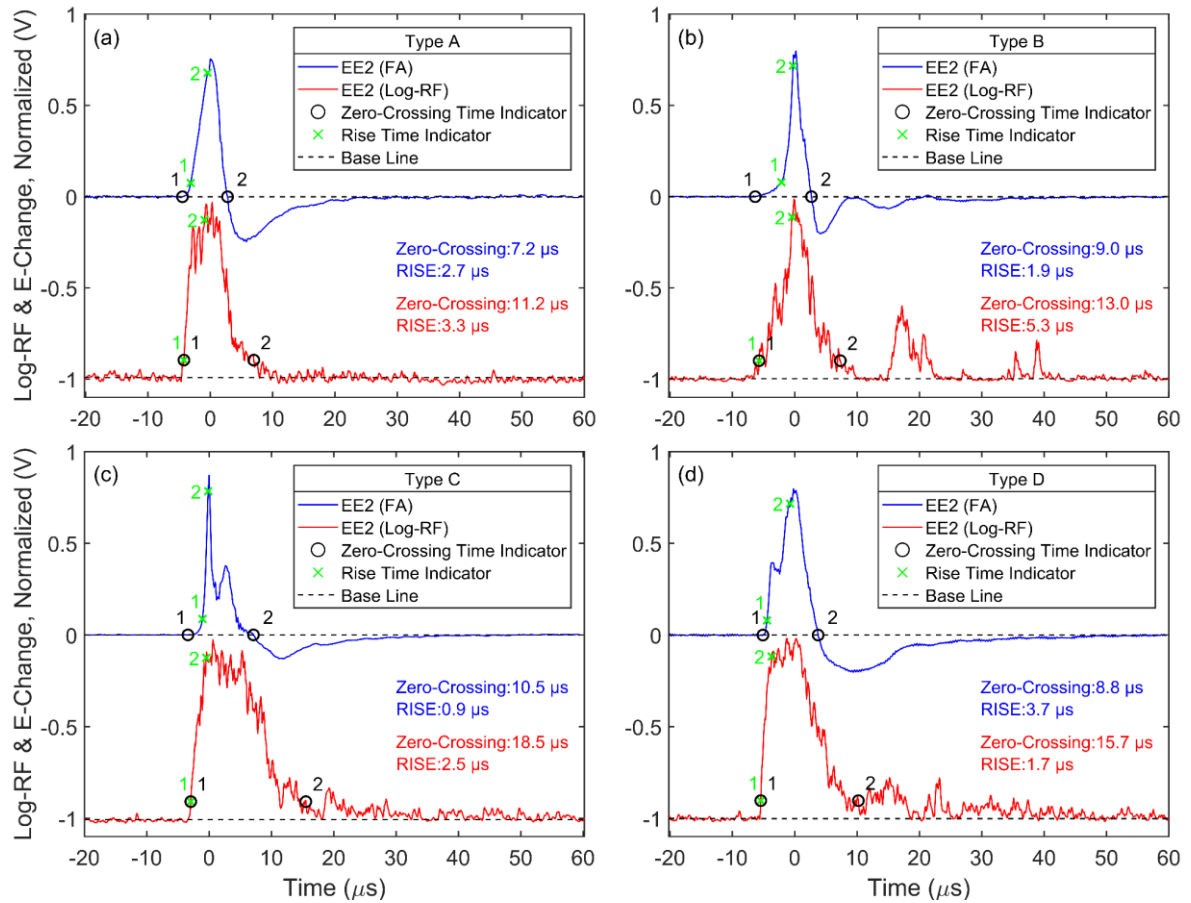


Figure 5.5. Shows the definition of the rise time and zero crossing time parameters of the type A-D waveform that were recorded by FA and the Log-RF antenna. The beginning and ending times of the zero-crossing time for the FA and Log-RF waveforms are indicated with a black circle, while the beginning and ending times for the rise time are indicated with the green “x” for both waveforms.

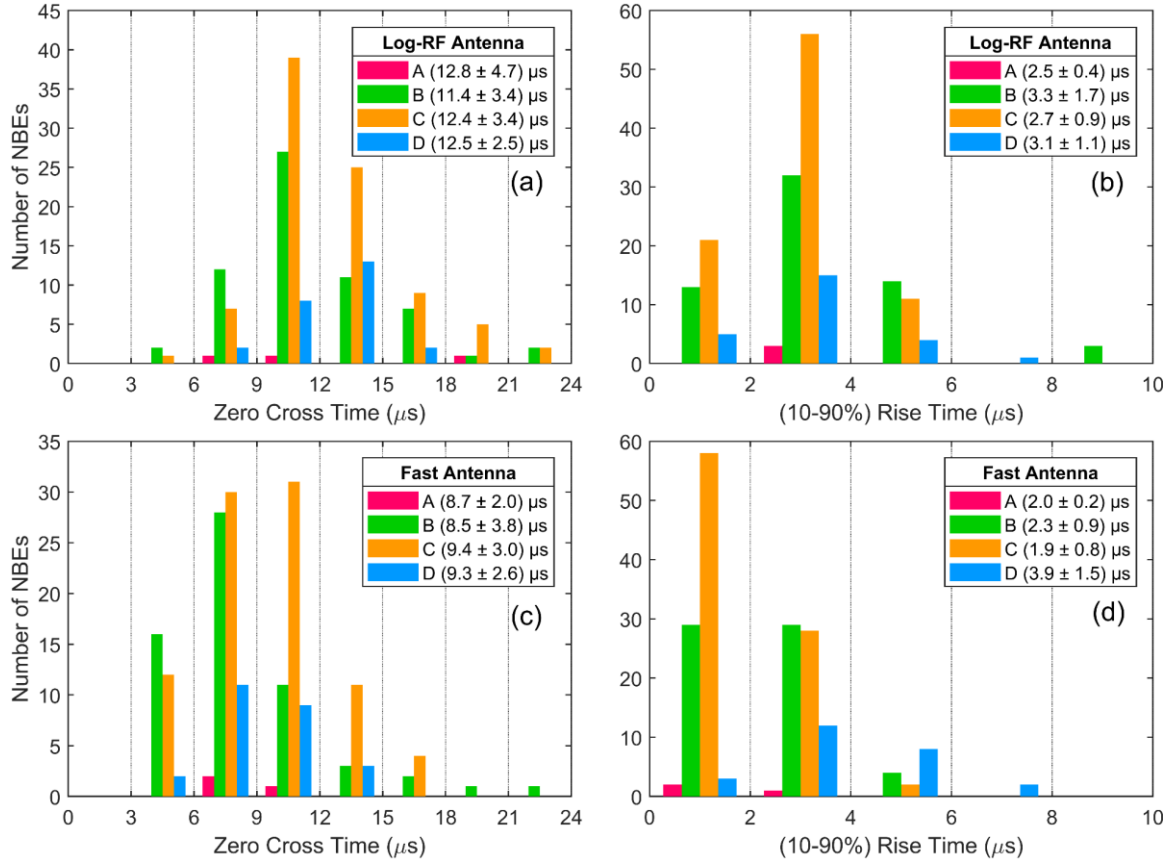


Figure 5.6. Comparison of zero cross and rise time of Type A-D waveforms using Log-RF (Top) and FA (bottom) data. The legend of each plot includes (parenthetically) the arithmetic mean \pm standard deviation of relevant property. The grid lines in each figure show the bin edges.

Figure 5.6 shows the comparison of the zero cross time and the rise time of Type A-D NBEs that were measured using Log-RF (top) and FA (bottom) antenna. The average values of zero crossing and rise time for Type A-D found in the Log-RF waveform were slightly larger than those of the FA waveform. For most NBEs, the duration of the main Log-RF pulse was about 150% of the duration of FA positive pulse of the bipolar NBE; see example NBEs in Figure 5.5.

5.5.3 VHF source Power of NBEs in Method 1.

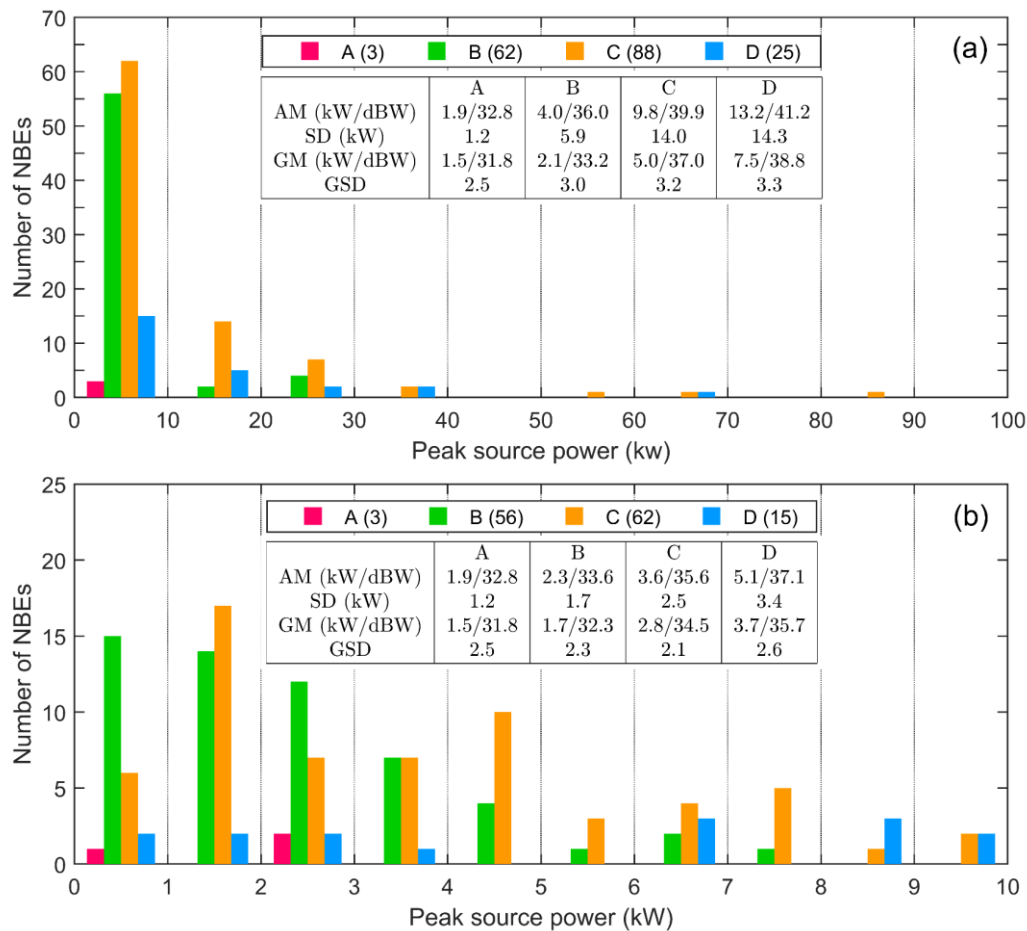


Figure 5.7. (a) Distribution of peak radiated power for the Types A-D of NBEs. (b) An expanded view of 0 – 10 kW. The legend of each graph includes the number of NBEs (in parentheses), in the table the arithmetic mean (AM), the geometric mean (GM), the standard deviation (SD) and the geometric standard deviation (GSD) for powers related to each type.

Figure 5.7a shows a histogram of the radiated peak powers for the Type A-D of NBEs. For each NBE type, the arithmetic mean (AM) with its standard deviation (SD) and geometric mean (GM) with its standard deviation (GSD) are given. Figure 5.7b shows the distribution of the radiated peak powers for Type A-D of NBEs within a power range of 10 kW. The legend of the plot shows how many NBE are in each type found in the range of 10 kW. As seen in figure 5.7a-b, more than 60% of type A-D had a peak power less than or equal to 10 kW. Also, the maximum power of all the NBEs in type A were less than 10 kW.

However, radiated powers of many types C and D extended above 10 kW, as indicated by their mean and stranded deviation values of 9.8 ± 14 kW and 13.2 ± 14.3 kW, respectively. According to Figure 5.7a, NBE C and D types appear to be the most energetic of NBE types, in contrast to types A and B.

5.5.4 VHF source Power of NBEs in Method 2.

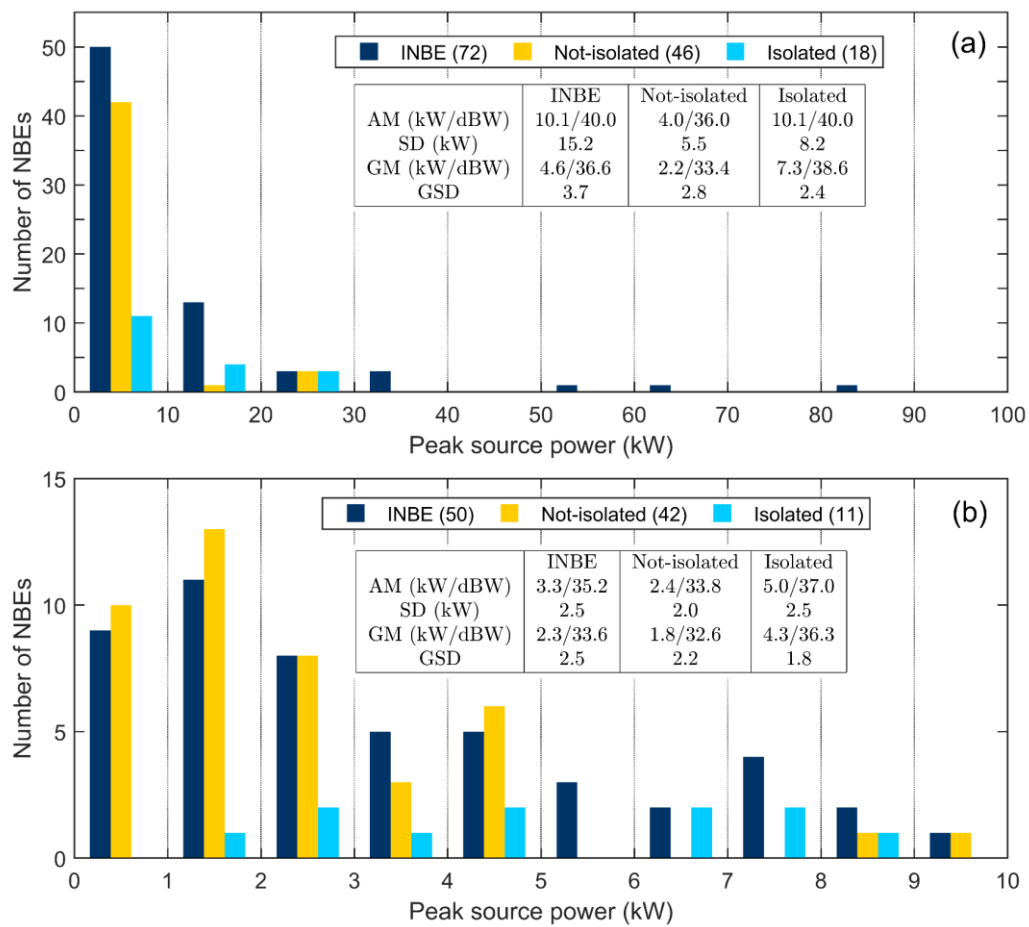


Figure 5.8. Histograms of VHF powers of the three NBEs groups; INBE, Isolated, and Not-isolated: (a) overall distribution, (b) expanded view of 0 – 10 kW. AM = arithmetic mean, SD = standard deviation of AM, GM = geometric mean, GSD = standard deviation of GM. The legend of each plot includes (parenthetically): in (a) amount of NBEs in each group, in (b) number of NBEs that have peak power < 10 kW.

The figure 5.8a shows the overall distribution of peak source power for the three groups INBE, Not-isolated, and Isolated. From panel (a), 31% of NBEs in the INBE group have powers > 10 kW. This value for the Not-isolated and Isolated groups were 7% and 39 %, respectively. Panel (b) shows the distribution of source powers for the three groups within the power range 0-10 kW. INBEs and Isolated NBEs had the largest peak powers, as indicated by their arithmetic mean value of 10.1 kW, and INBEs had the largest range of peak powers.

Based on the broadband VHF interferometer and the LMA observation, Rison et al. (2016) found that positive NBEs that initiate IC flashes had a wide range of strength. For example, their data presented for 51 of ICs had VHF powers in the range of -20 to 60 dBW. Although the VHF receivers were in a different frequency band compared to the current study, we also found that a wide range of source power for NBEs in the INBE group.

5.5.5 Characteristic of Rise time of Log-RF waveform.

Figure 5.9 shows scatter plots of the peak radiated powers versus rise time of the Log-RF waveforms for NBEs of types B-D of NBEs (Figures 5.9 a, b, c), and for NBEs in the INBE, not-isolated and isolated groups (Figures 5.9 d, e, f). There is a total of 175 Type B-D of NBEs and 136 NBEs in the INBE, not-isolated and isolated groups. NBEs in Type A were excluded due to the small sample size. The Spearman correlation coefficients (ρ) and the probability values (p) for type C NBEs and for the INBE group in Figure 5.9 indicate that, with increasing NBE peak power, the rise time of the NBE Log-RF waveform decreases.

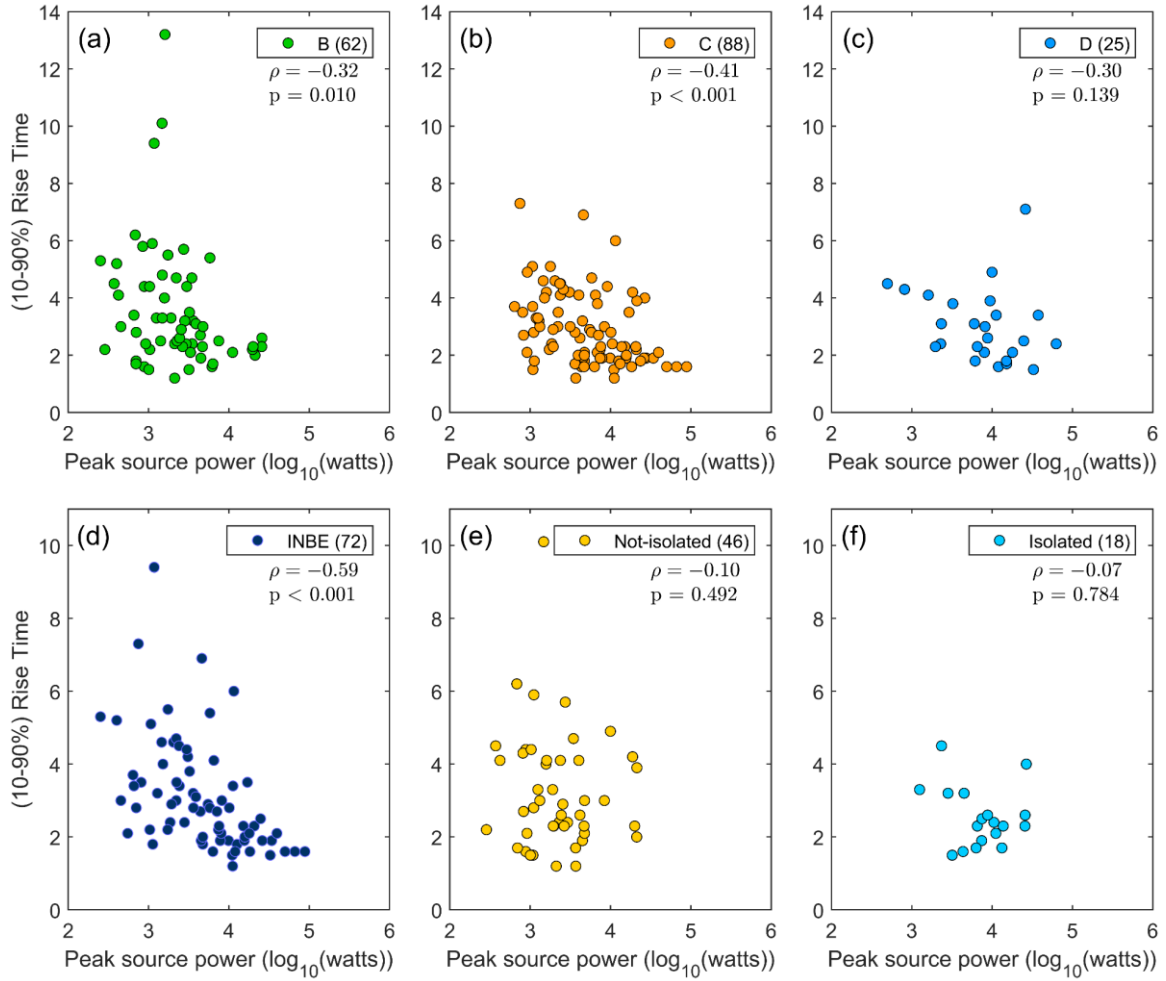


Figure 5.9. Scatter plots of the peak radiated power versus the rise time of the Log-RF waveform for: (a) – (c) Type B-D of NBEs. (d)-(f) all NBEs found in INBE, not-isolated, and isolated and groups. The legend of each plot includes (in parentheses) the number of NBE found in each type (B-D) and group (INBE, not-isolated, and isolated). ρ = The Spearman correlation coefficient. p = probability value.

Note that Spearman rank correlation coefficient is a non-parametric statistical measurement, and it weighs (or ranks) the strength of the monotonic relationship between two data sets. The correlation coefficient ranges between 1.0 (strong correlation) and -1.0 (strong anti-correlation) with zero indicating no correlation between the data sets. Additionally, its level of statistical significance based on the probability value (p). Smaller p values indicate stronger correlation between the two data sets. Therefore, the p -value is a measure of how likely there is a correlation between two sets of data.

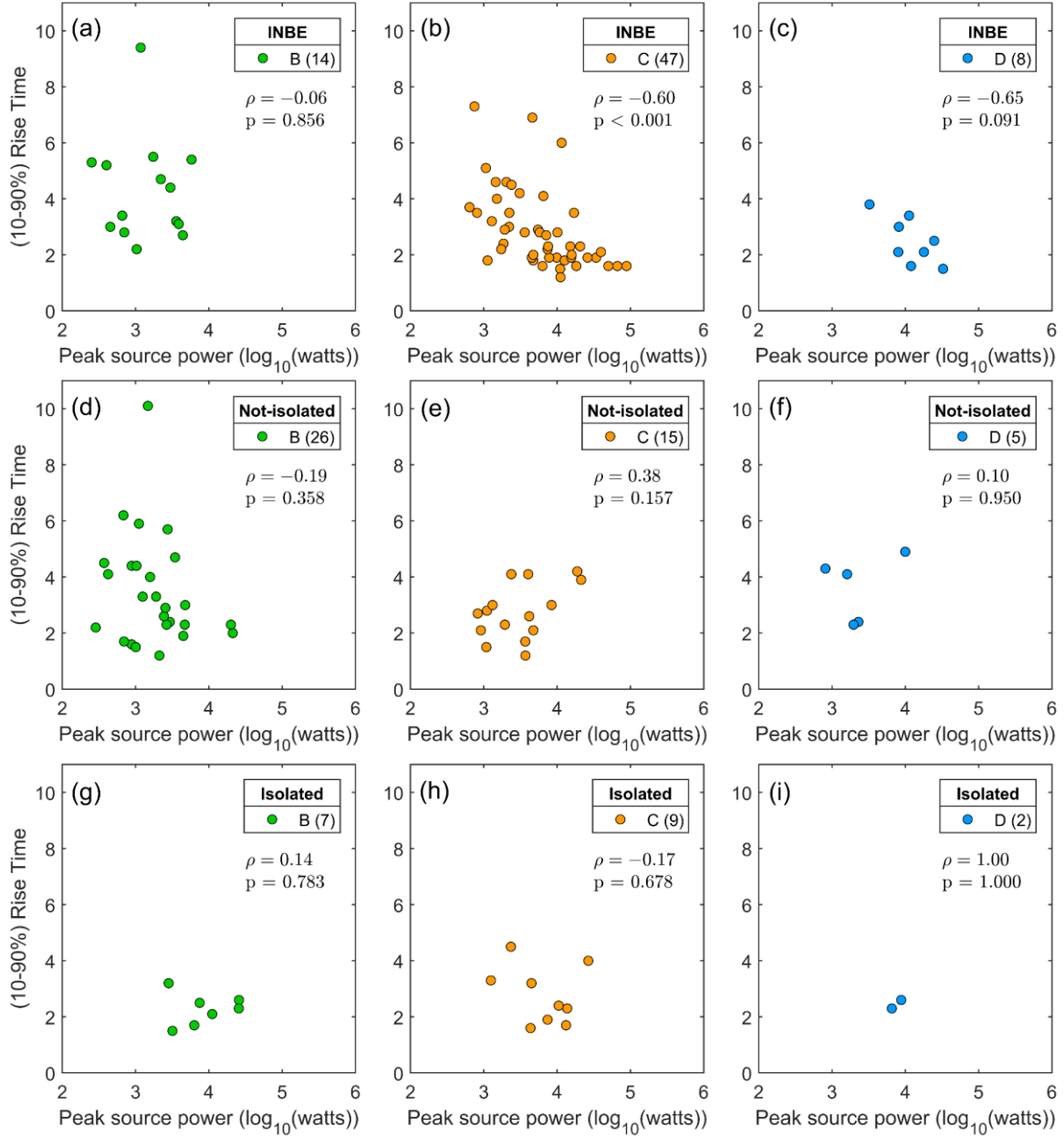


Figure 5.10. In the same format as Figure 5.9, (a) – (c) Type B-D of NBEs found in INBE group. (d)-(f) Type B-D of NBEs found in Not-isolated group. (g)-(i) Type B-D of NBEs found in Isolated group.

Figure 5.10 shows scatter diagrams of the peak radiated powers versus the rise time of the Log-RF waveforms as similar to Figure 5.9, for NBEs of types B-D of NBE that were in the INBE, not-isolated, and isolated groups. From Figure 5.10a, the correlation coefficient found for Type C NBEs in the INBE group indicates that there is a significant negative correlation between waveform rise times and peak radiated powers so that the waveform rise time tends to decrease with increasing peak radiated power.

We note that there is strong correlation for type D NBE found in INBE and Isolated group, but their sample sizes are too small to conclude any relationship.

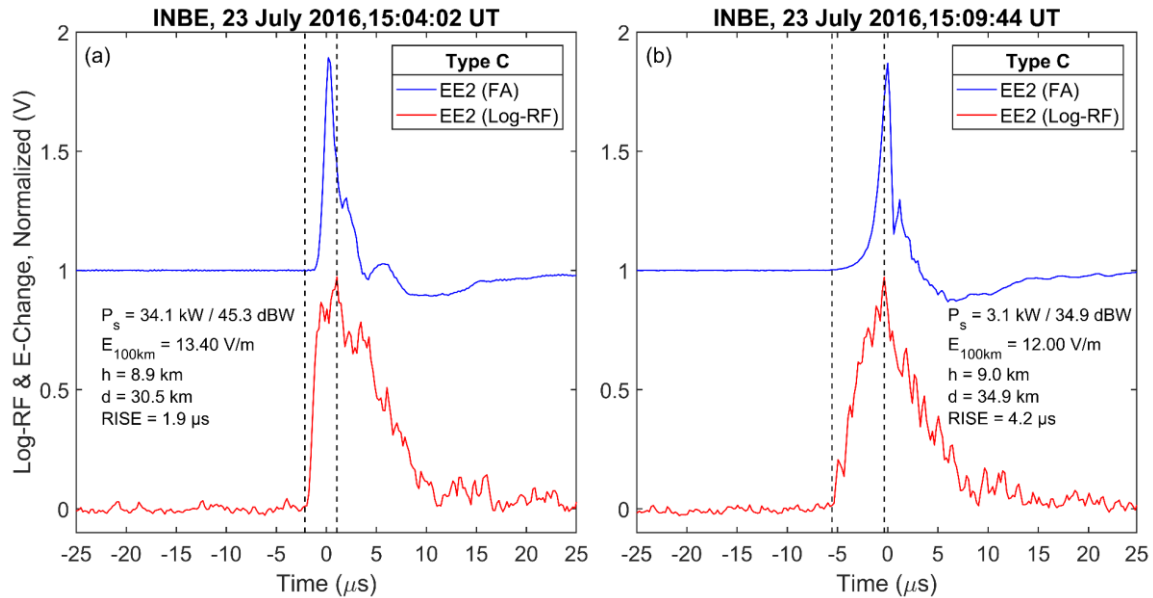


Figure 5.11. Examples of Type C NBE waveform found in INBE group. The FA data (blue) and Log-RF data (red) are both shown as normalized voltages. P_s = radiated peak power in kW/dBW. E_{100km} = range-normalized Electric field amplitude at 100 km. h = discharge height of the NBE. d = Horizontal distance of NBE from EE sensor site. RISE = Rise time (10–90% of the peak value) of Log-RF waveform. (a) NBE that has a high radiated peak power. (b) The NBE has a relatively low peak radiated power.

Figure 5.11 shows example of two type C NBEs found INBE group. It shows characteristic of VHF radiated power variation with Log-RF waveform rise time. The vertical lines in the figure indicate the beginning and the peak position of the Log-RF waveform. Figures 5.11a and 5.11b show waveform of FA and Log-RF for Type C NBEs. Peak power of the NBE in Figure 5.11a was more than 10 times stronger than the power of NBE on Figures 5.11b and their rise times were 1.9 μ s and 4.2 μ s, respectively.

The NBE waveforms in Figure 5.11a and 5.11b had the following characteristics, as observed by FA and Log-RF data.

1. They both show Type C characteristics in FA data.
2. The FA and Log-RF waveform of NBE in Figure 5.11a had a more abrupt change at the beginning of the waveform compared to the NBE in Figure 5.11b.
3. Log-RF waveform of NBE in Figure 5.11b had more subpulses at both rising and falling portion of the waveform compare to the Log-RF waveform in Figure 5.11a

5.6 Summary and Conclusions.

We analyzed 201 positive NBE using data from fast antennas and Log-RF antennas. The dE/dt data in this study was mainly used to locate NBE and other lightning activities. We classified 178 of 201 NBEs as Type A-D according to their characteristic of E-change waveform; 136 of 178 were also identified and grouped into INBE, not isolated and isolated groups according to their spatiotemporal relationship with other lightning activities.

Based on the FA E-change waveforms, the Log-RF waveforms, and their associated characteristic parameters, we found the following conclusions.

1. Arithmetic mean values of range-normalized FA E-change amplitudes for Type A-D of NBEs suggest that Type B NBEs seems to produce larger amplitude E-change waveform in contrast to Type C and D.
2. Arithmetic mean values of peak radiated power associated Type A-D of NBEs show that Type C and D NBEs seem to be the most energetic types of NBE.
3. Peak radiated power comparison among INBE, Not-isolated, and Isolated group show that the largest peak radiation power of NBEs can be found within INBE and Isolated groups with the INBE group showing the largest peak power variation.

4. The relationship between the peak radiation powers and the rise time of the Log-RF waveform show that there was a significant negative correlation so that the rise time of the Log-RF waveform tends to decrease with increasing peak radiation power for Type C NBEs and for the INBE group. This relationship is also significant for type C NBE found in the INBE group.

CHAPTER 6

THE OCCURRENCE OF MULTIPLE NBES WITHIN THUNDERSTORMS

In this chapter we will observe and discuss multiple NBE discharge events. Fast antenna and Log-RF data are used to examine various NBE discharge events. To study the storm structure, the next-generation weather radar (NEXRAD) will be used.

6.1 Introduction

A narrow bipolar event (NBE) is an intra-cloud lightning discharge event, and its discharge has many distinct features. Therefore, it can be uniquely identified among ordinary (normal) lightning discharge. Some of their characteristic are as follows: NBE discharge associated with strong VHF emission, they occur in compact region with estimated channel length less than 1 km (e.g., Smith et al.,1999; Rison et al.,2016), they have large peak current and unusually fast propagation speed ($\sim 5 \times 10^7$ m/s). Although NBE occurs as the first event or part of many lightning flashes (e.g., Rison, 1999; Nag, 2010; Wu, 2011; Wu, 2014; Karunarathne, 2015; Rison et al.,2016), a large percentage of NBE are isolated events.

Among their distinct features recently found that NBE can be used for monitoring severe convective activities in thunderstorms. Suszcynsky and Heavner, 2003 observe that strong statistical correlation between NBE discharge rate and cloud-to-ground (CG) lightning flash rates. Also, they found that NBE occurrence height increase with increasing NBE discharge rate.

From this observation, they deduce that NBE flash rates and source heights are driven by the strength of the convective updraft in thunderstorms. However, Wiens et al. (2008) statistically compare NBE rates to non-NBE lightning rates with convective strength of thunderstorms inferred from radar data at Great Plains in the USA, found that insignificant correlation between NBE rate and convective strength of thunderstorms. Additionally, Wiens et al. (2008) found that NBE discharges often occurred in clusters in storms and suggested that their occurrence was perhaps indicative of specific types of storms or particular stages in convective development.

Smith et al. (1999) study radio frequency emission of NBE with the help of 3 multiple stations E-change meter along with three broad bands (3–30MHz) receiver. Smith et al. (1999) found that NBEs tend to occur as isolated events and they commonly occurred within or near to deep reflectivity cores of the thundercloud. Wu et al. (2013) studied the location of NBE discharges in relation to the structure of thunderstorm using a phased array radar in the Osaka region of Japan. Wu et al. (2013) found that positive NBEs did not occur in deeper convection; instead they occurred around and outside of the deeper convection regions. Furthermore, they observed that positive NBE usually occurred well within the thundercloud, while negative NBEs usually occurred close to the upper boundary of a thundercloud.

Karunarathna et al. (2015) analyzed the locations of 172 positive NBE with thunderstorm radar echo structure found in the Florida storm. They found that 79 % of them occurred in or above the high-reflectivity core while 17 % of NBEs were found next to the reflectivity core. The remaining NBEs (4%) occurred in the anvil region of storms. Additionally, Karunarathna et al. (2015) observed that the number of NBEs in a storm increased as the storm's reflectivity increased.

6.2 Data and Methodology.

The NBEs data used in this study are a subgroup of the 201 NBEs studied in chapter 5. After careful observation of the 201 positive NBEs, it was determined that some positive NBEs occurred in groups, even though NBEs are usually reported to occur as a single isolated events or as the initial event in IC flashes (INBEs). We found that 26 of the 201 NBEs occurred in groups of 2 NBEs along with one group of 3 NBEs and one group of 5 NBEs. Surprisingly, 3 of the NBE pairs had both positive and negative NBEs. Detailed descriptions of the methods for detecting and locating NBEs can be found in chapters 4 and 5.

Table 6.1. Number of NBEs groups

Discharge Type	No. of groups
Doublets ($N = +2$)	10
Triplets ($N = +3$)	1
Quintuplets ($N = +5$)	1
(+) & (-) NBEs within the doublet	3

We define the occurrence proximity for NBEs in a single group as those that occurred within a 10 km radius and a ± 660 ms time interval from the first NBE of the group. Those parameters are similar to Isolation parameters discussed in chapter 5. There were 34 NBEs that occurred in 15 groups as follows: 10 pairs of positive NBEs, 3 pairs of a positive NBE and a negative NBE, 1 group of 3 positive NBEs, and one group of 5 positive NBEs (see Table 6.1). We note that of the 10 groups with two positive NBEs, one group really had a time sequence of three positive NBEs, but since we could locate only two of them, we consider this case as a pair. Similarly, the group with 5 NBEs really had 6 positive NBEs within the time period, but we could locate only 5 of them.

This study uses volumetric Plan Position Indicator (PPI) radar reflectivity scans from the Next Generation Weather Radar (NEXRAD) in Memphis, TN, operated by the NOAA/National Weather Service. To investigate the storm radar structure coinciding with each NBE, the location given from the $\int dE/dt$ or PBFA was overlaid on PPI radar reflectivity scans and on vertical cross sections of radar reflectivity data. Construction of a vertical cross section from volumetric measurement of radar reflectivity data has been described in Karunarathna et al. (2015, 2017). Each radar volume is composed of 360° azimuth scans at 14 elevation angles and takes 3.5 to 5 min to complete. Therefore, to construct the vertical cross sections, we used volumetric radar data for the 5 min time interval in which the NBE discharge happened.

6.3 Space and Time development of NBE Groups.

6.3.1 Altitudes, range-normalized amplitudes, and VHF powers of NBEs in groups.

Figure 6.1 shows the altitudes, range normalized FA amplitudes, and VHF powers of the 34 NBEs that occurred in the 15 Groups. In Figure 6.1(a) the altitudes of the 31 positive NBEs varied from 5.0 – 16.2 km with an average altitude of 12.9 km and a standard deviation of 2.3 km. The heights for 3 negative NBEs discharges were 15.7, 15.0, and 12.7 km and their opposite-polarity associate (positive NBE of pair) occurred at heights of 14.0, 13.8, and 13.2 km, respectively. Many previous studies show that altitude of positive NBEs are generally lower than negative NBEs. Smith et al. [2004] concluded that the positive and negative NBEs occurred in a clear separate altitude region in a cloud with positive NBEs between 7-15 km and negative NBEs between 15-20 km.

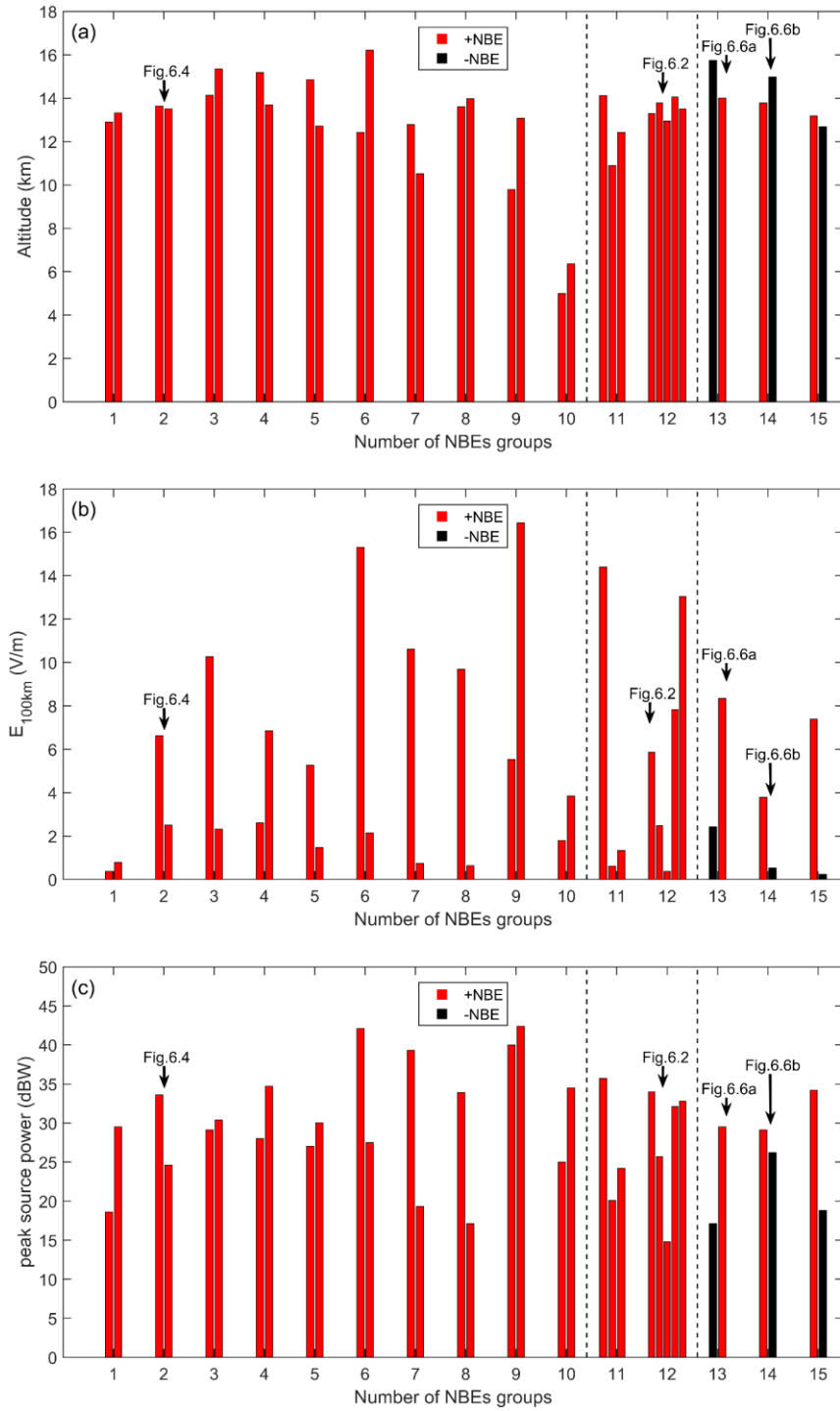


Figure 6.1. Bar chart of: (a) altitude, (b) range-normalized (100 km) FA amplitude, (c) VHF powers for NBEs in groups. The x-axis shows the NBE group number. Groups 1 - 10 each have a pair of positive NBE, Groups 11 and 12 have 3 and 5 positive NBEs, and Groups 13 - 15 have 2 NBEs with opposite polarities.

Similarly, Wu et al. [2012] stated that negative NBE mostly occurred between 16 - 19 km altitude and positive NBEs can occur in a wide range of altitudes, mostly 7-16 km. The altitudes of the 34 NBEs in Figure 6.1(a) are in reasonable agreement with previous measurements except for two differences: (i) the NBEs in Group #10 had quite low altitudes for positive NBEs and (2) the separation of NBE polarities by altitude (negative NBEs above positive NBEs) was not observed.

Figure 6.1(b) shows the NBE FA amplitudes range-normalized to 100 km ($E_{100\text{km}}$) for the 15 Groups. $E_{100\text{km}}$ values for all positive NBE ranged from 0.4 to 16.4 Vm^{-1} with an arithmetic mean/standard deviation of $(5.5 \pm 4.8) \text{ Vm}^{-1}$. Our average $E_{100\text{km}}$ value is somewhat smaller than the 8.0 and 11.0 Vm^{-1} averages found by Willett et al. (1989) and Karunarathne et al. (2015), respectively, but we searched for NBEs with large amplitude Log-RF pulses (VHF) while the earlier studies searched for NBEs with large amplitude FA pulses. $E_{100\text{km}}$ values for the three negative NBEs (2.4, 0.5, and 0.2 Vm^{-1}) were substantially smaller than the majority of positive NBEs.

Figure 6.1(c) shows the peak radiated power in dBW for the 15 Groups. VHF radiated powers were estimated using Equation 4.1 in chapter 4. The source powers for 31 positive NBEs ranged from 14.8 – 42.4 dBW (30 – 17,500 W) with arithmetic mean 34.3 dBW (2.7 kW). Peak radiated powers for the three negative NBEs were 17.1, 26.2, 18.8 dBW (51, 420, 76 W).

6.3.2 Time and Horizontal separation of NBEs in groups.

For 10 pairs of positive NBEs (Groups 1-10 in Figure 6.1), the time separation between the positive NBEs varied from 18-476 ms with an arithmetic mean of 136.2 ms. The horizontal distance between the NBEs in these pairs ranged between 0.6 and 6.5 km with an arithmetic mean of 3.6 km. The time separations between successive positive NBEs in Group 11 were 52.0 ms and 125.0 ms, while their horizontal distance separations were 4.6 and 2.9 km, respectively. For Group 12 (5 positive NBEs), time separations between successive positive NBEs were 145.8, 222.4, 75.8, and 2.4 ms and their horizontal distance separations were 8.4, 5.6, 3.5, and 3.6 km, respectively. For Groups 13-15 the time intervals between the positive and negative NBEs of each pair were 31.0, 133.6 and 71.1 ms and the horizontal distance separations were 4.7, 6.1 and 1.3 km.

The only previous report of NBE groups (that we know of) is Nag et al. (2010), who found three groups of two NBEs with time intervals between pairs of 43, 66 and 181 ms. The horizontal separation distances were 16, 24 and 11 km, respectively. Note that the separation distances between NBE pairs found in Nag et al. (2010) study were greater than our limit of proximity defined within the NBE pairs (10 km).

6.3.3 Spatiotemporal relation with other lightning activities.

The NBEs groups can be either isolated or not-isolated (associated with other lightning activities). Similar to the definition of an isolated NBE, we defined an NBE group as isolated if no other detectable lightning events occurred within a 10 km radius and a time interval of ± 660 ms from the 1st NBE of the group.

Among our 10 pairs of positive NBEs (Groups 1-10 in Figure 6.1), 7 groups were identified as isolated events. The 3 not-isolated pairs can be described as follows.

One pair was followed by intracloud lightning activities. Another pair occurred during a single return stroke, negative CG flash; the first NBE of the pair occurred 141 ms and 4.5 km horizontally before the return stroke while second NBE occurred 5.8 ms and 9.4 km horizontally after the return stroke. The third not-isolated pair occurred after a three-stroke negative CG flash: the first return stroke of the flash occurred 411 ms and 5.6 km horizontally prior to the first NBE of the pair.

The triplet of positive NBEs (Group 11 in Figure 6.1) was not isolated since it was followed by a three-stroke negative CG flash. First two NBEs of the triplet occurred before the 1st return stroke, respectively, 202.0 ms, 150.0 ms and 2.5 km, 5.8 km horizontally from the first return stroke. 3rd NBE was embedded in the sequence of IB pulses 25 ms before and 3.2 km from the first return stroke of the CG flash.

Three pairs of NBE with mixed NBE polarity were found. One mixed group (#15 in Figure 6.1) was an isolated event with a positive initial NBE followed by a substantially weaker negative NBE. Other two mixed polarity pairs are shown in figure 6.3. These 2 pairs could not be identified as an isolated or not-isolated event since lightning activities around a time interval of ± 660 ms from the NBE event did not trigger enough sensors to locate the pulses.

Figure 6.2 shows the detailed data for Group 12 in Figure 6.1. This group had six positive NBEs, but only 5 of the NBEs could be located (labeled NBE-1 to NBE-5). Figure 6.2(a) shows 1.8 s of FA and Log-RF data from nearby EE2 sensors along with altitudes of lightning events determined from $\int dE/dt$ represented by light and dark green dots (right axis). All events within 10 km of the NBE-1 (see figure) are indicated in dark green color, so all light green events are more than 10 km horizontally from the NBE-1. Locations of NBEs are indicated by black circles while locations of return strokes are marked with triangles.

The flash begins with seven-stroke negative CG flash, and 1st stroke happened before 1040 ms and 6.9 km horizontally from the NBE-1 while the time and horizontal distance separation for closest (in time) return stroke (last dark green triangle) from NBE-1 were, respectively, 703 ms and 6.5 km. (Note that based on NBE-1 rather than NBE-0, the last located event of the CG flash was not within 660 ms.)

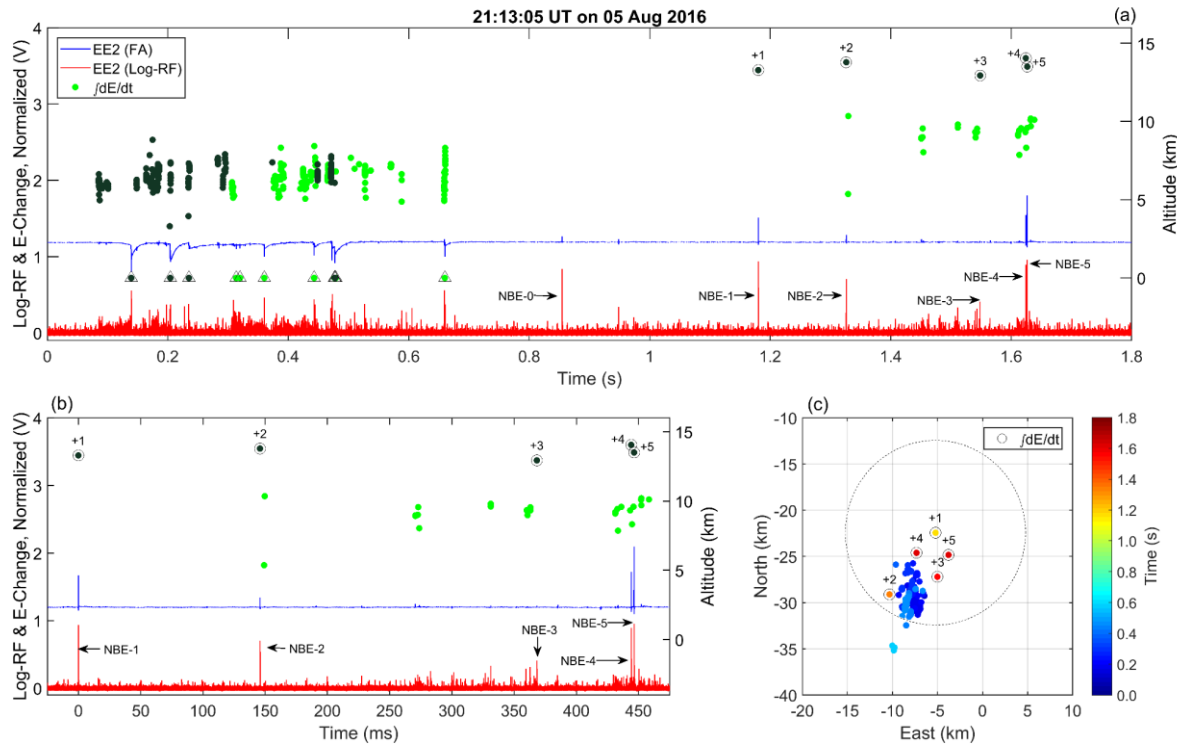


Figure 6.2. Example of a multiple positive NBE discharge event (Group 12). The FA data and Log-RF data are both shown as normalized voltages. (a) An overview is showing 1.8 s of FA data (blue) and Log-RF data (red) including six positive NBEs (NBE-0 to NBE-5). Light and dark green dots represent altitudes (right-hand vertical scale) of FA pulses determined using $\int dE/dt$. All events within 10 km of NBE-1 are marked with dark green dots. Triangles indicate the locations of return strokes. Each NBE location is marked with a small circle. (b) Expanded view (500 ms) of (a) showing NBEs. (c) Plan view of lightning event locations near NBE-1. Locations are color-coded according to their appearance time. NBE-1 is at the center of the 10 km ring.

Figure 6.2(b) is an expanded view of the 500 ms of electrical activity including NBE-1 through NBE-5. It is easy to see that each NBE had a substantial pulse in FA data coincident with a substantial Log-RF pulse (with NBE-3 being the weakest at 14.8 dBW or 30 W). Altitudes of 5 NBEs were, respectively, 13.3, 13.8, 12.9, 14.1 and 13.5 km, so each NBE occurred at roughly the same height. Figure 6.2 (c) shows the plan position 1.8 s of lightning activity (within 10 km of NBE-1, indicated by a black dotted circle). A small black circle indicates the X-Y location of each NBE and each number near the NBE location represents the discharge sequence. The time of each event is color coded with early events blue and late events red (see the color bar).

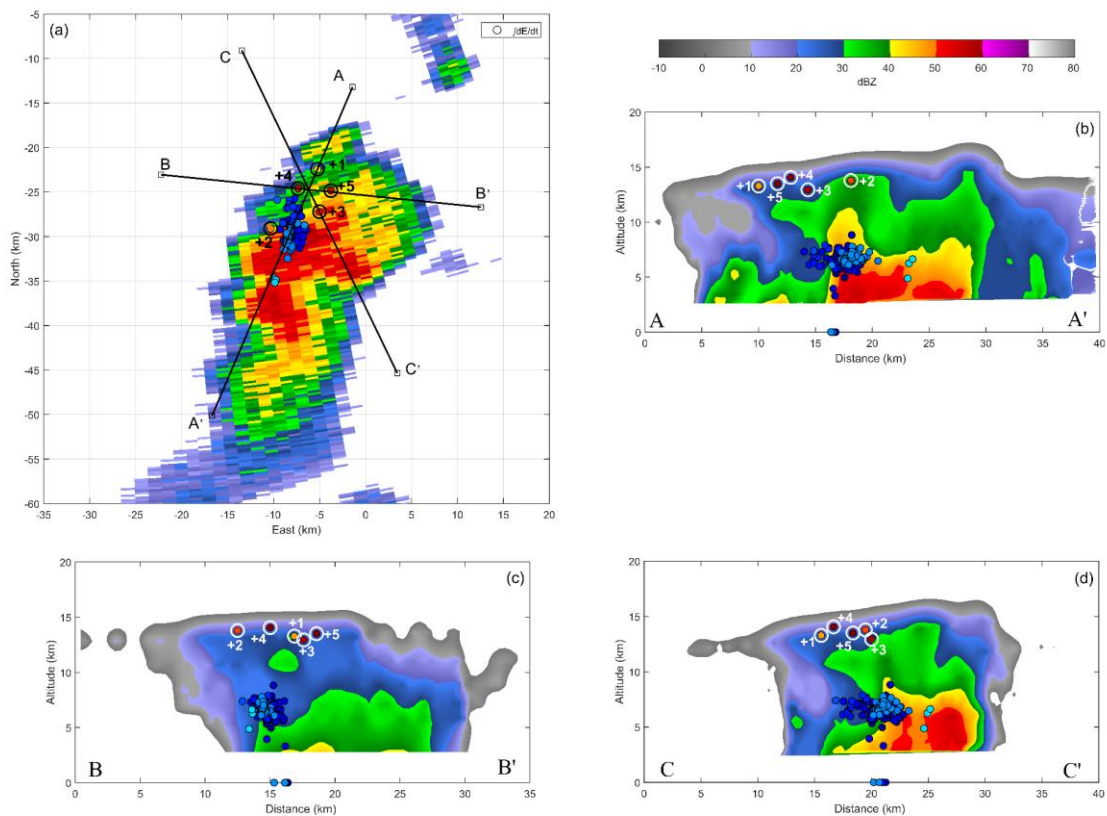


Figure 6.3. Radar reflectivity along with the five positive NBEs of Group 12 (shown in Figure 6.2). (a) Location of NBEs (numbered black circles) superimposed on PPI radar scan at 3.4° elevation angle. The other lightning events (dots) on the PPI scan are color-coded by time as in Figure 6.2 (c). Lines A-A', B-B', and C-C' show the plan view locations of the vertical radar cross-sections shown (b), (c), and (d). Panels (b), (c) and (d): Vertical radar cross-sections along the line segments of A-A', B-B', and C-C', respectively, with lightning events superimposed and NBEs shown as numbered white circles.

Figure 6.3 shows radar reflectivity data associated with the 5-NBE group (Group 12, Figure 6.1) just discussed. The positive NBEs occurred within 30 km of the EE sensor site and had location errors of $dx \leq 70$ m, $dy \leq 170$ m, and $dz \leq 250$ m. Figure 6.3(a) shows horizontal locations of all NBEs, as well as the location of other lightning events superimposed on the PPI radar reflectivity scan. The radar elevation angle of PPI scan was 3.4° . Vertical radar cross sections are shown in Figures 6.3(b), 6.3(c), and 6.3(d), respectively. Each NBE is shown as a numbered black circle. Approximate height of the cloud was 14-16 km while the altitudes of NBEs were respectively, 13.3, 13.8, 12.9, 14.1, and 13.5. All positive NBEs occurred at the upper part of the cloud while the other located lightning events of the negative CG flash happened below 8 km altitude in or near the high reflectivity storm core.

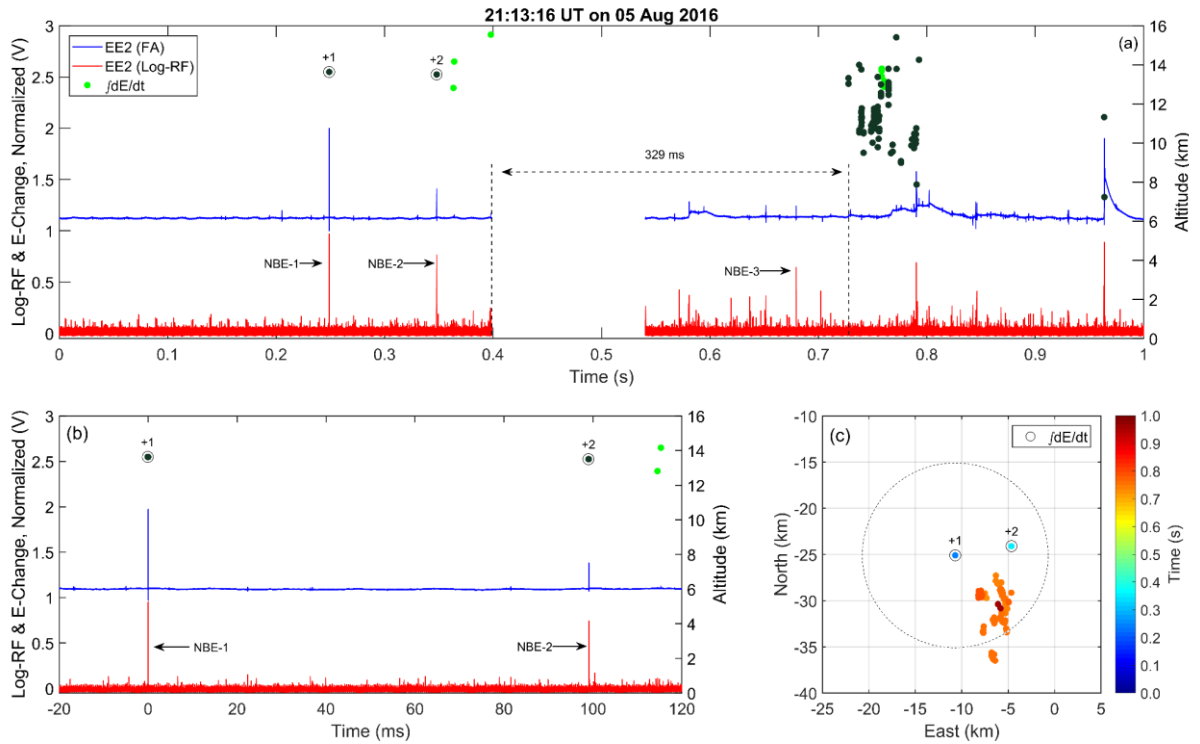


Figure 6.4. Figure format similar to that of Figure 6.2, shows an additional example of multiple positive NBEs discharge events. This example has three positive NBEs.

Figure 6.4 shows another example of a not-isolated group of positive NBEs; the group is followed by an IC flash. This example had three positive NBEs, but only two of them were located. These 3 NBEs occurred 10 seconds after the group of NBEs shown in Figures 6.2 and 6.3. Figures 6.4(a), 6.4(b), and 6.4(c) are similar to corresponding parts of Figure 6.2. The separation time between NBE-1 and NBE-2 was 99 ms, while their horizontal separation was 6.1 km. The IC flash followed the positive NBEs within 479 ms and 5 km horizontally (dark green dots). The 329 ms period indicated by two horizontal lines in Figure 6.4(a) included a time without a trigger and another part in which there were not enough FA or dE / dt data to determine event locations.

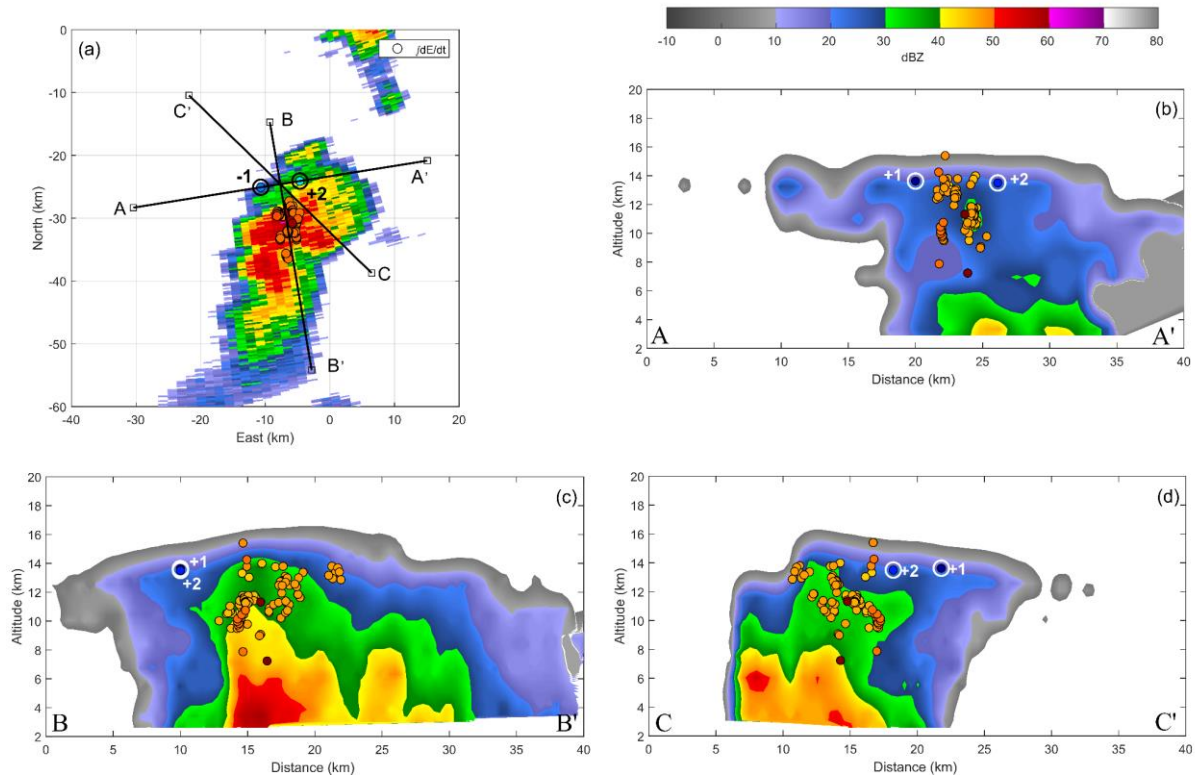


Figure 6.5. Radar reflectivity scan and the vertical cross sections of the volumetric radar data for three sequences of NBE discharge events in Figure 6.4. The format of the figure is similar to that of Figure 6.3.

Figure 6.5 shows radar reflectivity data similar to the data shown in Figure 6.3 but representing the NBE group data just discussed and shown in Figure 6.4. The positive NBEs occurred within 30 km of the EE sensor site and had location errors of $dx \leq 70$ m, $dy \leq 170$ m, and $dz \leq 250$ m. The NBE groups shown in Figures 6.3 and 6.5 use the same radar data, since the groups were separated by only 10 seconds.

Figure 6.5(a) shows that the two located positive NBEs were north of the IC flash that followed them, while Figures 6.5(b), (c), (d) show that the IC flash extended up to and above the 2 NBEs, but no located IC flash events moved as far north as the NBEs. Approximate cloud boundary was at 14-16 km. The NBEs occurred in the downshear anvil while the IC flash occurred primarily above the reflectivity core.

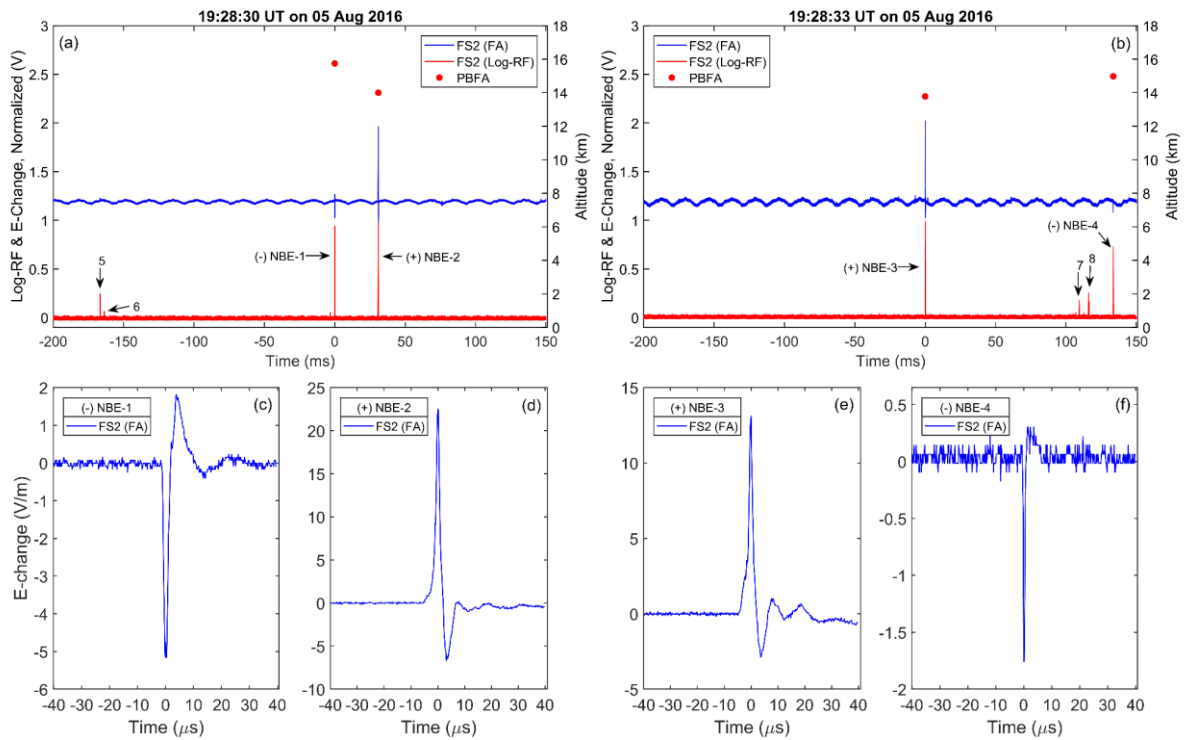


Figure 6.6. Examples of mixed polarity pairs of NBEs. (a) Overview of 350 ms of Group 13 showing FA and Log-RF data for a negative NBE followed by positive NBE; expanded FA waveforms (80 μ s) of these NBEs are shown in (c) and (d). (b) Overview of 350 ms of FA and Log-RF data for another mixed pair of NBEs (Group 14) with the first NBE positive; expanded FA waveforms (80 μ s) of these two NBEs are shown in (e) and (f).

Figure 6.6 shows two examples of mixed polarity NBE groups (#13 and #14); these groups were isolated. Note that these groups were separated by only 3 s, so we discuss them together. The altitudes of the pulses (right axis) were determined from the PBFA method (red dots). In Figure 6.6(a) NBE-1 and NBE-2 occurred 3.5 seconds before the NBE-3 and NBE-4 in Figure 6.6(b). (The additional Log-RF pulses indicated by 5 and 6 in Figure 6.6(a) and 7 and 8 in Figure 6.6(b) could be weaker positive NBEs, but we could not determine their locations.) In Figure 6.6(a), the first event of the pair was negative NBE, and its FA waveform is shown in Figure 6.6(c) while the FA waveform of positive NBE within the pair shown in Figure 6.6(d). Figure 6.6(b) is similar to Figure 6.6(a) except the initial event of the pair was a positive NBE. The horizontal distance from the positive NBE to negative NBE was 6.1km and time difference within the pair was 133.6 ms: their FA waveforms are shown in Figures 6.6(e) and 6.6(f).

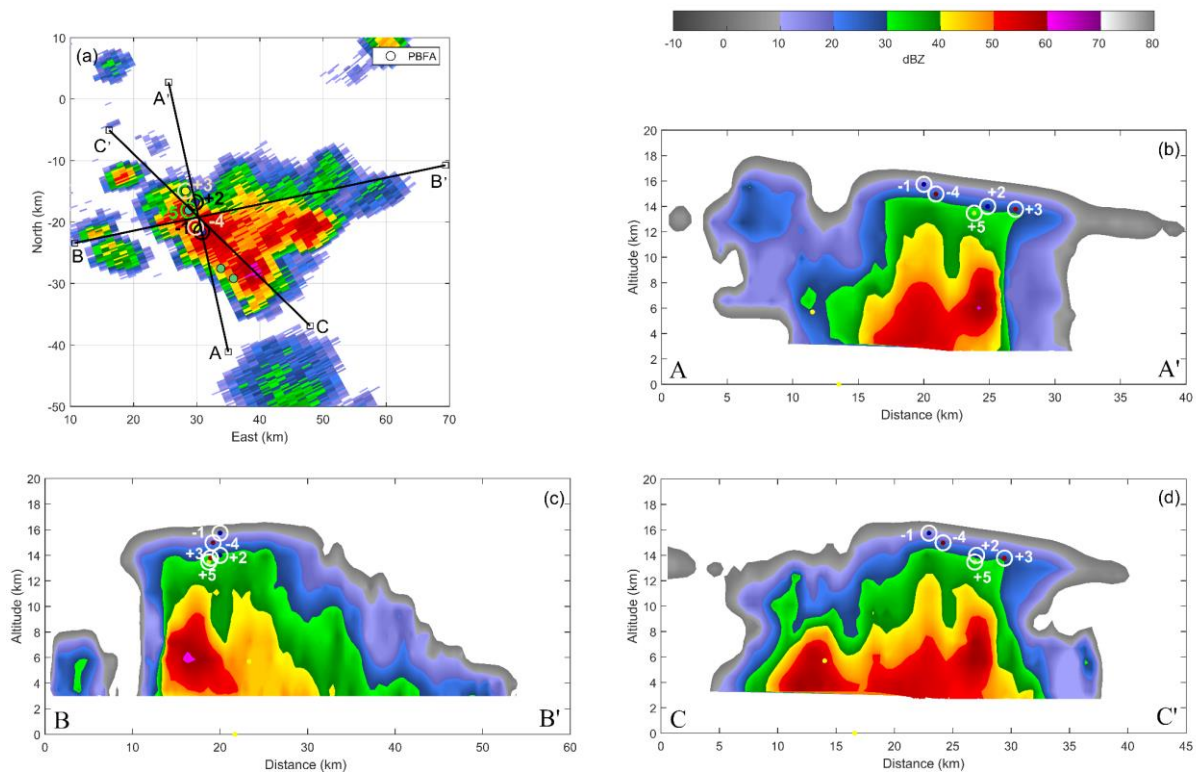


Figure 6.7. Similar to Figure 6.3, showing radar reflectivity data for two pairs of NBE discharge events with opposite polarity within the pair, as shown in Figure 6.6.

Figure 6.7 shows radar reflectivity data similar to the data shown in Figure 6.3, but representing the two isolated NBE groups just discussed and shown in Figure 6.6. The radar elevation angle of PPI scan was 3.4° . The positive NBEs occurred within 20 km of the EE sensor site and had location errors of $dx \leq 650$ m, $dy \leq 480$ m, and $dz \leq 380$ m. Note that a fifth positive NBE is included and marked as NBE #5; this NBE occurred during the 3 s period that separated the two NBE groups. Figures 6.7(b), (d) indicate that the 2 negative NBEs were higher than the 3 positive NBEs and occurred above a slightly higher reflectivity core (indicated by the 40 dBZ contour) than the positive NBEs, which were above a different reflectivity core.

6.4 Summary and Conclusions.

We have analyzed 34 of NBEs that occurred in 15 groups; 31 NBEs were positive NBEs and 3 were negative NBEs. By our definition a NBE group occurred when an NBE was followed by one or more NBEs within a 10 km radius and a ± 660 ms time interval from the first NBE. For positive NBEs only, we found 10 doublets, a triplet, and a quintuplet; in addition there were 3 pairs with a positive NBE and a negative polarity NBE. The majority of the NBE groups occurred as isolated events at high altitudes.

In Chapter 5, we found that the time separations between the initiating positive NBE (INBE) and the first IB pulse of the following IC flash varied from 0.2 to 6.7 ms with an average of 2.1 ms. For the 15 Groups NBEs (Figure 6.1), the time separations between successive NBEs were > 18 ms and averaged 94 ms (with one exception of 2.4 ms). Thus, the time separations between the successive NBEs seem too long for the first NBE to have initiated the following NBE. In other words, these data suggest that all (or possibly all but one) of the NBEs in the Groups were initiated independently.

As discussed above, Karunarathna et al. (2015) studied the locations of 172 positive NBEs in the radar structure of Florida thunderstorm; they noted that some of the 172 NBEs occurred at places in the thundercloud where the expected polarity of the large-scale cloud electric field could not have initiated them. Karunarathna et al. (2015) cited evidence suggesting that complex updrafts and downdrafts existed in, above, and around the thunderstorm core and caused turbulent motions on many scales; they also cited evidence that buoyant dynamics in anvil clouds also made these cloud regions turbulent. Karunarathna et al. (2015) suggested that turbulent motions could “stir, fold, and invert” adjacent, oppositely charged regions in the clouds, thereby producing small-scale regions with electric fields with opposite polarity from “expected,” thereby explaining the unexpected initiation of positive NBEs and negative NBEs. The conclusion of the previous paragraph of the independent initiation of NBEs in the 15 Groups fits with the observation in Karunarathna et al. (2015) and supports the suggestion that small-scale turbulent motions can be important in initiating NBEs.

CHAPTER 7

SUMMARY

The overall goal of this dissertation has been to investigate Narrow Bipolar Events (NBEs) properties and their relation to initiation of lightning, using data from a lightning sensing array. This task was carried out successfully in four different investigations (Chapters 3,4,5 and 6), and the main findings are the following:

Finding the precise source locations of the lightning pulses was vital part of completing this dissertation. This work has been described in Chapter 3. and some of the key points are,

1. To study lightning initiation and obtain source location of lightning pulse, we deployed an array of sensors at seven sensor sites within 45 km of Oxford, Mississippi. Each station was equipped with four electric field sensors: FA (10 ms decay time), SA (1.0 s decay time)), dE/dt , and Log-RF antenna (bandwidth 187-192 MHz).
2. FA data from at least 5 station were used to obtain the position (t, x, y, z) of lightning pulses using the PBFA (for “position by fast antenna”) method described in Karunarathne et al. (2013).
3. The numerically integrated dE/dt pulses were in good agreement with the waveform of the E -change pulses. Thus, lightning pulses were also located with $\int dE/dt$ waveforms from at least five sensor sites using the PBFA algorithm.
4. There was good agreement between lightning pulse locations determined using E-change data (PBFA) and dE/dt data ($\int dE/dt$). In general, the PBFA locations are slightly more scattered than the $\int dE/dt$ locations.

5. With our sensors, smaller lightning pulses are more easily seen using the integrated dE/dt data than the E-change data.

Data from FAs and Log-RF are used to examine NNBEs. The main focus on the low-altitude (<8.0 km) NNBEs that initiate negative cloud-to-ground (-CG) flashes; very few low-altitude NNBEs have been studied previously. For comparison, 24 high-altitude (>8.0 km) NNBEs are also examined. The low-altitude NNBEs are found to have two types, called NNBE(L) and NNBE(H). This work has been described in Chapter 4 and some of the key points are,

1. Visual inspection of the fast antenna and Log-RF data of 868 -CG flashes with locatable IB pulses showed that, only 33 flashes (4%) were preceded by an event that can be characterized as an NNBE. Thus, 96% of the -CG flashes investigated probably did not begin with an NNBE.
2. The NNBEs that initiated -CG flashes, namely NNBE(L)s and NNBE(H)s, were substantially weaker than NNBE(T)s. They are also much weaker than previously studied positive NBEs that initiated IC flashes. This fact suggests that CG flashes are easier to initiate than IC flashes.

We analyzed 201 positive NBE using data from FA and Log-RF antennas. The dE/dt data in this study was mainly used to locate NBE and other lightning activities. 178 of 201 NBE were classified as Type A-D. 136 of 178 were identified and grouped into INBE, Not-isolated, and isolated group. Based on the E-change, Log-RF waveform and their associated characteristic parameters suggest following results (Chapter 5).

1. Arithmetic mean values of Range-normalized E-change amplitudes for Type A-D of NBEs suggest that Type B NBEs seem to produce large amplitude E-change waveform in contrast to Type C and D.
2. Arithmetic mean values of peak radiated power associated Type A-D of NBEs show that Type C and D NBEs seem to be the most energetic types of NBE.
3. Peak radiated power comparison among INBE, Not-isolated, and Isolated groups show that, largest peak radiation power of NBEs can be found within INBE and Isolated group with the INBE group showing the largest peak power variation.
4. The relationship between the peak radiation powers and the rise time of the Log-RF waveform show that there was a significant negative correlation for the NBE found in the Type C and INBE group. This relationship is also significant for type C NBE in the INBE group.

It was determined that some positive NBEs occurred in groups, although NBEs are usually reported to occur as a single isolated event or as the initial event in IC flashes (INBEs). We have analyzed 34 of NBEs that occurred in 15 groups; 31 NBEs were positive NBEs and 3 were negative NBEs. This work has been described in Chapter 6 and some of the key points are,

1. Only for positive NBEs, we found that there are 10 doublets, a triplet, and a quintuplet; in addition, there were 3 pairs with a positive polarity NBE and a negative polarity NBE. The majority of the NBE groups occurred as isolated events at high altitudes.
2. Time separations between the initiating positive NBE (INBE) and the first IB pulse of the following IC flash was much shorter compared to the time separations between the successive NBEs in the groups. This fact suggests that all (or possibly all but one) of the NBEs in the Groups were initiated independently.

3. Karunarathna et al. (2015) suggested that turbulent motions could “stir, fold, and invert” adjacent, oppositely charged regions in the clouds, thereby producing small-scale regions with electric fields with opposite polarity from “expected,” thereby explaining the unexpected initiation of positive NBEs and negative NBEs. The independent initiation of NBEs in the 15 Groups fits with the observation in Karunarathna et al. (2015) and supports the suggestion that small-scale turbulent motions can be important in initiating NBEs.
4. Although the times between successive NBEs in the groups was long compared to the time from an INBE to first IB pulse of IC flashes, these times were short compared to the time scale of charging the cloud. This fact also supports the notion of small-scale, large amplitude electric field regions produced by turbulence, especially for the opposite polarity NBE pairs.

BIBLIOGRAPHY

BIBLIOGRAPHY

- Azlinda Ahmad, N., Fernando, M., Baharudin, Z.A., Cooray, V., Ahmad, H., Abdul Malek, Z., 2010. Characteristics of narrow bipolar pulses observed in Malaysia. *J. Atmos. Solar-Terrestrial Phys.* 72, 534–540. <https://doi.org/10.1016/j.jastp.2010.02.006>
- Balanis, C.A., 2005. *Antenna Theory: Analysis and Design*, 3rd. ed. Wiley-Interscience, New York, NY, USA, pp. 92-95.
- Bitzer, P.M., Christian, H.J., Stewart, M., Burchfield, J., Podgorny, S., Corredor, D., Hall, J., Kuznetsov, E., Franklin, V., 2013. Characterization and applications of VLF/LF source locations from lightning using the Huntsville Alabama Marx Meter Array. *J. Geophys. Res. Atmos.* 118, 3120–3138. <https://doi.org/10.1002/jgrd.50271>
- Chapman, R., Marshall, T., Karunarathne, S., Stolzenburg, M., 2017. Initial electric field changes of lightning flashes in two thunderstorms. *J. Geophys. Res.* 122, 3718–3732. <https://doi.org/10.1002/2016JD025859>
- Cooray, V., Lundquist, S., 1985. Characteristics of the radiation fields from lightning in Sri Lanka in the tropics. *J. Geophys. Res.* 90, 6099. <https://doi.org/10.1029/JD090iD04p06099>
- Fisher, R.J., Schnetzer, G.H., Thottappillil, R., Rakov, V.A., Uman, M.A., Goldberg, J.D., 1993. Parameters of triggered-lightning flashes in Florida and Alabama. *J. Geophys. Res.* 98, 22887. <https://doi.org/10.1029/93JD02293>
- Griffiths, R.F., Phelps, C.T., 1976. A model for lightning initiation arising from positive corona streamer development. *J. Geophys. Res.* 81, 3671–3676. <https://doi.org/10.1029/JC081i021p03671>
- Gurevich, a. V., Zybin, K.P., Roussel-Dupre, R.A., 1999. Lightning initiation by simultaneous effect of runaway breakdown and cosmic ray showers. *Phys. Lett. A* 254, 79–87. [https://doi.org/10.1016/S0375-9601\(99\)00091-2](https://doi.org/10.1016/S0375-9601(99)00091-2)
- Gurevich, A. V., Zybin, K.P., 2005. Runaway Breakdown and the Mysteries of Lightning. *Phys. Today* 58, 37–43. <https://doi.org/10.1063/1.1995746>
- Gurevich, A.V., Medvedev, Y.V., Zybin, K.P., 2004. New type discharge generated in thunderclouds by joint action of runaway breakdown and extensive atmospheric shower. *Phys. Lett. A* 329, 348–361. <https://doi.org/10.1016/j.physleta.2004.06.099>
- Gurevich, A.V., Milikh, G.M., Roussel-Dupre, R., 1992. Runaway electron mechanism of air breakdown and preconditioning during a thunderstorm. *Phys. Lett. A* 165, 463–468. [https://doi.org/10.1016/0375-9601\(92\)90348-P](https://doi.org/10.1016/0375-9601(92)90348-P)

- Hamlin, T., 2004. The New Mexico Tech Lightning Mapping Array. PhD dissertation. New Mexico Institute of Mining and Technology, Socorro, NM.
- Hamlin, T., Light, T.E., Shao, X.M., Eack, K.B., Harlin, J.D., 2007. Estimating lightning channel characteristics of positive narrow bipolar events using intrachannel current reflection signatures. *J. Geophys. Res. Atmos.* 112, 1–8. <https://doi.org/10.1029/2007JD008471>
- Jacobson, A.R., Knox, S.O., Franz, R., Enemark, D.C., 1999. FORTE observations of lightning radio-frequency signatures: Capabilities and basic results. *Radio Sci.* <https://doi.org/10.1029/1998RS900043>
- Jacobson, A.R., Light, T.E.L., 2012. Revisiting “Narrow Bipolar Event” intracloud lightning using the FORTE satellite. *Ann. Geophys.* 30, 389–404. <https://doi.org/10.5194/angeo-30-389-2012>
- Jerauld, J.E., 2007. Properties of natural cloud-to-ground lightning inferred from multiple-station measurements of close electric and magnetic fields and field derivatives. PhD dissertation. University of Florida
- Karunarathna, N., Marshall, T.C., Karunarathne, S., Stolzenburg, M., 2017. Initiation locations of lightning flashes relative to radar reflectivity in four small Florida thunderstorms. *J. Geophys. Res. Atmos.* 122, 6565–6591. <https://doi.org/10.1002/2017JD026566>
- Karunarathna, N., Marshall, T.C., Stolzenburg, M., Karunarathne, S., 2015. Narrow bipolar pulse locations compared to thunderstorm radar echo structure. *J. Geophys. Res.* 120, 11,690–11,706. <https://doi.org/10.1002/2015JD023829>
- Karunarathne, S., Marshall, T.C., Stolzenburg, M., Karunarathna, N., 2016. Electrostatic field changes and durations of narrow bipolar events. *J. Geophys. Res.* <https://doi.org/10.1002/2016JD024789>
- Karunarathne, S., Marshall, T.C., Stolzenburg, M., Karunarathna, N., 2015. Observations of positive narrow bipolar pulses. *J. Geophys. Res.* 120, 7128–7143. <https://doi.org/10.1002/2015JD023150>
- Karunarathne, S., Marshall, T.C., Stolzenburg, M., Karunarathna, N., Vickers, L.E., Warner, T.A., Orville, R.E., 2013. Locating initial breakdown pulses using electric field change network. *J. Geophys. Res. Atmos.* 118, 7129–7141. <https://doi.org/10.1002/jgrd.50441>
- Kitagawa, N., Brook, M., 1960. A comparison of intracloud and cloud-to-ground lightning discharges. *J. Geophys. Res.* 65, 1189–1201. <https://doi.org/10.1029/JZ065i004p01189>
- Koshak, W.J., Solakiewicz, R.J., 1996. On the retrieval of lightning radio sources from time-of-arrival data. *J. Geophys. Res. Atmos.* 101, 26631–26639. <https://doi.org/10.1029/96JD01618>
- Krehbiel, P.R., Brook, M., McCrory, R.A., 1979. An analysis of the charge structure of lightning discharges to ground. *J. Geophys. Res.* 84, 2432. <https://doi.org/10.1029/JC084iC05p02432>
- Krider, E.P., Weidman, C.D., LeVine, D.M., 1979. The temporal structure of the HF and VHF radiation Produced by intracloud lightning discharges. *J. Geophys. Res.* 84, 5760. <https://doi.org/10.1029/JC084iC09p05760>

- Le Vine, D.M., 1980. Sources of the strongest RF radiation from lightning. *J. Geophys. Res.* 85, 4091. <https://doi.org/10.1029/JC085iC07p04091>
- Le Vine, D.M., Krider, E.P., 1977. The temporal structure of HF and VHF radiations during Florida lightning return strokes. *Geophys. Res. Lett.* 4, 13–16. <https://doi.org/10.1029/GL004i001p00013>
- Lyu, F., Cummer, S.A., Qin, Z., Chen, M., 2019. Lightning Initiation Processes Imaged With Very High Frequency Broadband Interferometry. *J. Geophys. Res. Atmos.* 2018JD029817. <https://doi.org/10.1029/2018JD029817>
- Marshall, T., Bandara, S., Karunarathne, N., Karunarathne, S., Kolmasova, I., Siedlecki, R., Stolzenburg, M., 2019. A study of lightning flash initiation prior to the first initial breakdown pulse. *Atmos. Res.* 217, 10–23. <https://doi.org/10.1016/j.atmosres.2018.10.013>
- Marshall, T., Schulz, W., Karunarathna, N., Karunarathne, S., Stolzenburg, M., Vergeiner, C., Warner, T., 2014. On the percentage of lightning flashes that begin with initial breakdown pulses. *J. Geophys. Res. Atmos.* 119, 445–460. <https://doi.org/10.1002/2013JD020854>
- Marshall, T., Stolzenburg, M., Karunarathna, N., Karunarathne, S., 2014. Electromagnetic activity before initial breakdown pulses of lightning. *J. Geophys. Res. Atmos.* 119, 12,558–12,574. <https://doi.org/10.1002/2014JD022155>
- Medelius, P., M. Thomson, E., S. Pierce, J., 1991. E and DE/DT waveshapes for narrow bipolar pulses in intracloud lightning.
- Nag, A., Rakov, V.A., Tsalikis, D., Cramer, J.A., 2010. On phenomenology of compact intracloud lightning discharges. *J. Geophys. Res.* 115, D14115. <https://doi.org/10.1029/2009JD012957>
- Phelps, C.T., 1971. Field-enhanced propagation of corona streamers. *J. Geophys. Res.* 76, 5799–5806. <https://doi.org/10.1029/JC076i024p05799>
- Phelps, C.T., 1974. Positive streamer system intensification and its possible role in lightning initiation. *J. Atmos. Terr. Phys.* 36, 103–111. [https://doi.org/10.1016/0021-9169\(74\)90070-1](https://doi.org/10.1016/0021-9169(74)90070-1)
- Proctor, D.E., 1971. A hyperbolic system for obtaining VHF radio pictures of lightning. *J. Geophys. Res.* 76, 1478–1489. <https://doi.org/10.1029/JC076i006p01478>
- Rakov, V.A., Uman, M.A., Jordan, D.M., Priore, C.A., 1990. Ratio of leader to return stroke electric field change for first and subsequent lightning strokes. *J. Geophys. Res.* 95, 16579. <https://doi.org/10.1029/JD095iD10p16579>
- Rakov, V.A., Uman, M.A., Thottappillil, R., 1994. Review of lightning properties from electric field and TV observations. *J. Geophys. Res.* 99, 10745. <https://doi.org/10.1029/93JD01205>
- Rison, W., Krehbiel, P.R., Stock, M.G., Edens, H.E., Shao, X.M., Thomas, R.J., Stanley, M.A., Zhang, Y., 2016. Observations of narrow bipolar events reveal how lightning is initiated in thunderstorms. *Nat. Commun.* 7, 1–12. <https://doi.org/10.1038/ncomms10721>
- Rison, W., Thomas, R.J., Krehbiel, P.R., Hamlin, T., Harlin, J., 1999. A GPS-based three-dimensional lightning mapping system: Initial observations in central New Mexico. *Geophys. Res. Lett.* 26, 3573–3576. <https://doi.org/10.1029/1999GL010856>

- Shao, X.M., Krehbiel, P.R., 1996. The spatial and temporal development of intracloud lightning. *J. Geophys. Res. Atmos.* 101, 26641–26668. <https://doi.org/10.1029/96JD01803>
- Shao, X.M., Stanley, M., Regan, A., Harlin, J., Pongratz, M., Stock, M., 2006. Total lightning observations with the new and improved Los Alamos Sferic Array (LASA). *J. Atmos. Ocean. Technol.* 23, 1273–1288. <https://doi.org/10.1175/JTECH1908.1>
- Smith, D.A., Eack, K.B., Harlin, J., Heavner, M.J., Jacobson, A.R., Massey, R.S., Shao, X.M., Wiens, K.C., 2002. The Los Alamos sferic array: A research tool for lightning investigations. *J. Geophys. Res. Atmos.* 107, 1–15. <https://doi.org/10.1029/2001JD000502>
- Smith, D.A., Heavner, M.J., Jacobson, A.R., Shao, X.M., Massey, R.S., Sheldon, R.J., Wiens, K.C., 2004. A method for determining intracloud lightning and ionospheric heights from VLF/LF electric field records. *Radio Sci.* 39, n/a-n/a. <https://doi.org/10.1029/2002RS002790>
- Smith, D.A., Shao, X.M., Holden, D.N., Rhodes, C.T., Brook, M., Krehbiel, P.R., Stanley, M., Rison, W., Thomas, R.J., 1999. A distinct class of isolated intracloud lightning discharges and their associated radio emissions. *J. Geophys. Res. Atmos.* 104, 4189–4212. <https://doi.org/10.1029/1998JD200045>
- Stolzenburg, M., Marshall, T.C., Rust, W.D., Bruning, E., MacGorman, D.R., Hamlin, T., 2007. Electric field values observed near lightning flash initiations. *Geophys. Res. Lett.* 34, L04804. <https://doi.org/10.1029/2006GL028777>
- Stutzman, W.L., Thiele, G.A., 2013. *Antenna theory and design*, 3rd. ed. John Wiley & Sons, pp. 113–114.
- Suszcynsky, D.M., Heavner, M.J., 2003. Narrow Bipolar Events as indicators of thunderstorm convective strength. *Geophys. Res. Lett.* 30, 1–4. <https://doi.org/10.1029/2003GL017834>
- Taylor, W.L., 1978. A VHF technique for space-time mapping of lightning discharge processes. *J. Geophys. Res.* 83, 3575. <https://doi.org/10.1029/JC083iC07p03575>
- Thomas, R.J., Krehbiel, P.R., Rison, W., Hamlin, T., Harlin, J., Shown, D., 2001. Observations of VHF source powers radiated by lightning. *Geophys. Res. Lett.* 28, 143–146. <https://doi.org/10.1029/2000GL011464>
- Uman, M.A., McLain, D.K., Krider, E.P., 1975. The electromagnetic radiation from a finite antenna. *Am. J. Phys.* 43, 33–38. <https://doi.org/10.1119/1.10027>
- Weidman, C.D., Krider, E.P., 1979. The radiation field wave forms produced by intracloud lightning discharge processes. *J. Geophys. Res.* 84, 3159. <https://doi.org/10.1029/JC084iC06p03159>
- Weidman, C.D., Krider, E.P., 1980. Submicrosecond risetimes in lightning return-stroke fields. *Geophys. Res. Lett.* 7, 955–958. <https://doi.org/10.1029/GL007i011p00955>
- Wiens, K.C., Hamlin, T., Harlin, J., Suszcynsky, D.M., 2008. Relationships among Narrow Bipolar Events, “total” lightning, and radar-inferred convective strength in Great Plains thunderstorms. *J. Geophys. Res. Atmos.* 113, 1–31. <https://doi.org/10.1029/2007JD009400>

- Willett, J.C., Bailey, J.C., Krider, E.P., 1989. A class of unusual lightning electric field waveforms with very strong high-frequency radiation. *J. Geophys. Res.* 94, 16255. <https://doi.org/10.1029/JD094iD13p16255>
- Wu, T., Dong, W., Zhang, Y., Funaki, T., Yoshida, S., Morimoto, T., Ushio, T., Kawasaki, Z., 2012. Discharge height of lightning narrow bipolar events. *J. Geophys. Res. Atmos.* 117, n/a-n/a. <https://doi.org/10.1029/2011JD017054>
- Wu, T., Dong, W., Zhang, Y., Wang, T., 2011. Comparison of positive and negative compact intracloud discharges. *J. Geophys. Res.* 116, D03111. <https://doi.org/10.1029/2010JD015233>
- Wu, T., Takayanagi, Y., Yoshida, S., Funaki, T., Ushio, T., Kawasaki, Z., 2013. Spatial relationship between lightning narrow bipolar events and parent thunderstorms as revealed by phased array radar. *Geophys. Res. Lett.* 40, 618–623. <https://doi.org/10.1002/grl.50112>
- Wu, T., Yoshida, S., Ushio, T., Kawasaki, Z., Wang, D., 2014. Lightning-initiator type of narrow bipolar events and their subsequent pulse trains. *J. Geophys. Res. Atmos.* 119, 7425–7438. <https://doi.org/10.1002/2014JD021842>
- Zhang, G., Wang, Y., Qie, X., Zhang, T., Zhao, Y., Li, Y., Cao, D., 2010. Using lightning locating system based on time-of-arrival technique to study three-dimensional lightning discharge processes. *Sci. China Earth Sci.* 53, 591–602. <https://doi.org/10.1007/s11430-009-0116-x>
- Zhu, Y., Rakov, V.A., Tran, M.D., 2016. A study of preliminary breakdown and return stroke processes in high-intensity negative lightning discharges. *Atmosphere (Basel)*. 7. <https://doi.org/10.3390/atmos7100130>

LIST OF APPENDICES

APPENDIX A

CIRCUIT DIAGRAM OF ELECTRIC FIELD DERIVATIVE AND LOG-RF SENSOR.

In this appendix, the circuit diagram of the amplifier used in the dE/dt antenna and the non-inverter level change circuit used in the Log-RF antenna will be shown. The amplifier circuit is necessarily a simple non-inverting circuit that was designed using a high output current LM7171 operational amplifier.

OPA602 and LM741 operational amplifier are the two main component of Non-inverter level change circuit. In operation, the OPA602 serves as an inverting amplifier, while the LM741 only provides constant reference voltage (~ 0.88 V) supply to the non-inverting terminal of the OPA602.

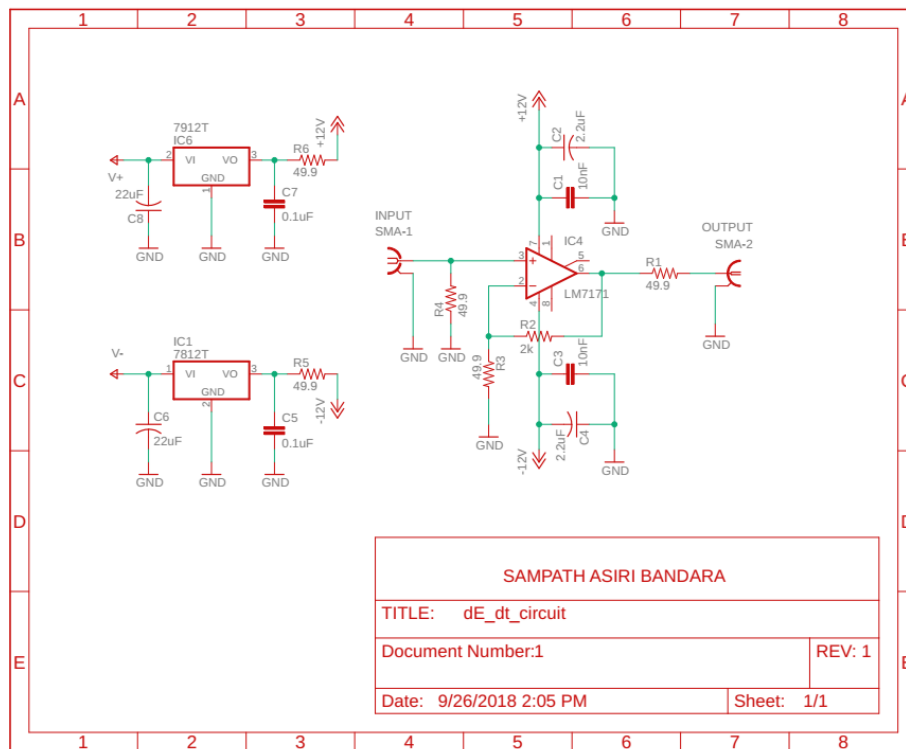


Figure A.1. The circuit diagram of amplifier used in the dE/dt .

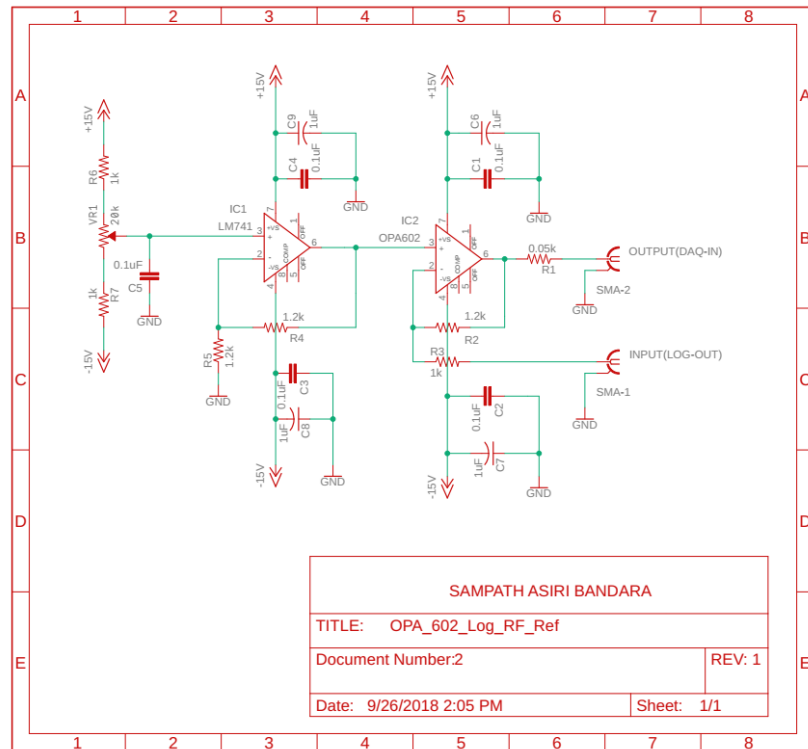


Figure A.2. The schematic of Non-inverter level change circuit.

APPENDIX B

NNBES THAT INITIATE -CG FLASHES: ADDITIONAL EXAMPLES.

The following appendix shows additional examples for negative NBEs that were the initial event of -CG flash. Figure B.1- B.16 shows additional examples for Figure 4.3 & 4.4 in Chapter 4, while Figure B.17- B.29 show further examples for Figure 4.5 & 4.6 in the same chapter.

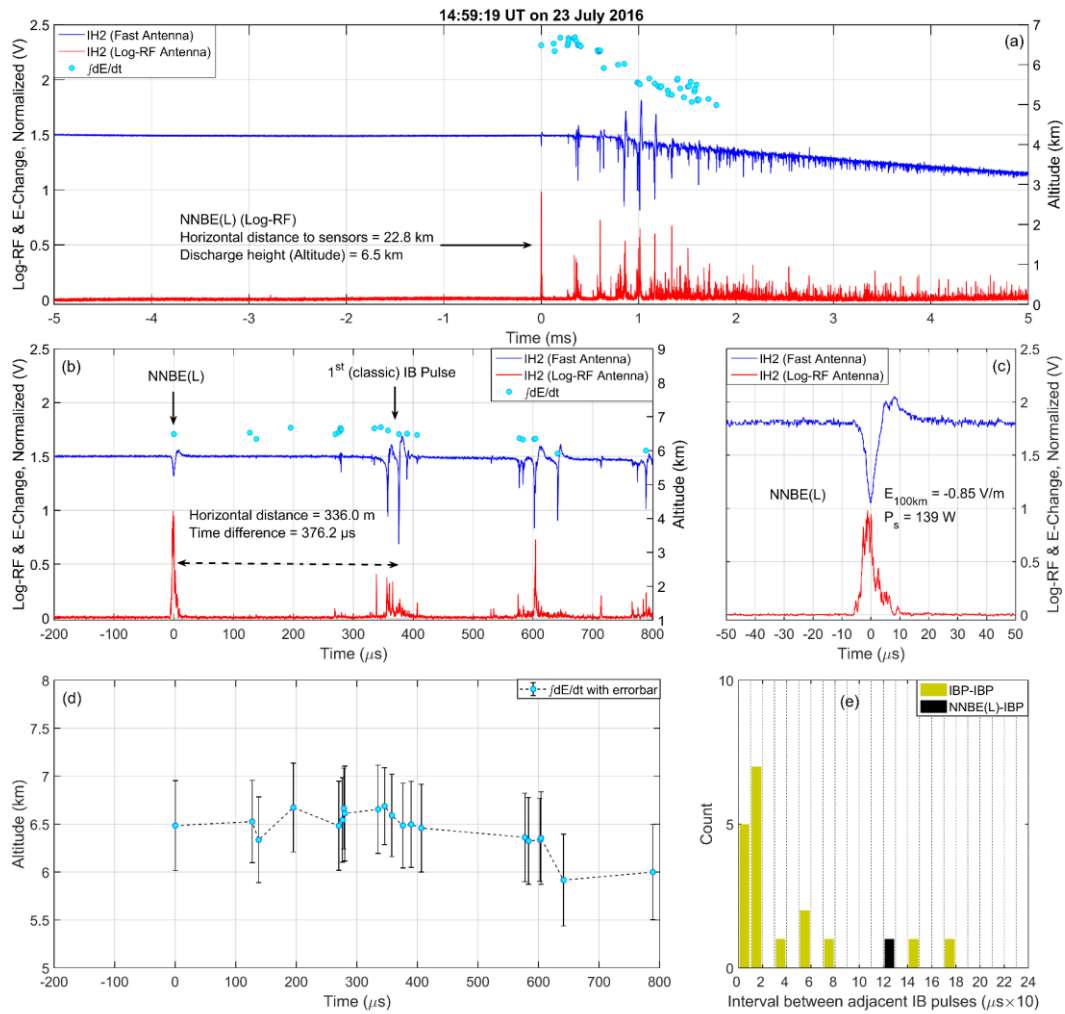


Figure B.1. Example of NNBE(L) occurred as the initial event of a negative CG flash.

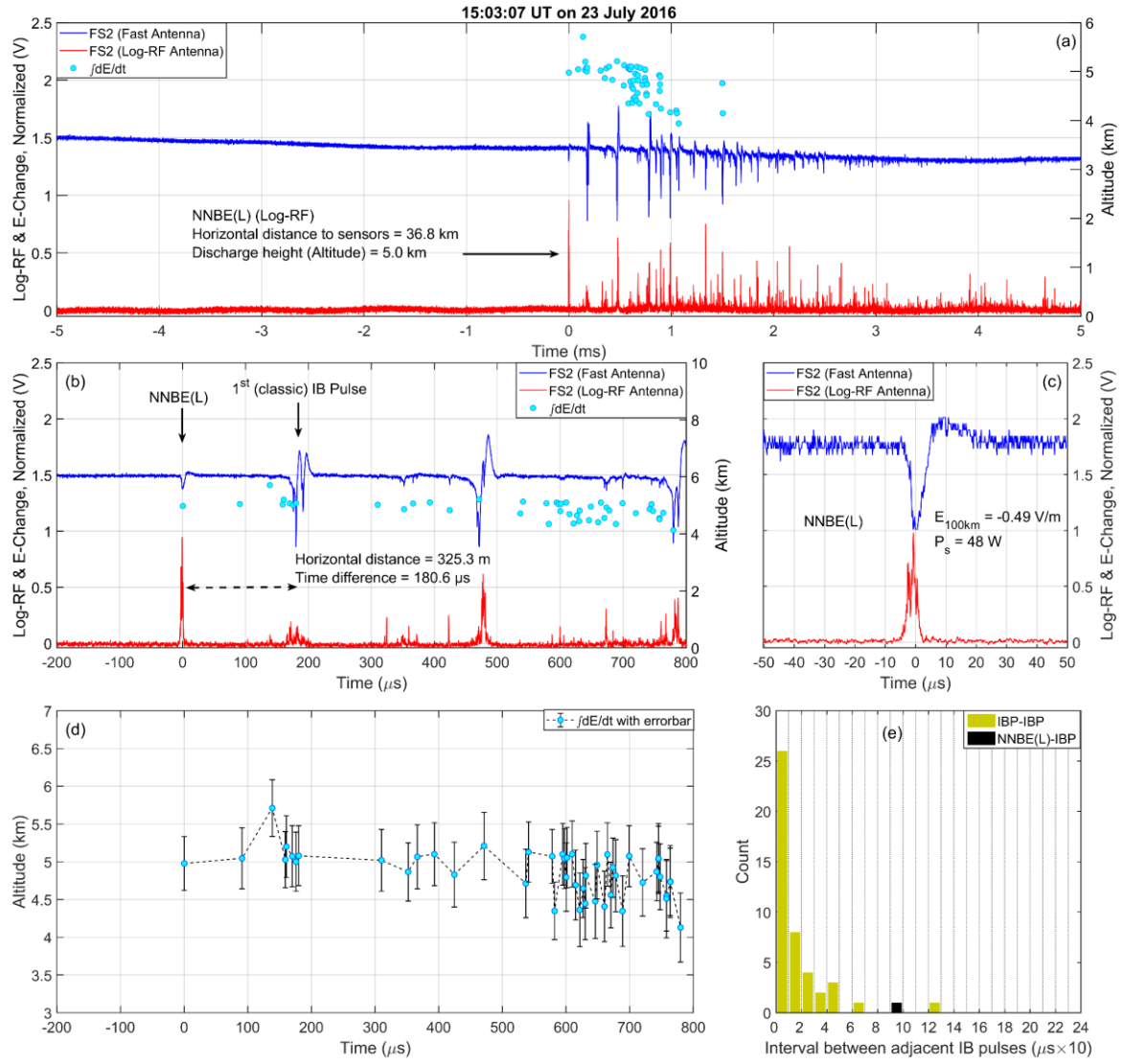


Figure B.2. Example of NNBE(L) occurred as the initial event of a negative CG flash.

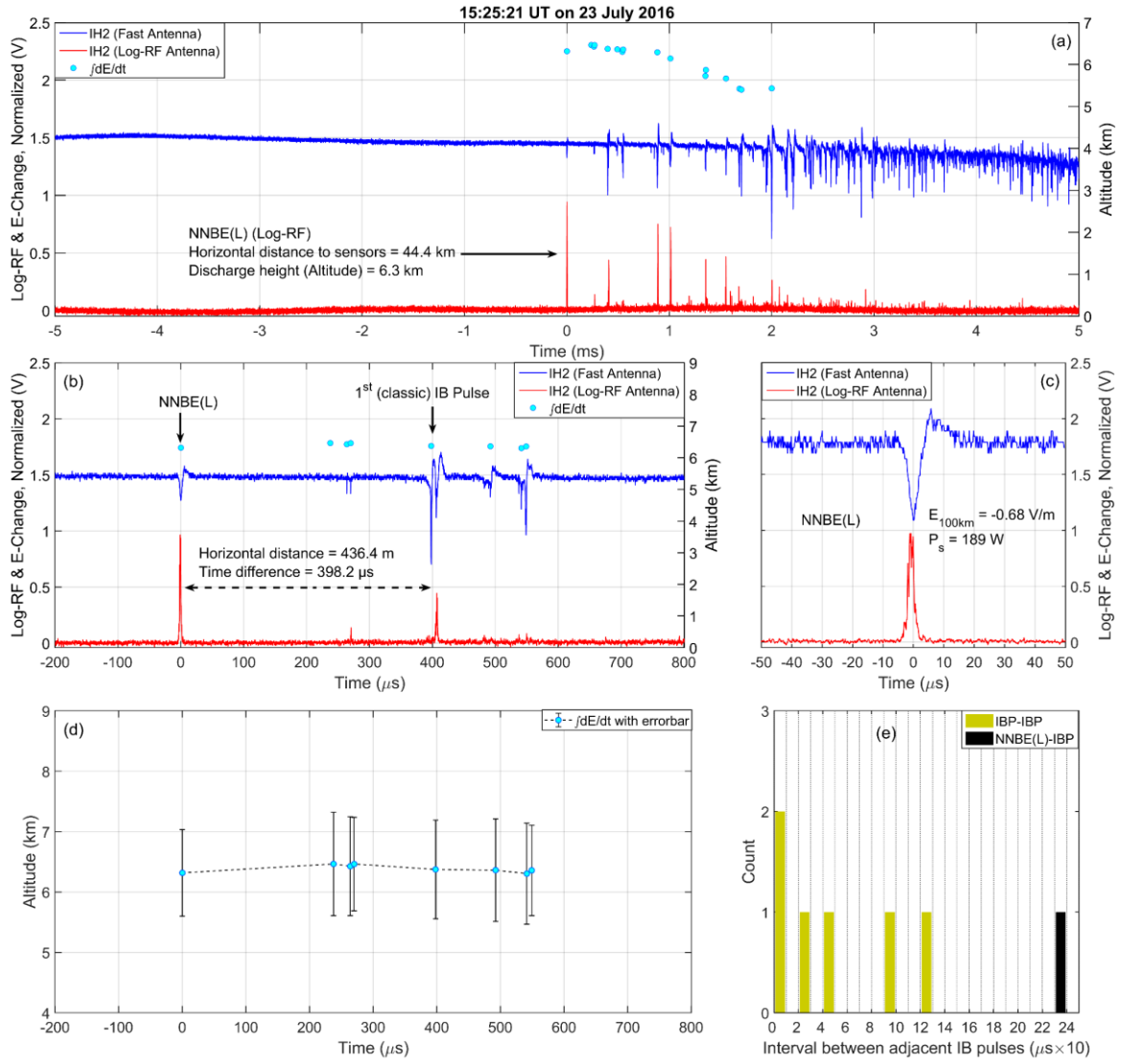


Figure B.3. Example of NNBE(L) occurred as the initial event of a negative CG flash.

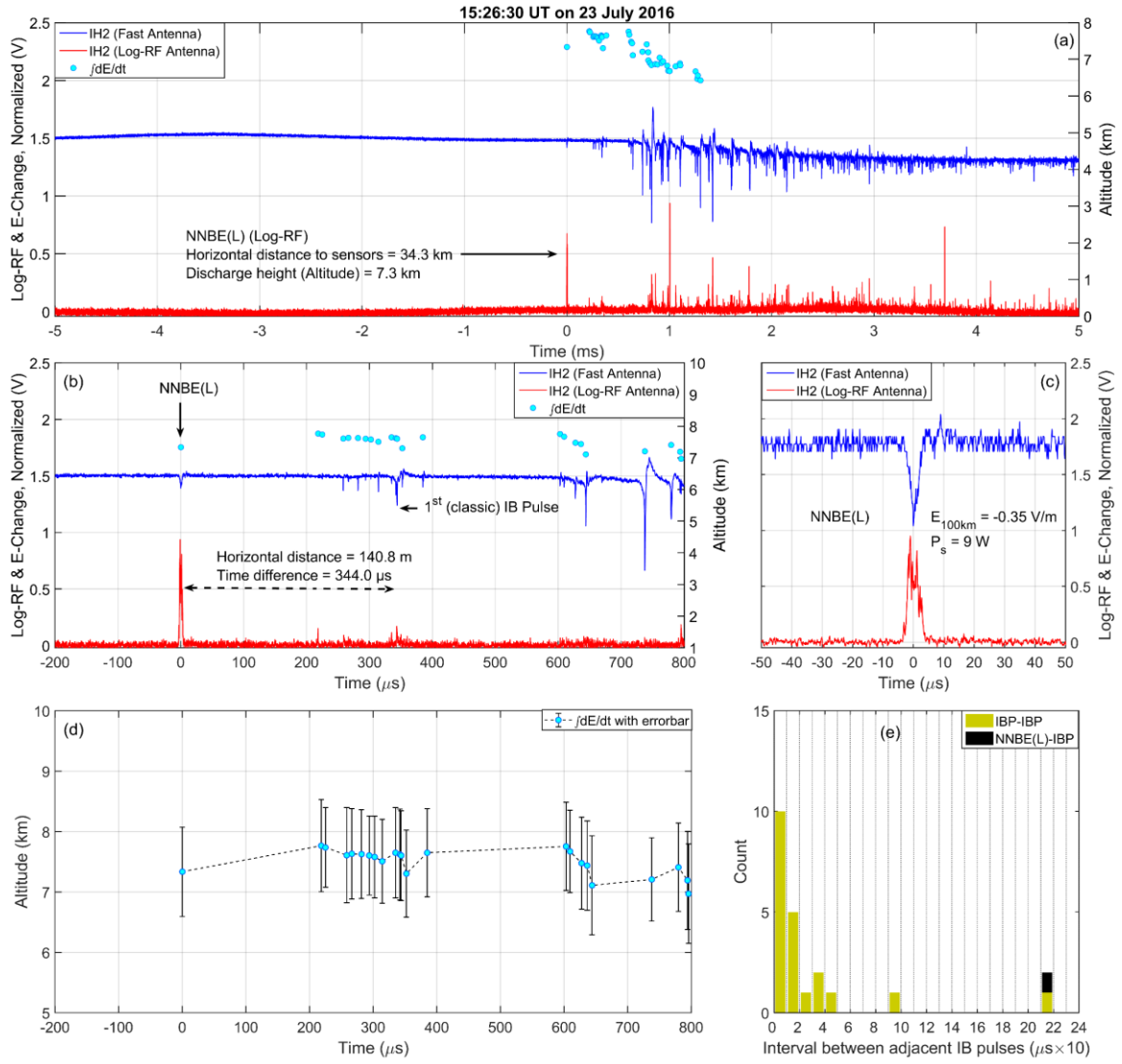


Figure B.4. Example of NNBE(L) occurred as the initial event of a negative CG flash.

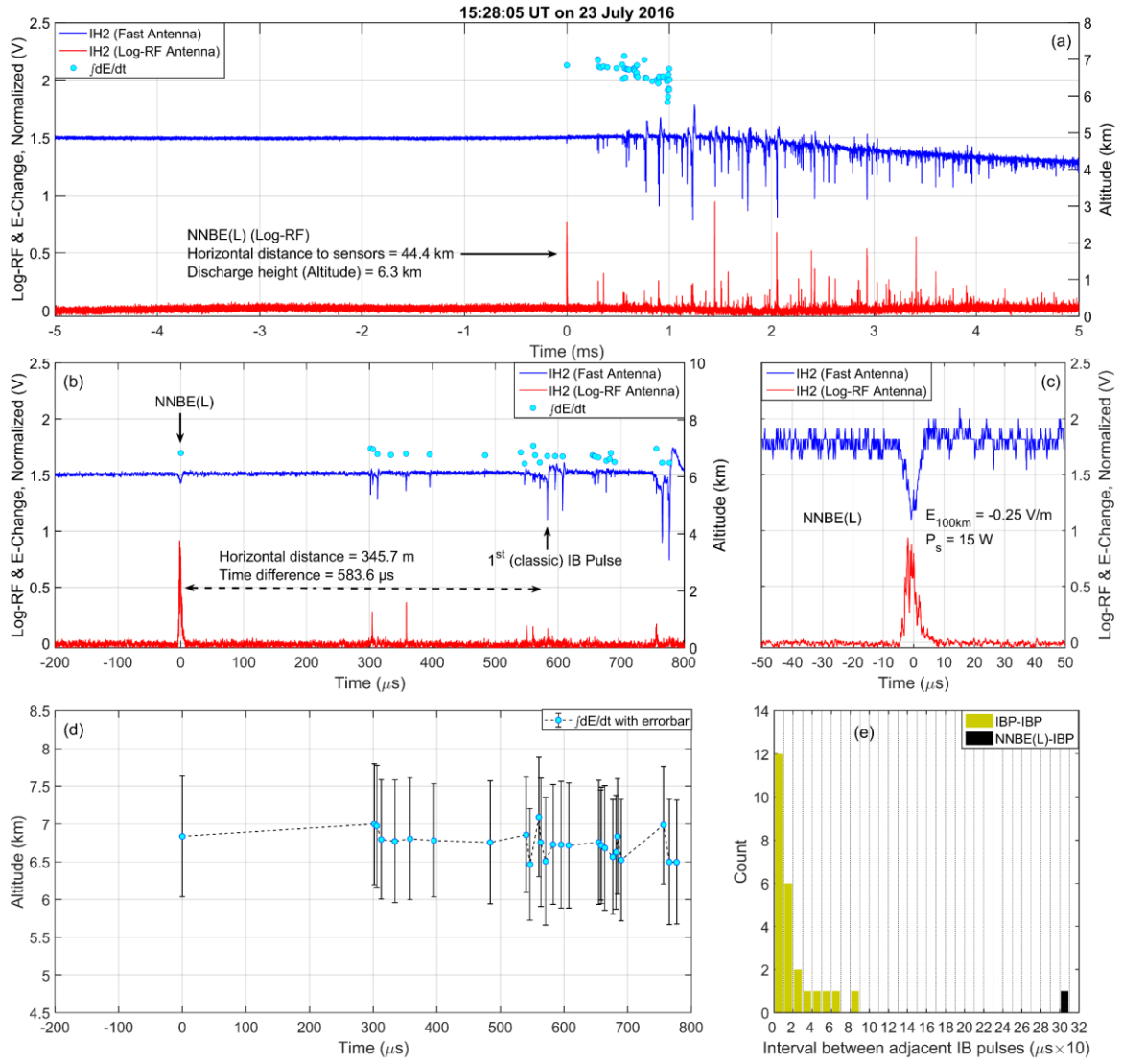


Figure B.5. Example of NNBE(L) occurred as the initial event of a negative CG flash.

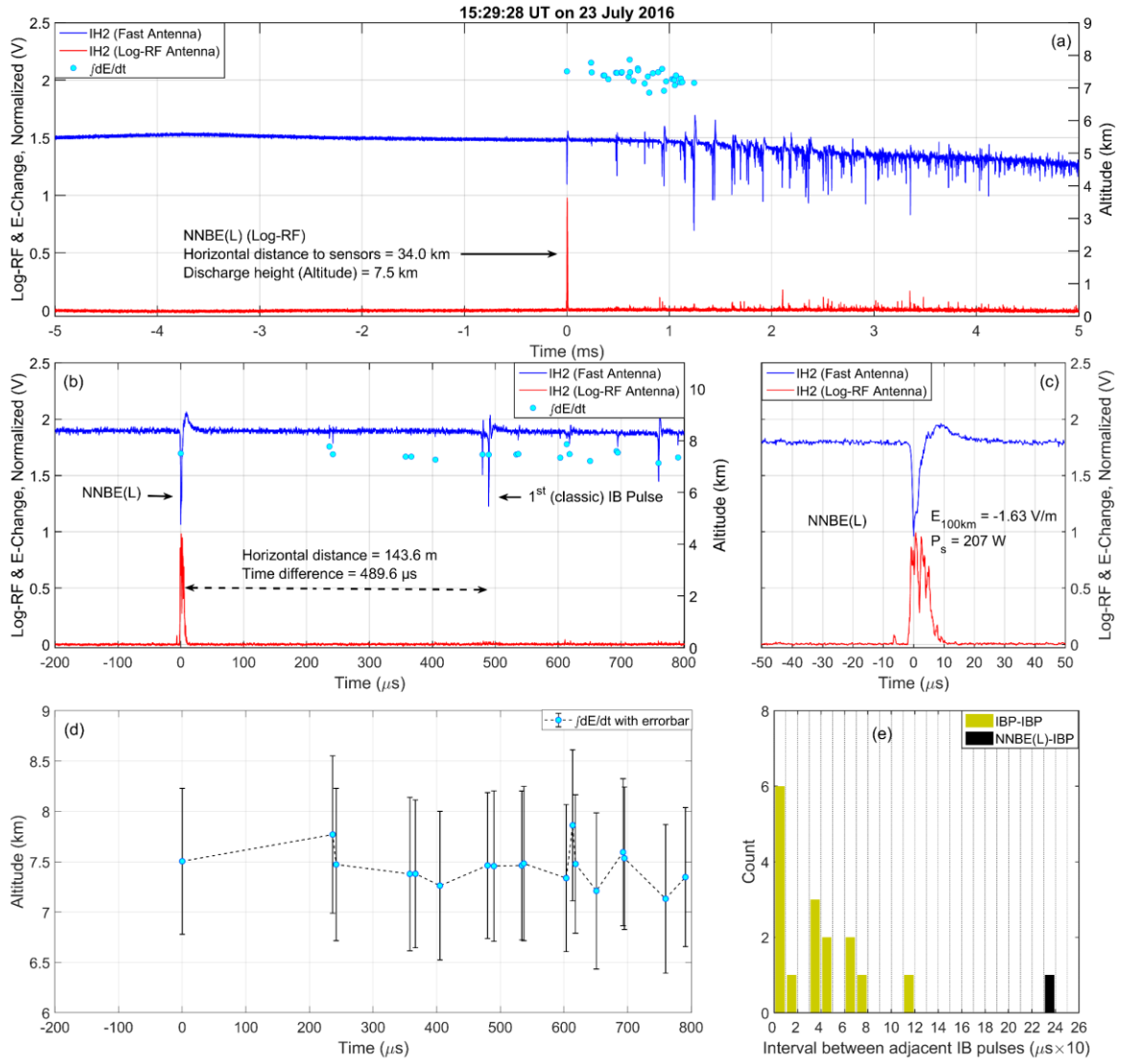


Figure B.6. Example of NNBE(L) occurred as the initial event of a negative CG flash.

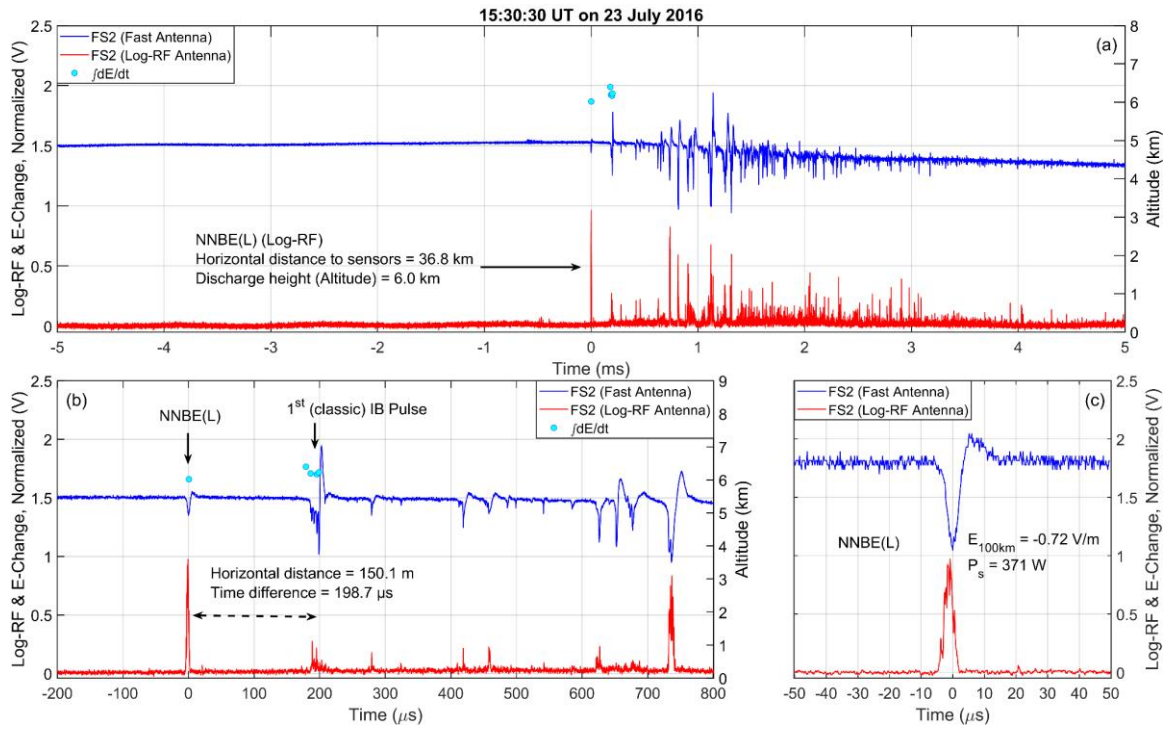


Figure B.7. Example of NNBE(L) occurred as the initial event of a negative CG flash.

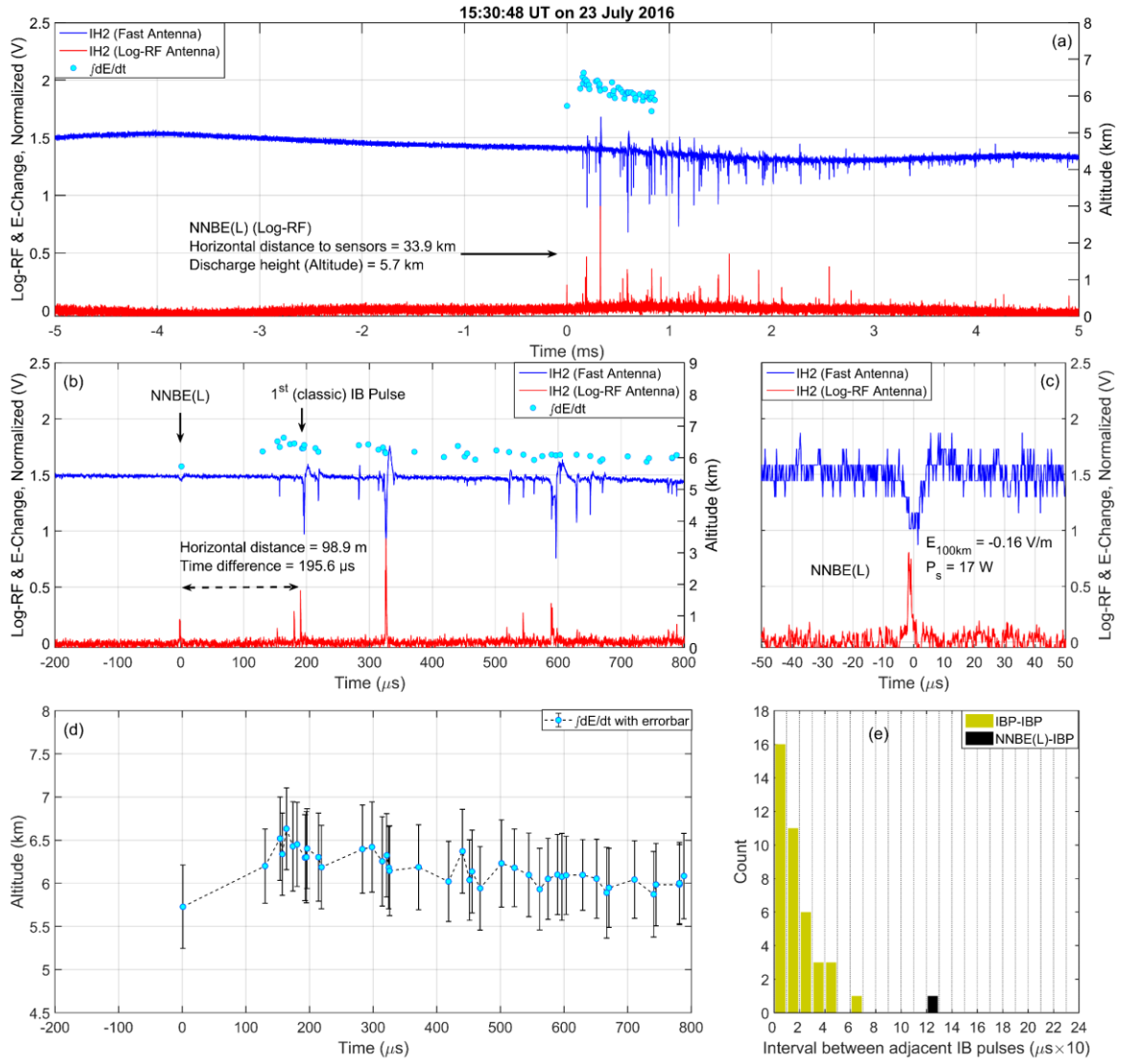


Figure B.8. Example of NNBE(L) occurred as the initial event of a negative CG flash.

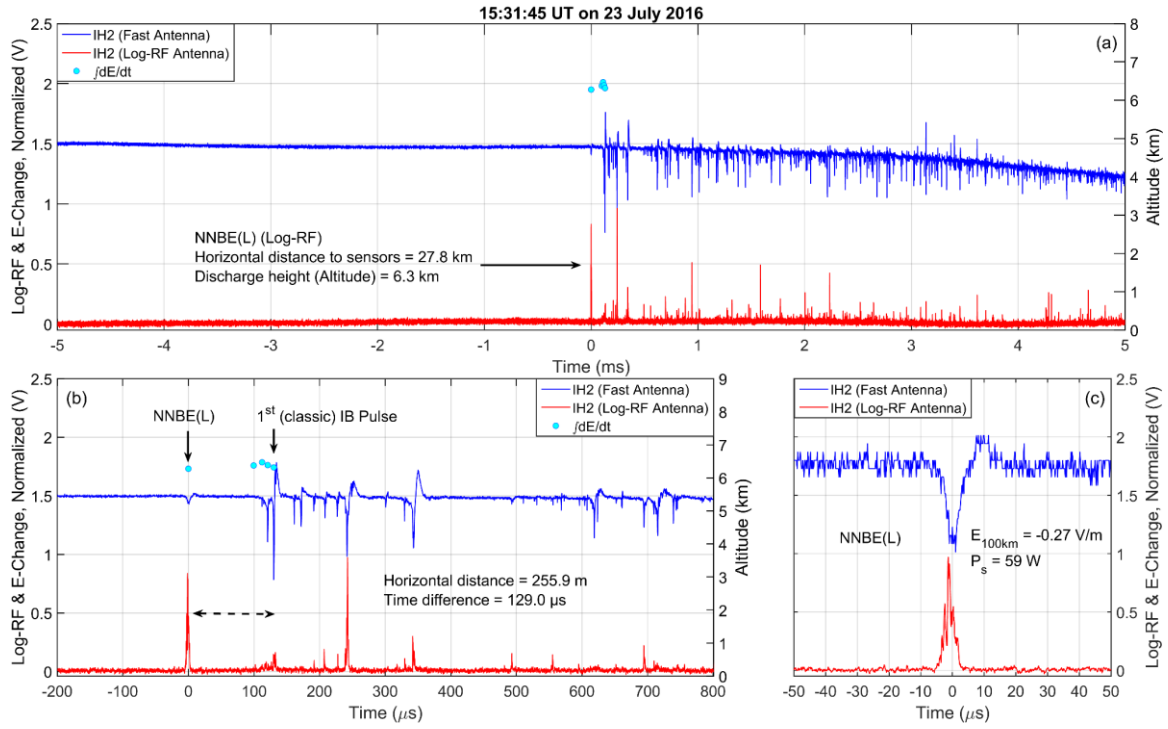


Figure B.9. Example of NNBE(L) occurred as the initial event of a negative CG flash.

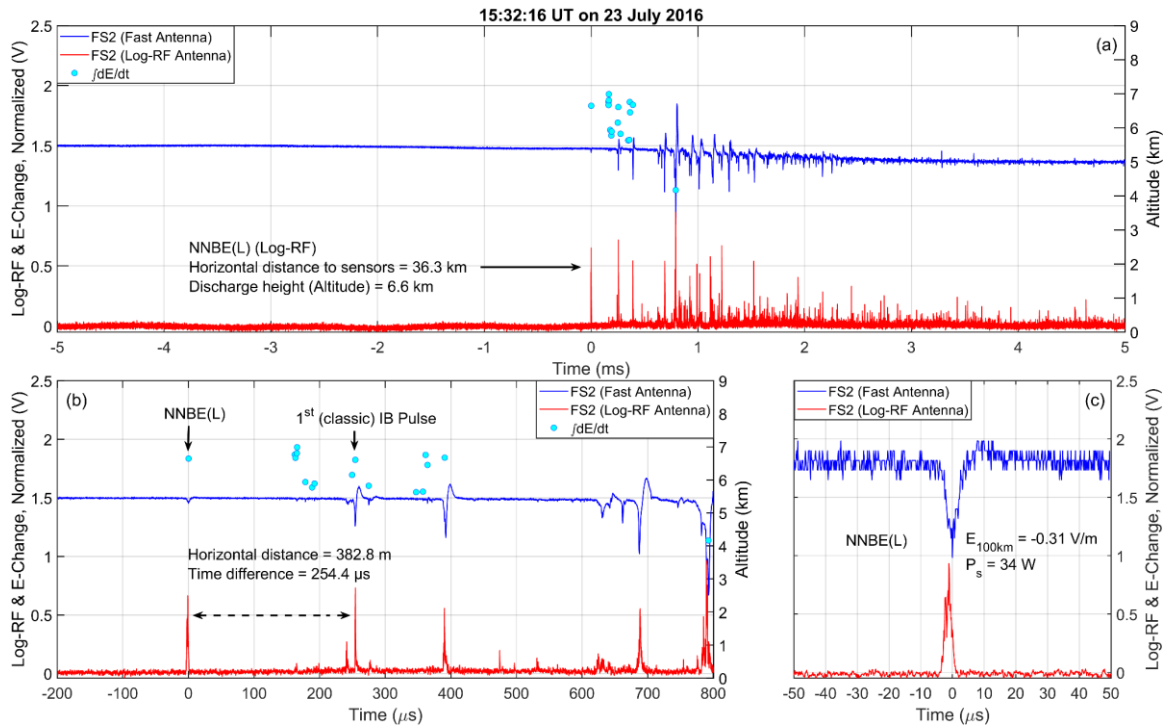


Figure B.10. Example of NNBE(L) occurred as the initial event of a negative CG flash.

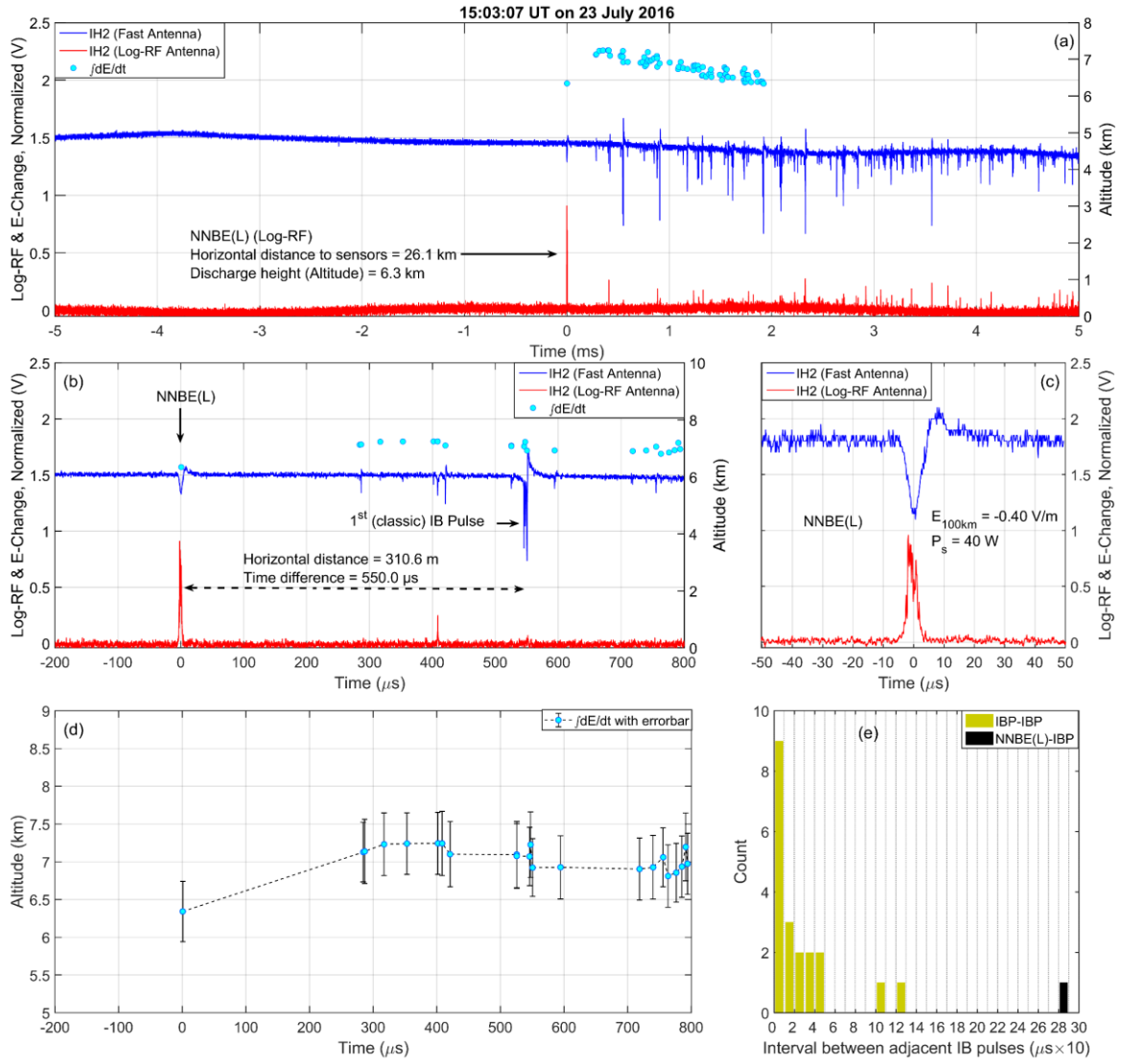


Figure B.11. Example of NNBE(L) occurred as the initial event of a negative CG flash.

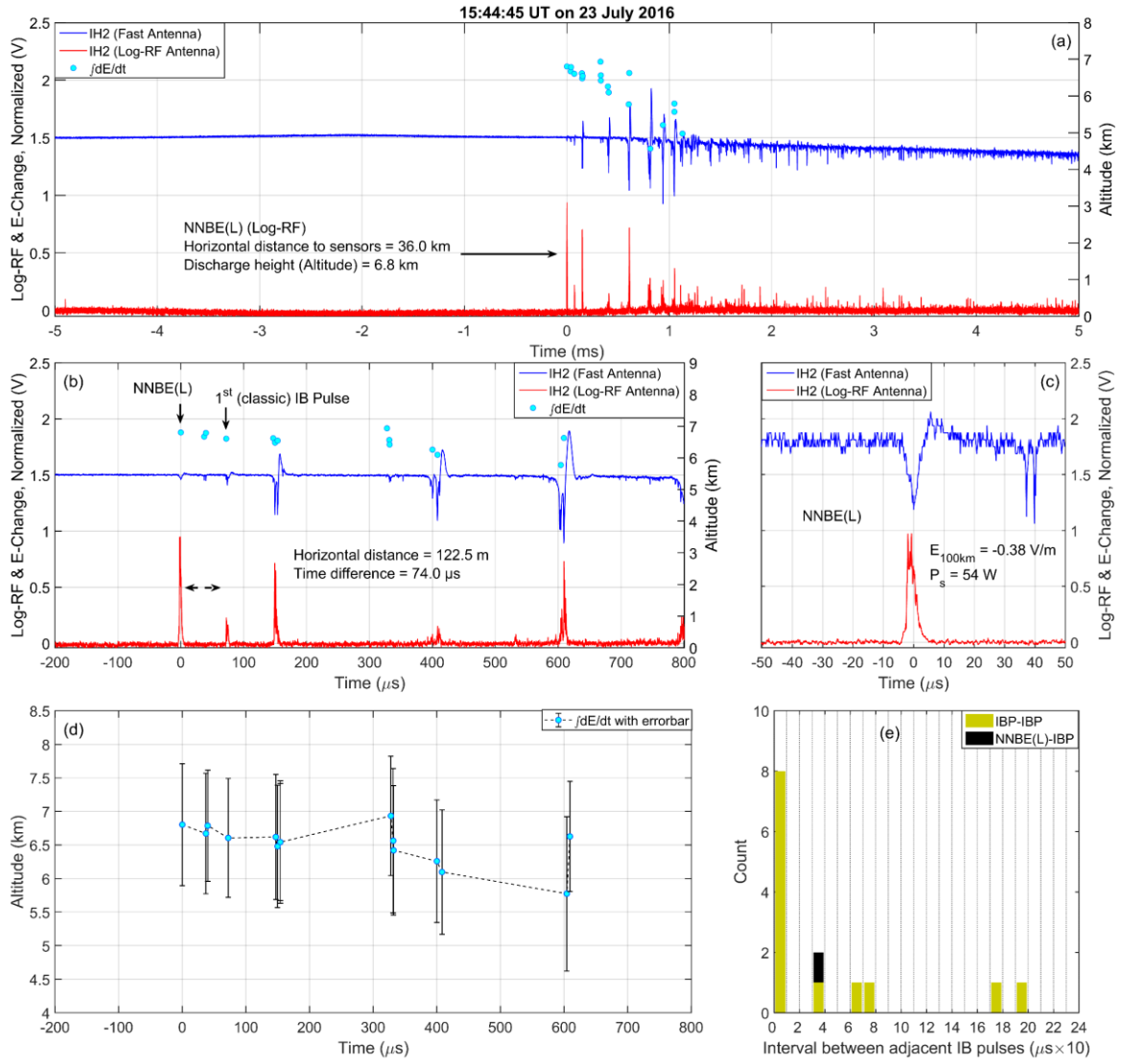


Figure B.12. Example of NNBE(L) occurred as the initial event of a negative CG flash.

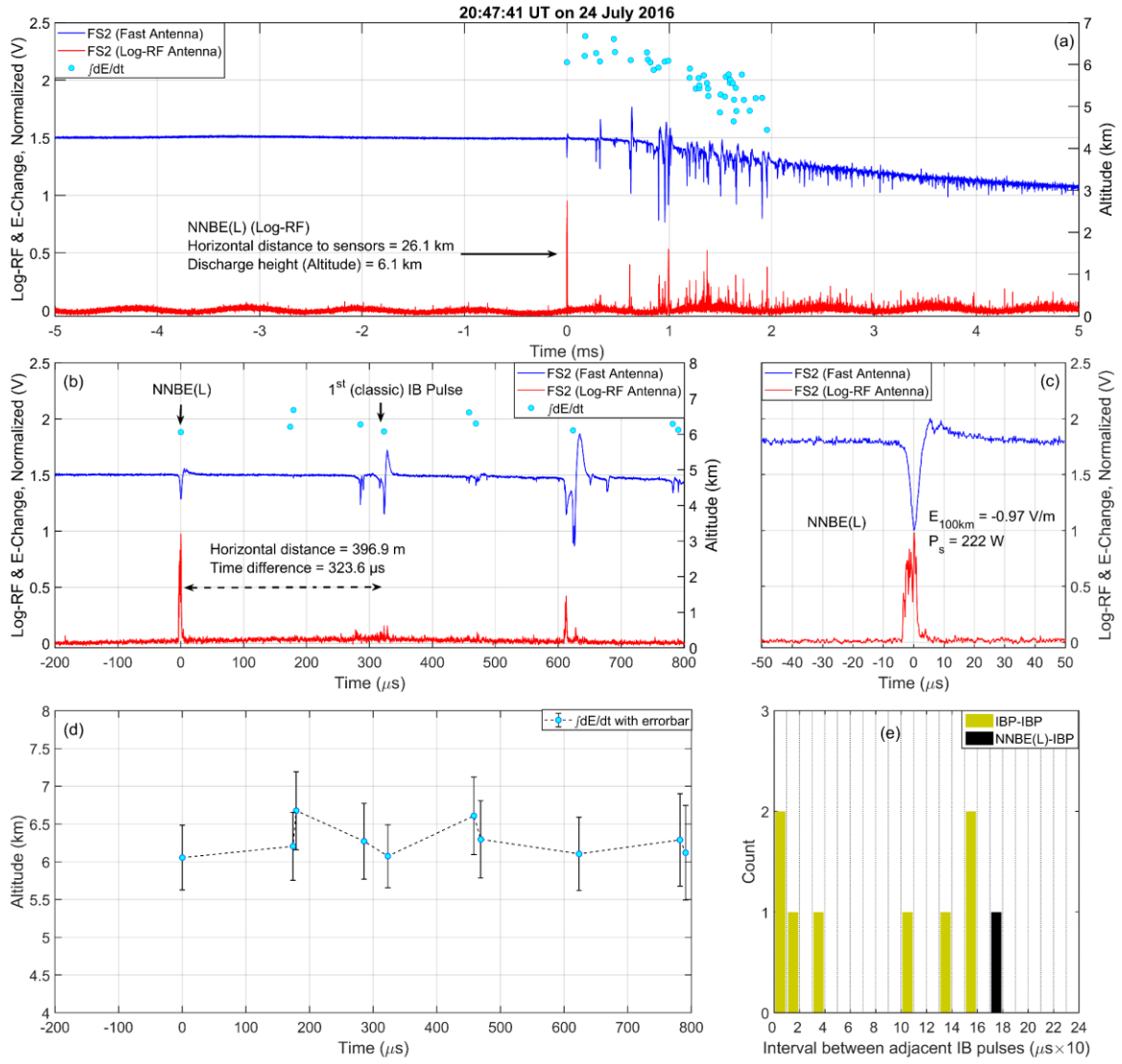


Figure B.13. Example of NNBE(L) occurred as the initial event of a negative CG flash.

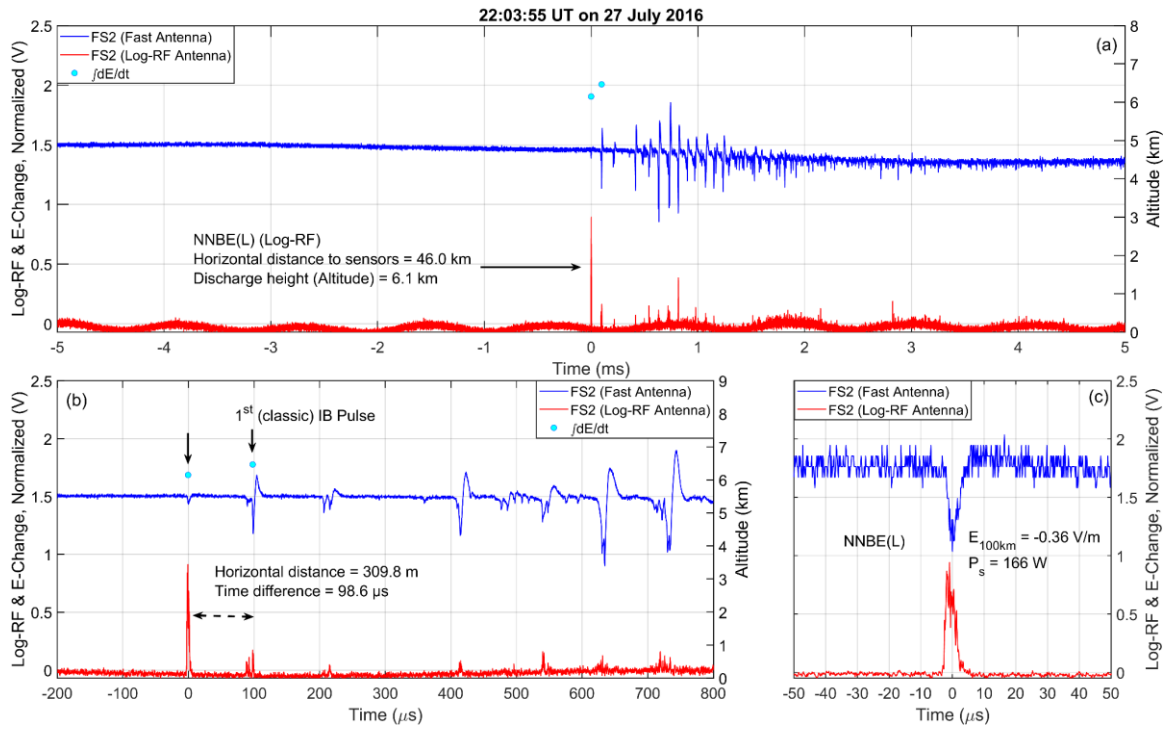


Figure B.14. Example of NNBE(L) occurred as the initial event of a negative CG flash.

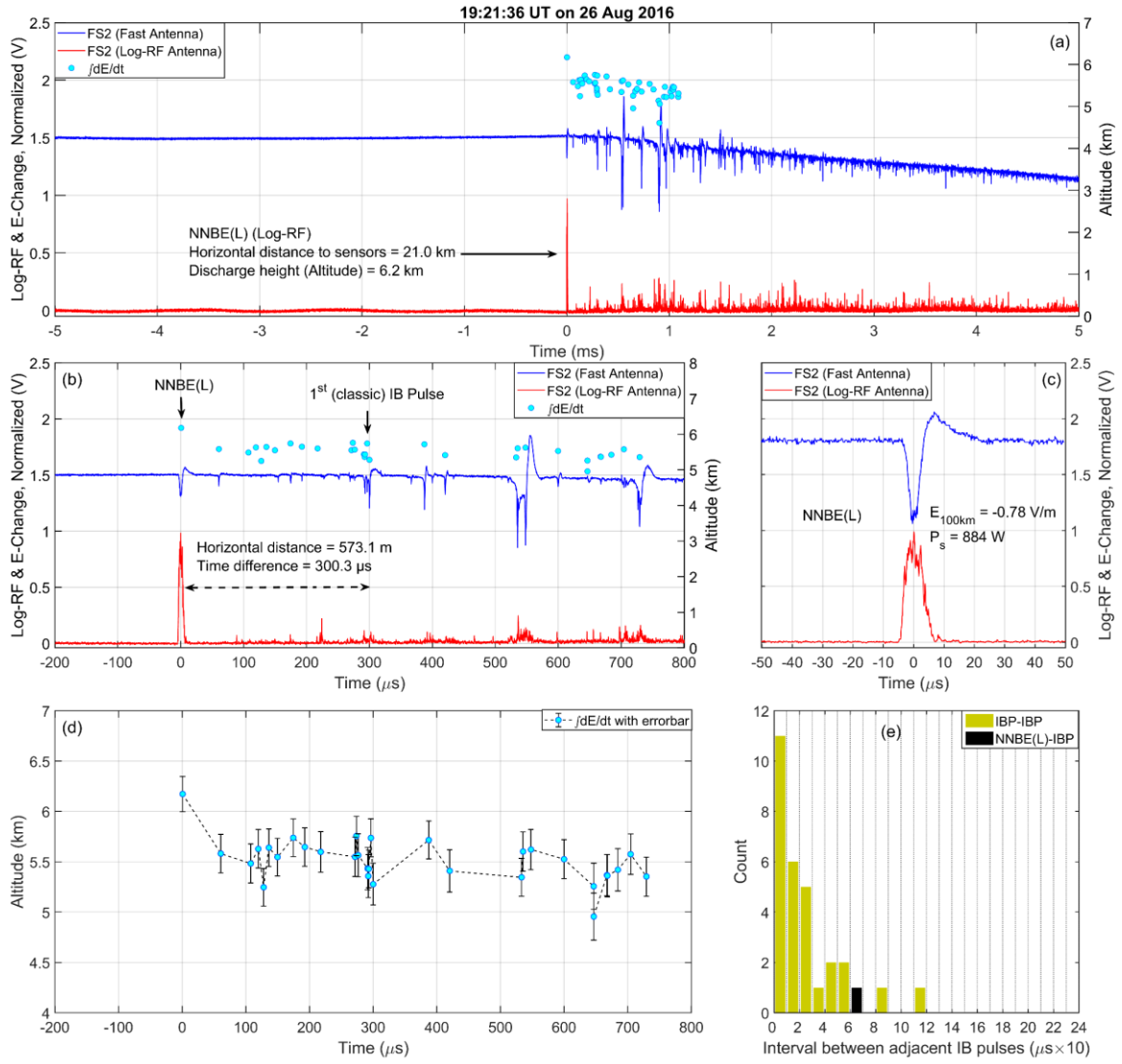


Figure B.15. Example of NNBE(L) occurred as the initial event of a negative CG flash.

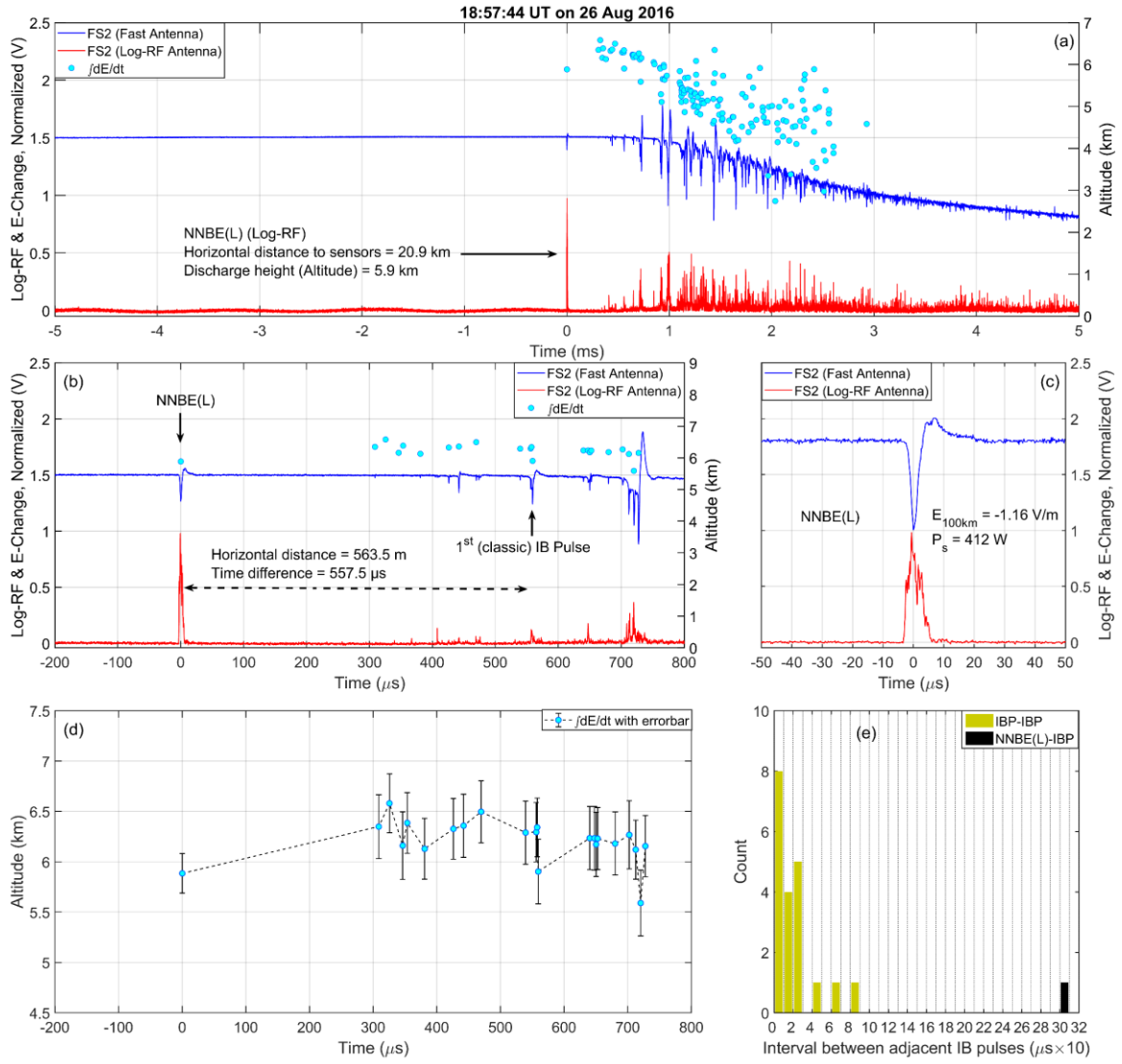


Figure B.16. Example of NNBE(L) occurred as the initial event of a negative CG flash.

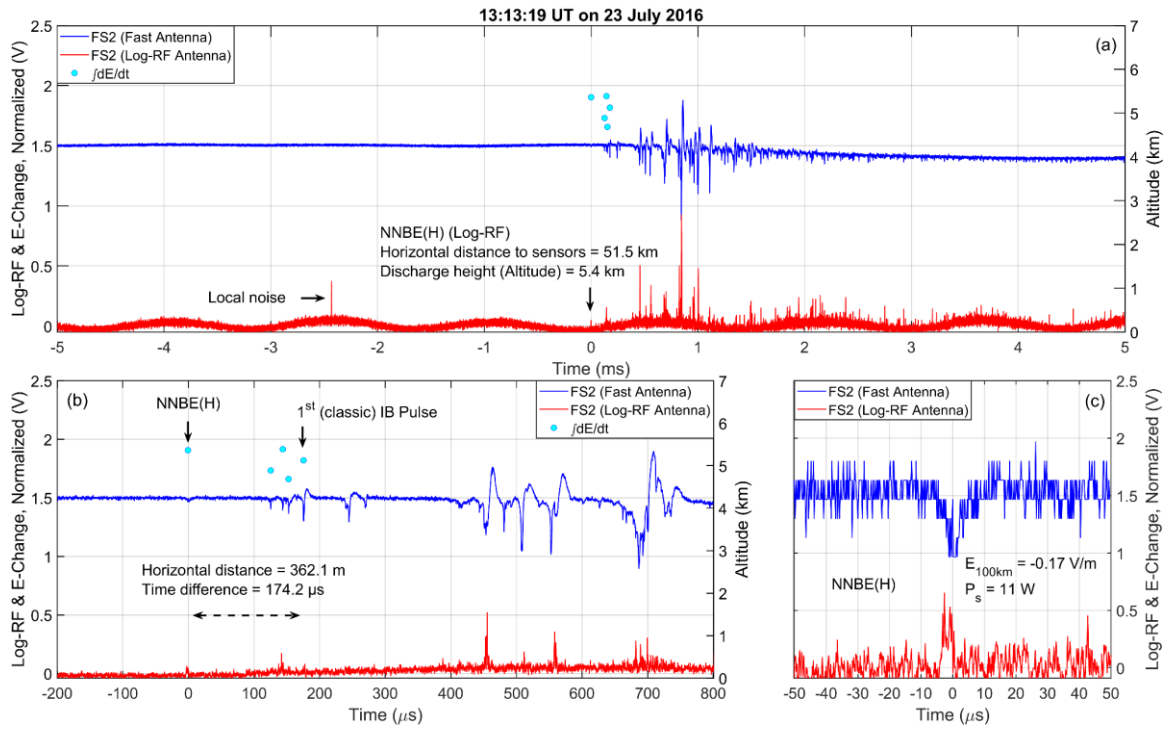


Figure B.17. Example of NNBE(H) occurred as the very first event of a negative CG flash.

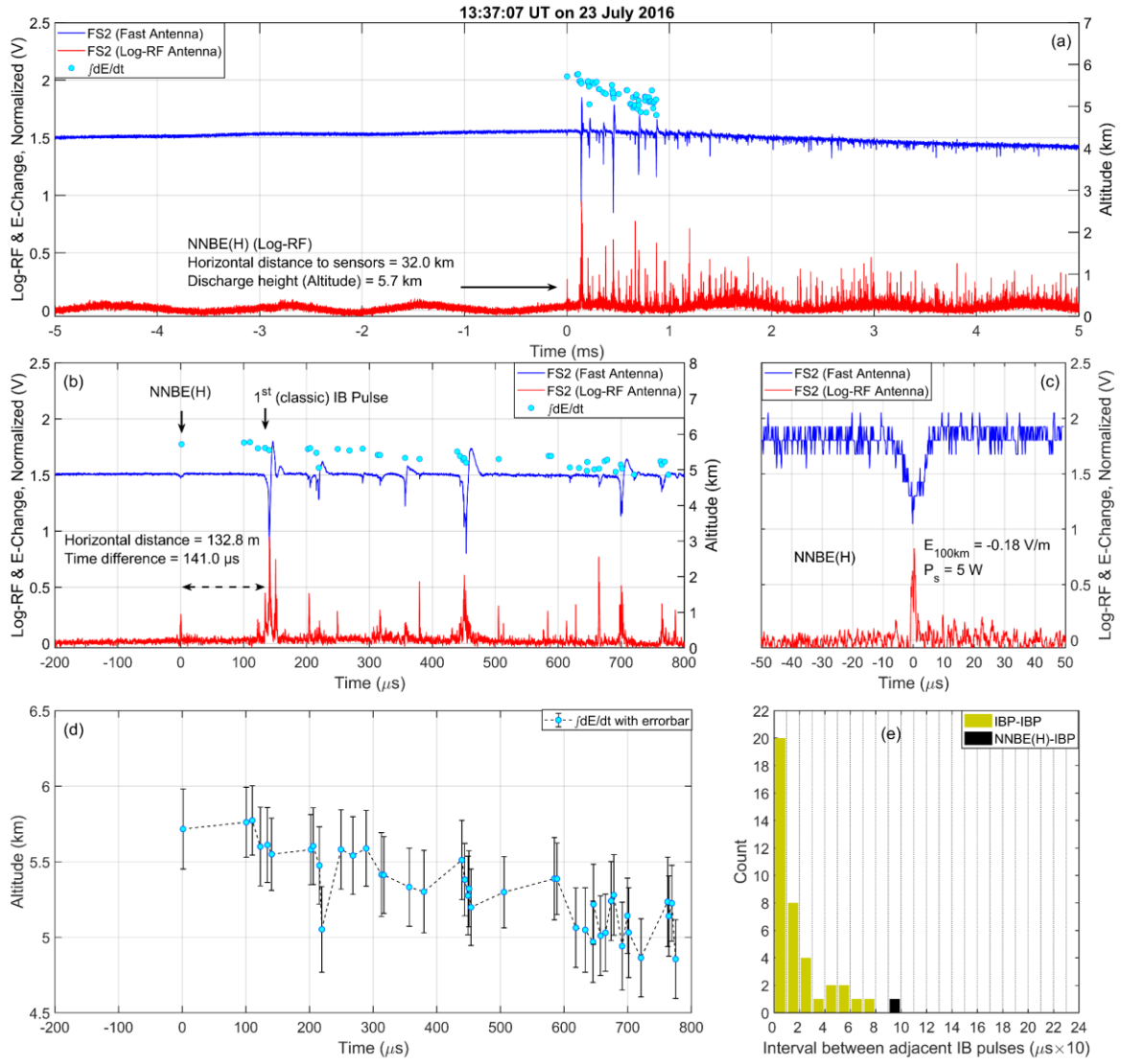


Figure B.18. Example of NNBE(H) occurred as the very first event of a negative CG flash.

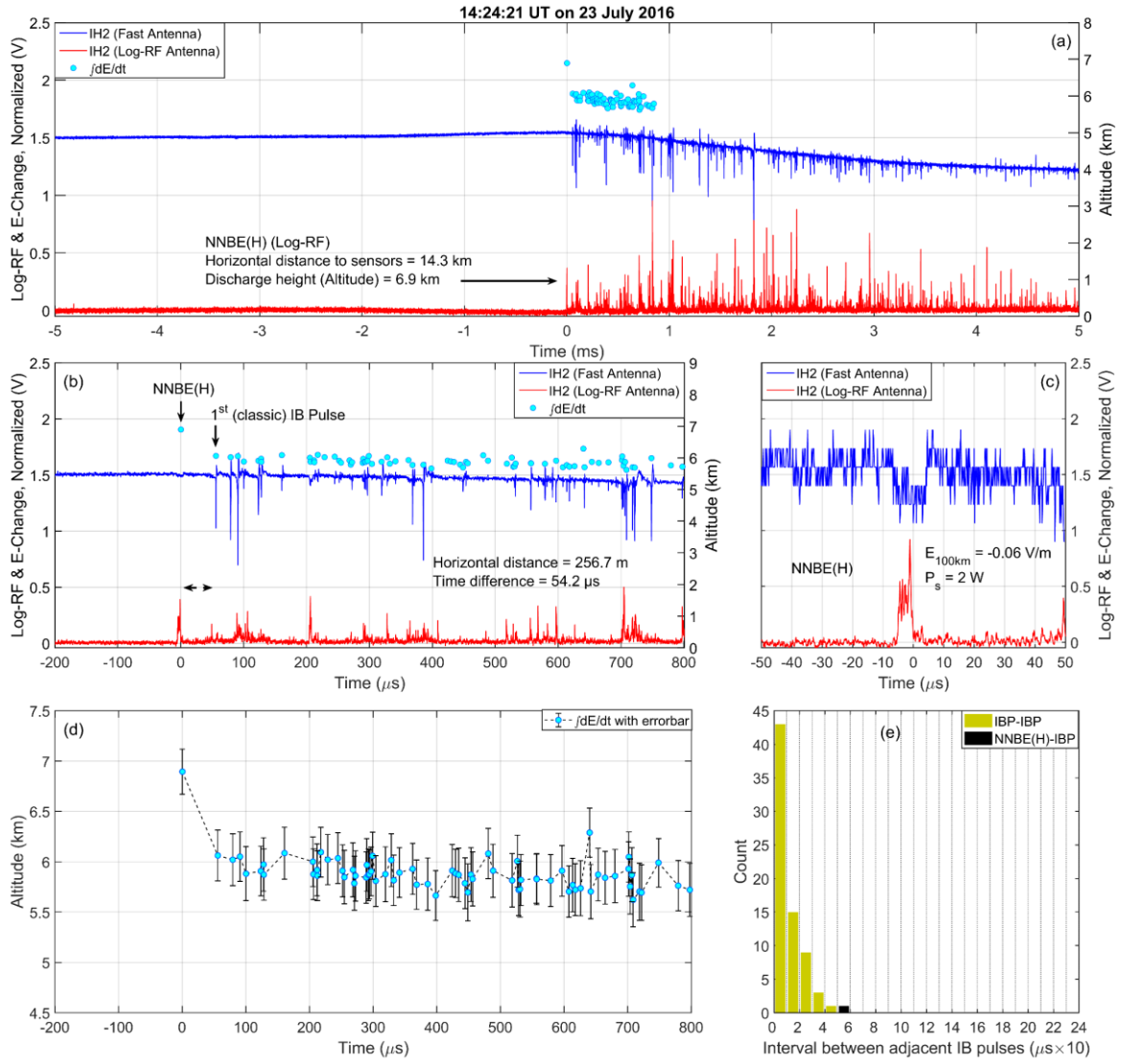


Figure B.19. Example of NNBE(H) occurred as the very first event of a negative CG flash.

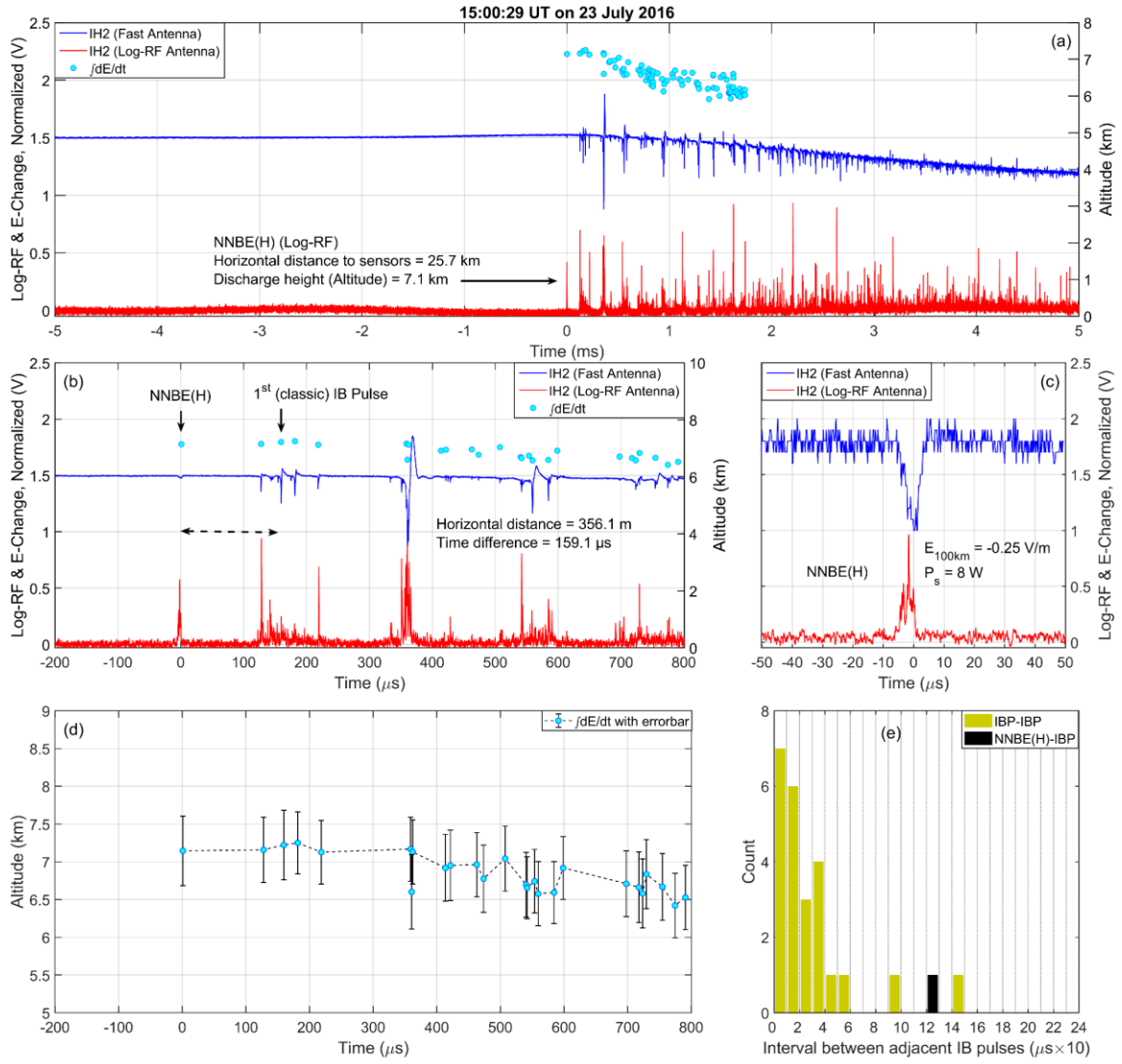


Figure B.20. Example of NNBE(H) occurred as the very first event of a negative CG flash.

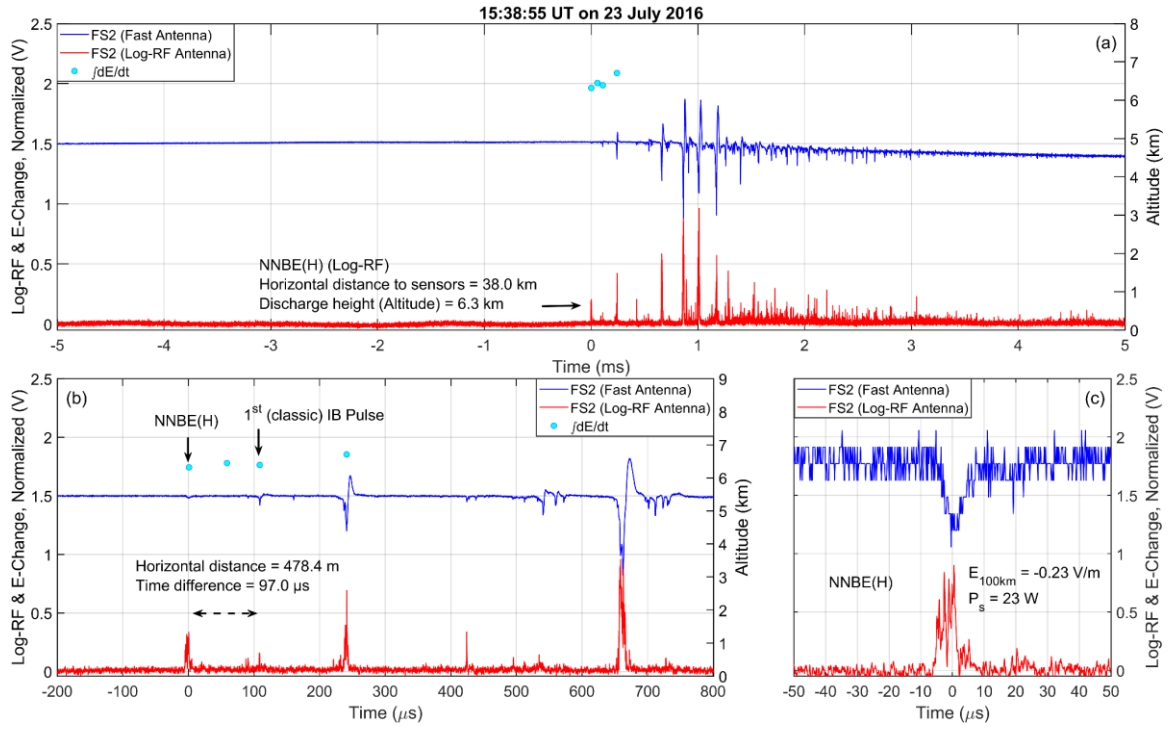


Figure B.21. Example of NNBE(H) occurred as the very first event of a negative CG flash.

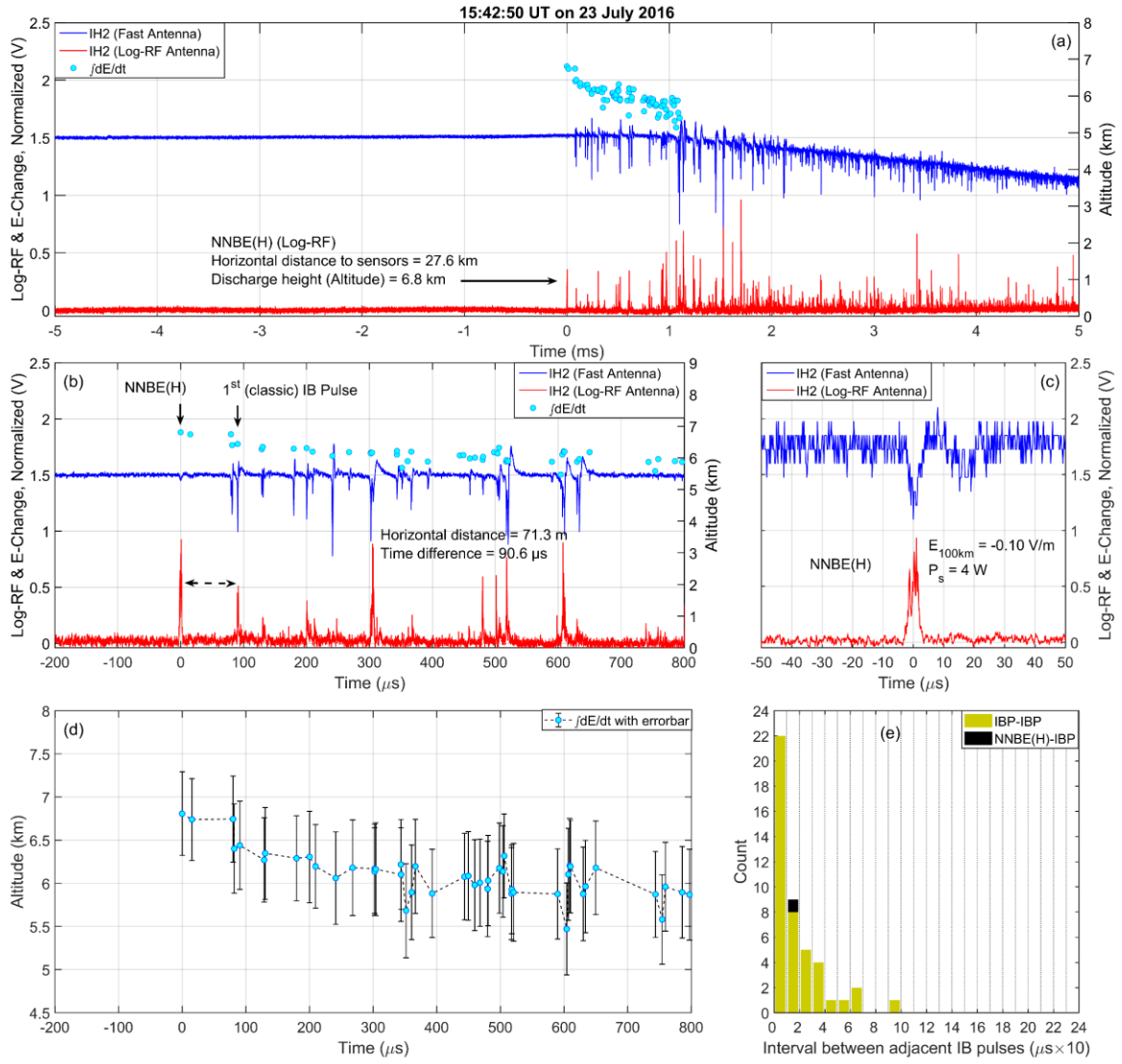


Figure B.22. Example of NNBE(H) occurred as the very first event of a negative CG flash.

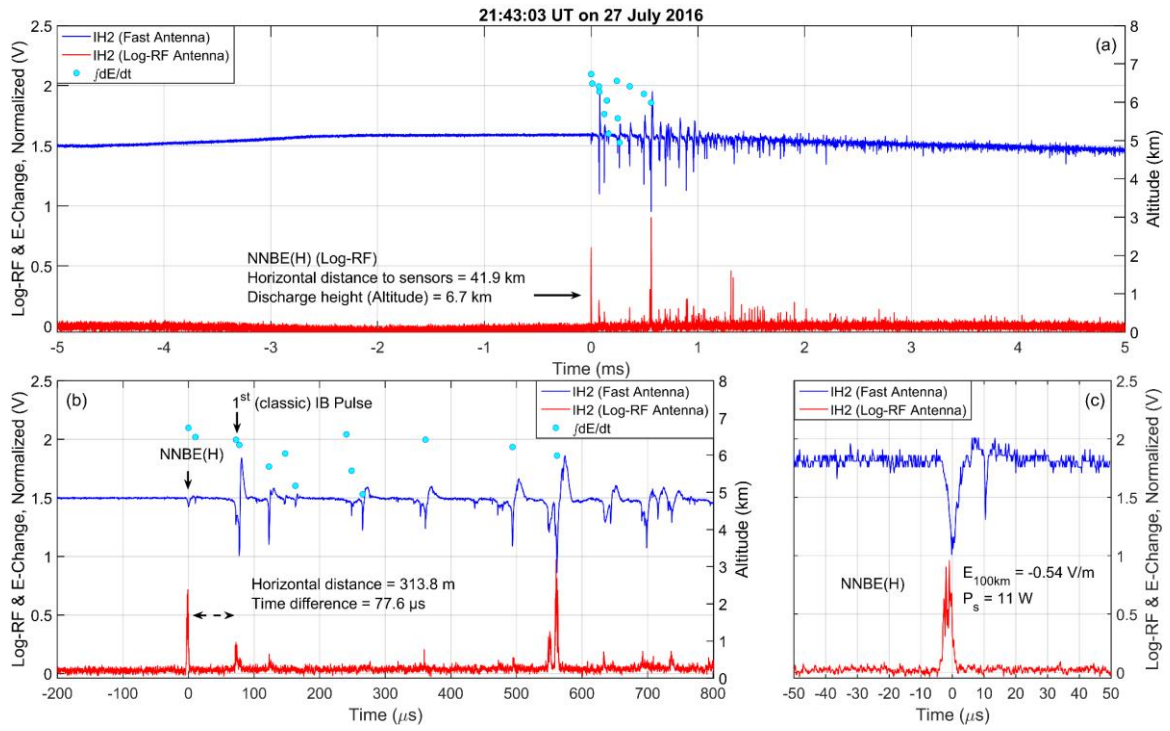


Figure B.23. Example of NNBE(H) occurred as the very first event of a negative CG flash.

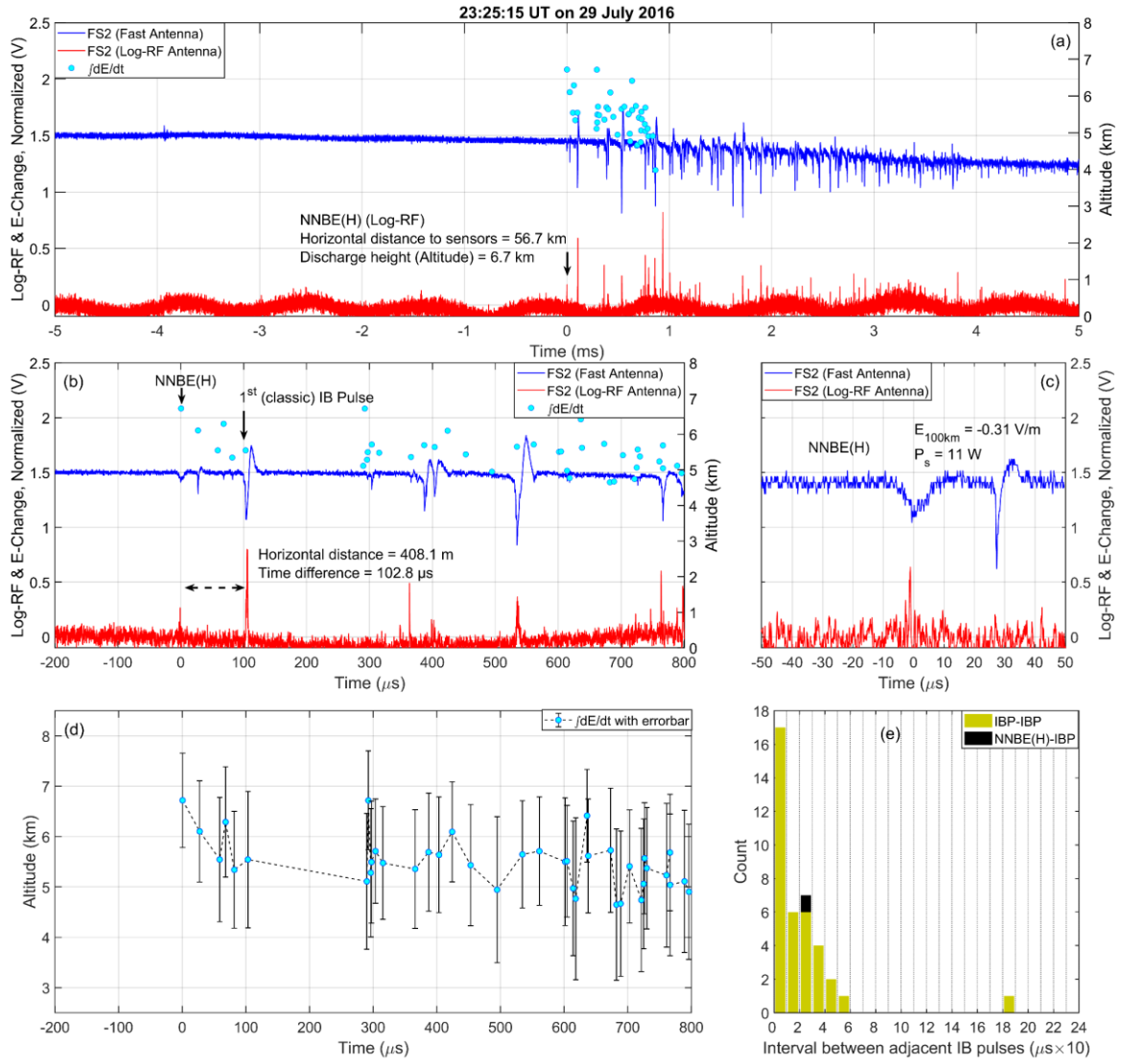


Figure B.24. Example of NNBE(H) occurred as the very first event of a negative CG flash.

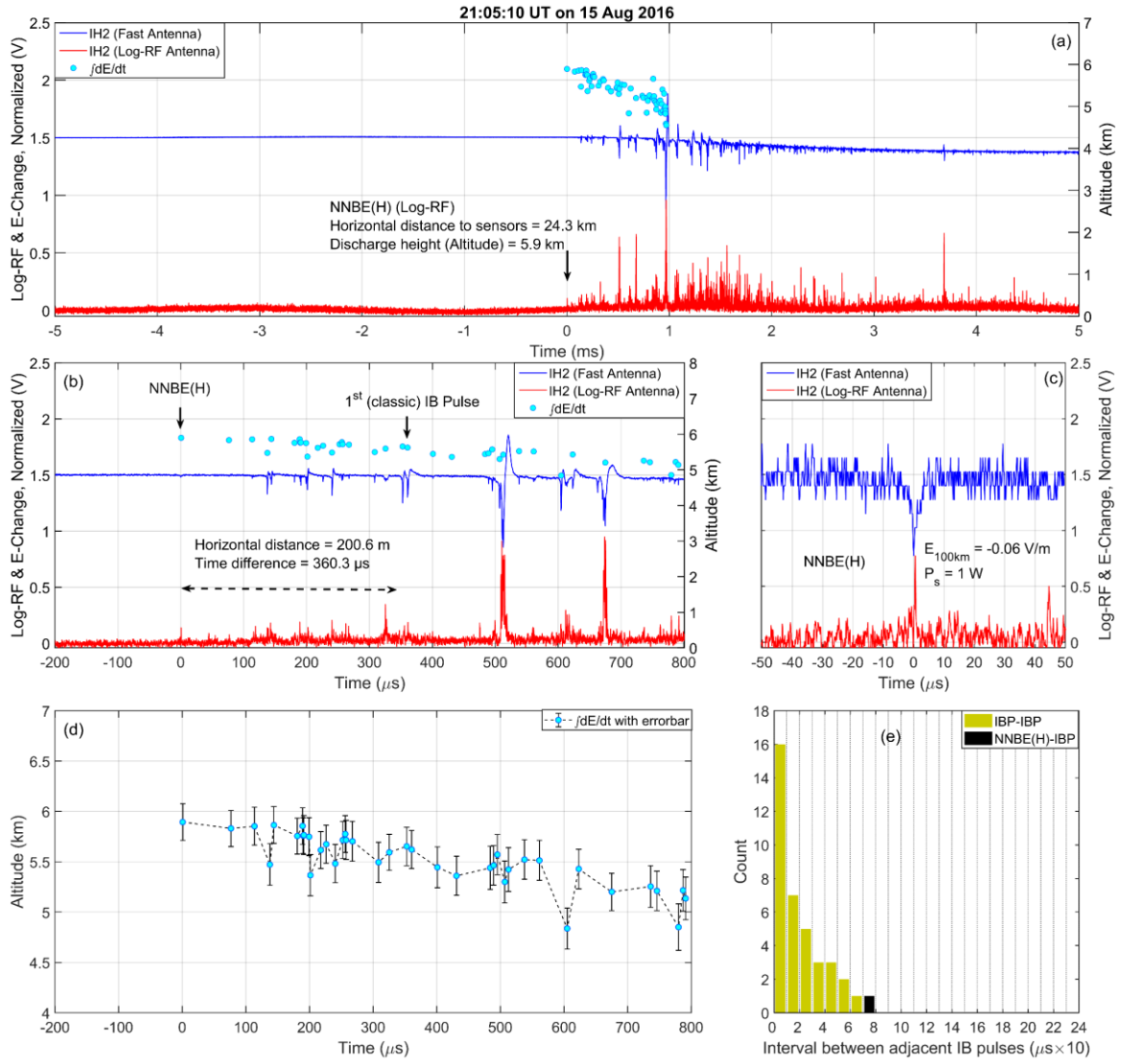


Figure B.25. Example of NNBE(H) occurred as the very first event of a negative CG flash.

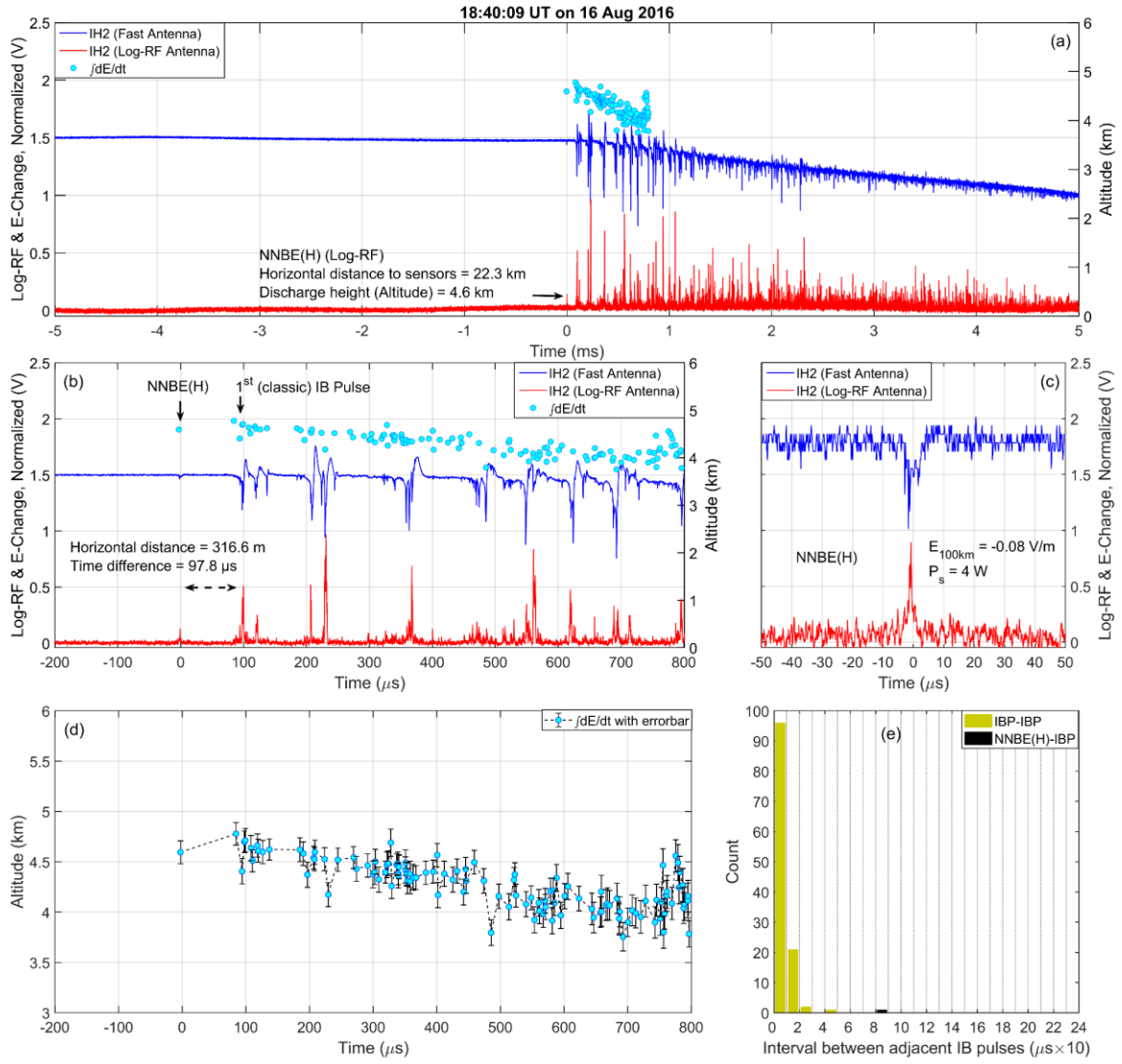


Figure B.26. Example of NNBE(H) occurred as the very first event of a negative CG flash.

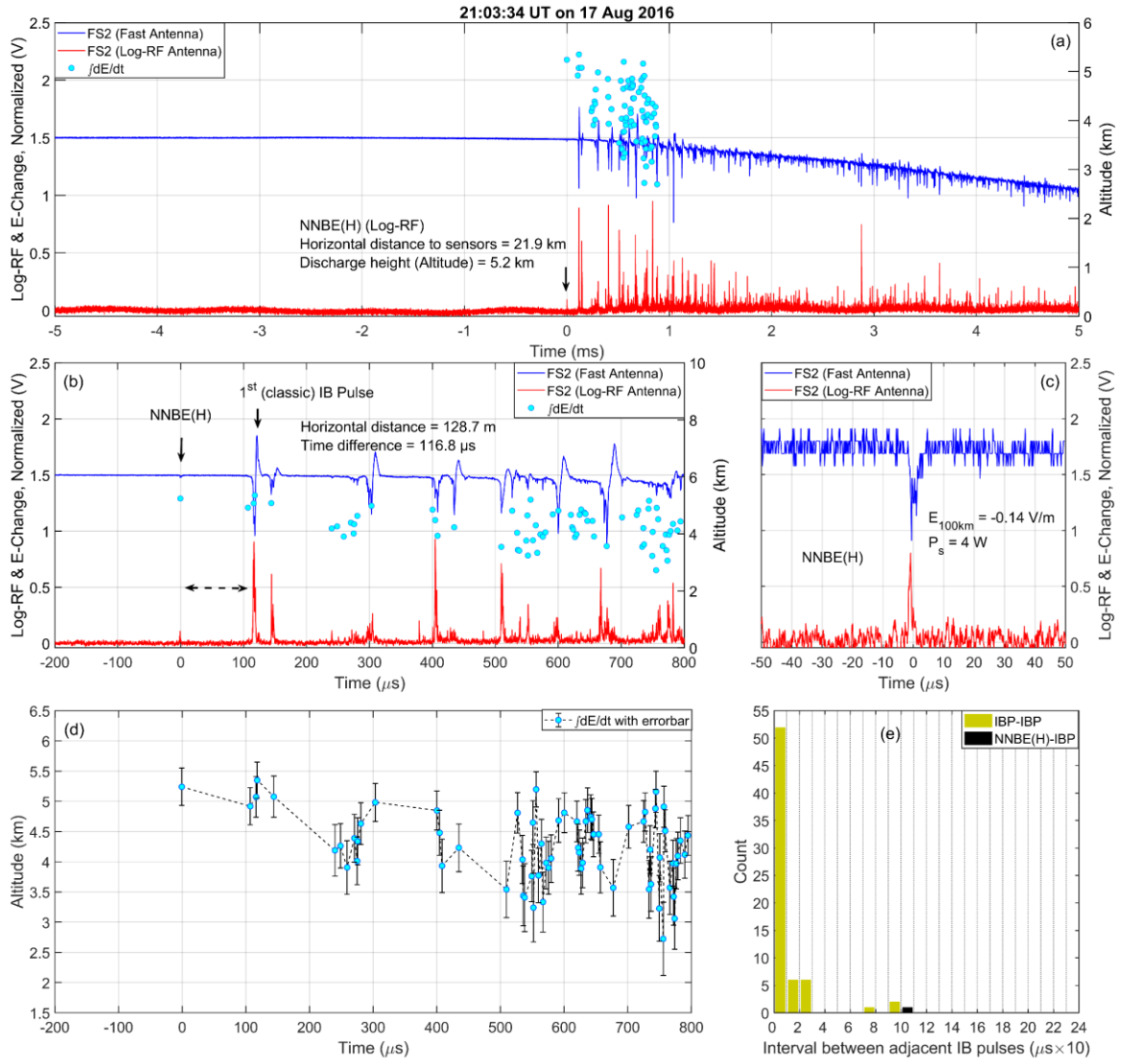


Figure B.27. Example of NNBE(H) occurred as the very first event of a negative CG flash.

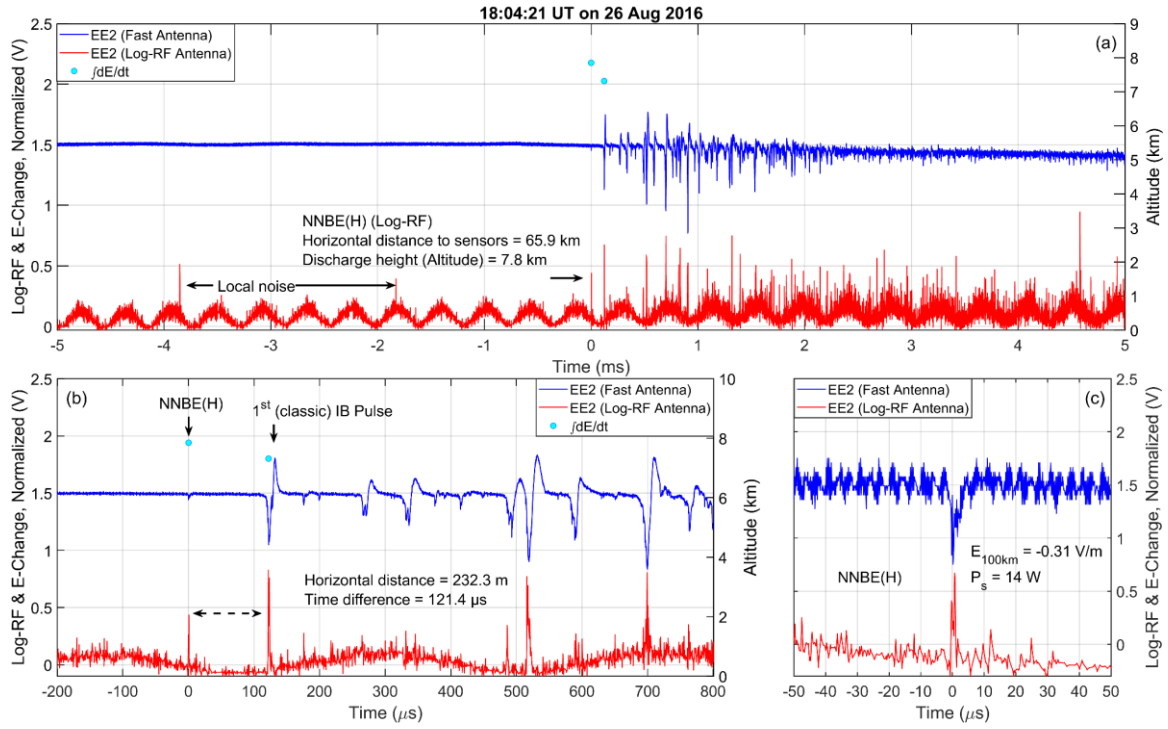


Figure B.28. Example of NNBE(H) occurred as the very first event of a negative CG flash.

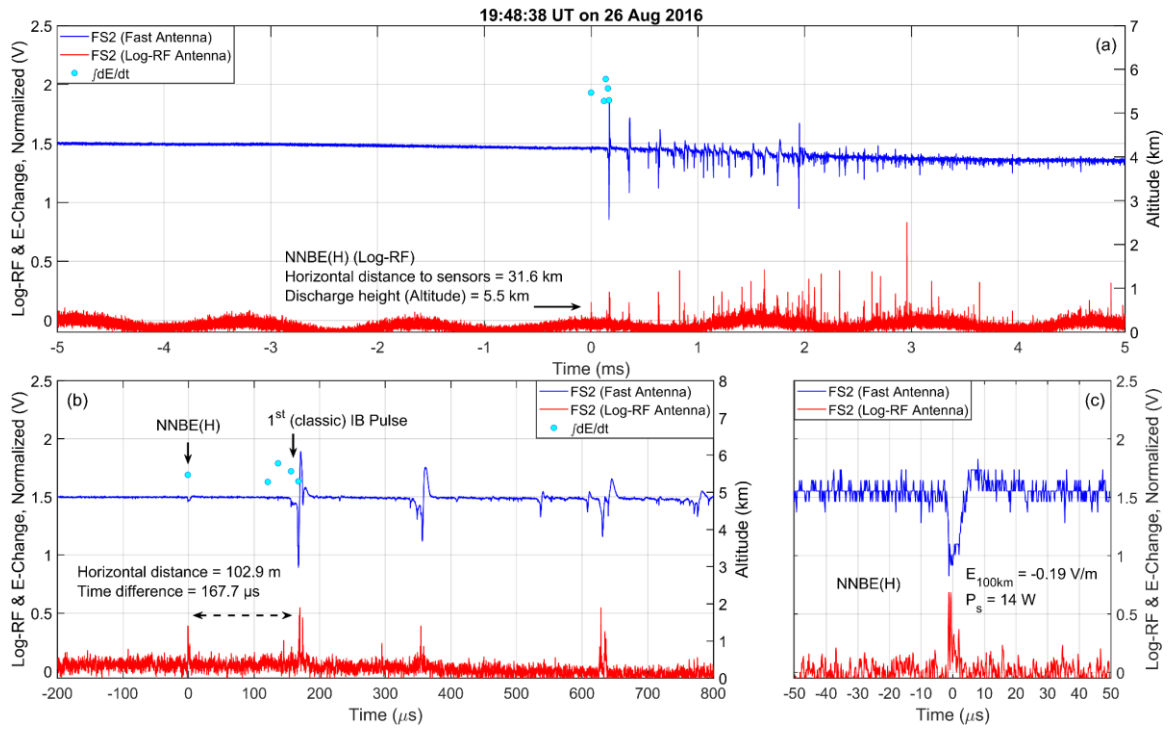


Figure B.29. Example of NNBE(H) occurred as the very first event of a negative CG flash.

VITA

Sampath Asiri Bandara was born in Medirigiriya, Sri Lanka. He received his Bachelor of Science (B.Sc.) degree in Physics with second upper class honors from University of Peradeniya, Sri Lanka in September 2011. After the graduation he has worked as a Teaching assistant in department of Physics in University of Peradeniya, Sri Lanka for two years. In 2014, he attended graduate school, of University of Mississippi. He obtained his Ph.D. in Physics and Astronomy from University of Mississippi in August 2019.